

Master of Science Thesis

Stochastic Collocation with CFD
robustness concepts for multi-dimensional
stochastic space
Application to a transonic airfoil

Huiqing Wang

Sept 13, 2015

**Stochastic Collocation with CFD
robustness concepts for
multi-dimensional stochastic space**
Application to a transonic airfoil

Master of Science Thesis

For obtaining the degree of Master of Science in Aerospace Engineering
at Delft University of Technology

Huiqing Wang

Sept 13, 2015



Delft University of Technology

Copyright © Aerospace Engineering, Delft University of Technology
All rights reserved.

DELFT UNIVERSITY OF TECHNOLOGY
DEPARTMENT OF AERODYNAMICS

The undersigned hereby certify that they have read and recommend to the Faculty of Aerospace Engineering for acceptance the thesis entitled **“Stochastic Collocation with CFD robustness concepts for multi-dimensional stochastic space”** by **Huiqing Wang** in fulfillment of the requirements for the degree of **Master of Science**.

Dated: Sept 13, 2015

Supervisors:

Dr. Richard Dwight

Prof. Stefan Hickel

Dr. Michiel Zaayer

Dr. Wouter Edeling

Acknowledgement

First and foremost, I would like to express my deepest gratitude to my supervisor Dr. Jeroen Witteveen, who brought me to the fantastic world of uncertainty quantification. I am grateful for his patience and expertise in guiding me through the whole project. In particular, I learned from him on scientific writing and how to do scientific research. Our collaborative work allows me to give my first academic presentation at the 1st International Conference on Uncertainty Quantification in Computational Sciences and Engineering, where I could meet many key researchers in UQ field.

Also, I would like to thank my supervisor at TU Delft Dr. Richard Dwight for correcting my thesis and your feedback on my research during the UMRIDA workshop. Many thanks for the other committee members Professor Stefan Hickel, Dr. Michiel Zaayer and Dr. Wouter Edeling for reading my thesis.

Thanks to my colleagues at Centrum Wiskunde & Informatica (CWI). Special thanks to Laurent for his help with the SU2 code. What's more, I am grateful for the funding support from the Scientific Computing group of CWI.

Last but not least, I would like to thank my parents for your endless support and love. Thanks too my girlfriend for every minute we spent together.

Huiqing Wang
Amsterdam, the Netherlands
September 2015

Abstract

Computational simulations have developed to a phase where the inherent physical variability prevalent in computational models exerts a larger effect on the predictive results than the deterministic numerical errors. To aim for more accurate and realistic simulations of the physical systems, it is imperative to include the input uncertainties into the computational models and investigate their effects on the outputs of interest. In the field of Computational Fluid Dynamics (CFD), which features high non-linearity and complexity, the non-intrusive Stochastic Collocation method (SC) gains great popularity by the virtue of easy implementation and high convergence rate of its spectral basis. The main idea of SC is to construct a surrogate response surface in the stochastic space by globally interpolating the sampling values obtained from the deterministic simulations. Therefore, like any other spectral method, it shows limitations in capturing local parametric steep gradient or discontinuity in the stochastic space. Besides, the convergence rate is deteriorated due to the Gibbs oscillations. These spurious oscillations, which amount to unphysical realizations, could result in falsely enlarged full confidence interval, *e.g.*, the pressure distribution along the upper surface of a transonic airfoil. To provide more robust stochastic analysis, the Gibbs oscillations in the stochastic space need to be eliminated.

To this end, the robustness concepts from the CFD community, *i.e.*, Local Extremum Conserving (LEC), Monotonicity Preserving (MP) and Essentially Non-Oscillatory (ENO), are reformulated for the multi-dimensional stochastic space and incorporated into the Stochastic Collocation method. The proposed method is termed Stochastic Collocation with Essentially Non-Oscillatory (SC-ENO) robustness. Different from the traditional Stochastic Collocation method, the SC-ENO method first resolves the locations of the discontinuity in the stochastic space by enforcing the robust limiter to the surrogate response surface. Then the whole stochastic space is partitioned into disjoint smooth sub-domains bounded by the discontinuities. All the deterministic sampling points are classified into each smooth sub-domain. Finally, the model surrogate in each smooth element is constructed by interpolating the sampling points of the same class. The proposed discontinuity detection method is implemented for the 1-dimensional space and extended to the multi-dimensional space by the so-called dimension-by-dimension approach. Hence, the deterministic multi-dimensional

sampling points are structured and formed by the tensor product of 1-dimensional nodes. As for the surrogate construction, the performance multivariate interpolation methods, *i.e.*, Sauer-Xu Lagrange interpolation and the least interpolation, are compared in terms of the robustness and the accuracy. The least interpolation method is better than Sauer-Xu algorithm but it lacks robustness for certain distribution of the sampling points. To remedy this, an element-wise interpolation method matching the proposed discontinuity detection method is developed.

One remarkable feature of the proposed SC-ENO method is being completely *non-parametric*. It is essentially a *post-processing* of the input sample realizations. When the deterministic sampling points are structured, it has been proved that SC-ENO is able to choose automatically either a piecewise or a global polynomial approximation based on the smoothness of the target solutions in each dimension of the stochastic space. Therefore, the robustness of the surrogate model is ensured while the efficiency of Stochastic Collocation method is maintained. The accuracy and convergence property of the proposed SC-ENO method is investigated for some numerical test functions with jump discontinuities. Although there is no obvious improvement of the convergence rate, especially for the statistical quantities, the issue of the Gibbs oscillations is solved. To see how SC-ENO performs for real problems with jump discontinuities or steep gradient in the stochastic space, it is applied to the shock tube problem with uncertainties in initial conditions and the transonic viscous flow over the RAE 2822 airfoil with uncertainties in inflow conditions. In both of these test cases, the accuracy, efficiency and robustness of the SC-ENO method are illustrated. It is shown that there are no unphysical overshoots in the full confidence intervals of the interested quantities with sufficient deterministic sampling points. Meanwhile, the performance of another approach dealing with the stochastic discontinuities, *Subcell Resolution* (SR), is investigated for these two test cases. It is concluded that the SC-ENO method is more suitable for the viscous flow problems whereas the SR approach performs better for the inviscid case. Using the same set of the deterministic sampling values, the results of some interested quantities of smooth nature are presented, where the spectral convergence property is obtained.

Since the SC-ENO method works on the tensor product sampling points, it is prone to the *curse of dimensionality* for high-dimensional stochastic spaces. To reduce the computational resources, the proposed approach is combined with the sparse grid approach of both isotropic type and dimension-adaptive type. However, the numerical experiments show that the robustness property of the SC-ENO is lost for the sparse grid case. A more efficient and robust scheme suitable for high-dimensional space is a future research topic.

Contents

Acknowledgements	v
Abstract	vii
1 Introduction	1
1.1 Uncertainty Quantification in Computational Fluid Dynamics	1
1.2 Thesis objectives	3
2 Review of existing numerical methods	5
2.1 Mathematical formulation	5
2.2 Monte Carlo sampling-based techniques	6
2.3 Generalized Polynomial Chaos methods	7
2.3.1 Spectral expansion with gPC basis	8
2.3.2 Stochastic Galerkin methods (SGM)	10
2.3.3 Non-intrusive spectral projection methods	11
2.3.4 Interpolation approach based on gPC basis	12
2.3.5 Statistics of solutions	13
2.4 Stochastic Collocation method	14

2.4.1	Full tensor-product formulation for multi-dimensions	15
2.4.2	Conventional Sparse Grid formulation for multi-dimensions	15
2.5	Motivation for a new approach	18
3	Robust one-dimensional Stochastic Collocation with discontinuities detection	21
3.1	Robustness concepts from the CFD community	21
3.1.1	Local extremum conserving limiter	22
3.1.2	Monotonicity Preserving limiter	24
3.2	Stochastic Collocation with ENO robustness in 1-D	25
3.3	Subcell Resolution	29
3.4	Discussion of discontinuity detection methods	30
4	Multi-dimensional Stochastic Collocation with ENO robustness	33
4.1	Discontinuities detection in the multi-dimensional space	33
4.2	Domain classification	35
4.3	Multivariate interpolation on unstructured grids	36
4.3.1	Sauer-Xu multivariate Lagrange interpolation	37
4.3.2	Least interpolation	39
4.3.3	Comparison of the multivariate interpolation methods	41
4.3.4	Element-wise interpolation	44
4.4	SC-ENO with the dimension adaptive sparse grid	47
4.4.1	Error estimate	48
4.4.2	Adaptive procedure	49

4.4.3	Loss of the hierarchical structure	49
5	Numerical examples	51
5.1	Test functions	51
5.2	Comparison between traditional SC and SC-ENO	53
5.2.1	One-dimensional case	53
5.2.2	Two-dimensional case on tensor grid	56
5.2.3	Post-processing time	59
5.3	Sparse grid	60
5.3.1	Standard sparse grid	60
5.3.2	Dimension adaptive sparse grid	64
6	Uncertainty quantification for shock tube problem	67
6.1	Shock tube test case descriptions	67
6.2	Deterministic simulation	68
6.3	Reference Monte Carlo results	69
6.4	Uncertainties propagation results with SC, SC-ENO and SR methods	69
6.4.1	Uncertain density at $x = 0.82$	69
6.4.2	Statistics and full confidence interval of the whole field	72
7	Uncertainty quantification for RAE 2822 airfoil	77
7.1	RAE 2822 airfoil test case descriptions	77
7.2	Deterministic simulation	79
7.3	Uncertainty propagation results with SC and SC-ENO	81

7.3.1	PDF of C_l , C_d and C_m	81
7.3.2	Pressure distribution around the airfoil surface	83
7.3.3	Mean and standard deviation of the whole pressure field	88
7.4	Uncertainties propagation with the Subcell Resolution (SR) method	88
7.4.1	Staircase approximation of the statistics	89
7.4.2	Subcell resolution for the transonic airfoil test case	90
7.4.3	Response surface in the parameter space with SR	90
7.4.4	Statistics and full confidence interval obtained with SR	91
7.4.5	Limitation of the SR method	93
8	Conclusions and Recommendations	95
8.1	Conclusions	95
8.2	Recommendations and future works	96
	Bibliography	104
A	The original Wiener polynomial chaos	105
B	Algorithm of the multivariate Lagrange interpolation	107
C	Construction of the least interpolant by Gauss elimination	109
D	Properties of the least interpolation method	113

Chapter 1

Introduction

This chapter starts with a general introduction of uncertainty quantification in Computational Fluid Dynamics (CFD) in Section 1.1. Then, the objectives of this thesis project is discussed in Section 1.2. Finally, the outline of this thesis is presented.

1.1 Uncertainty Quantification in Computational Fluid Dynamics

Up to date, deterministic CFD simulations have made considerable achievements in engineering design and system analysis. Accurate, efficient and robust numerical schemes have been developed to solve the governing model of the flow field under study. However, there still exist differences between the real flow field and the simulation results. Part of these differences result from the inevitable discretization errors originating from the numerical solutions of the mathematical model (round-off, numerical diffusion/dispersion, iteration errors, etc.) in the spatial or temporal domain, while the other parts can be attributed to the ubiquitous uncertainties present in the real physical phenomena. These uncertainties fall into the following two categories [36]:

Aleatory uncertainty, also referred to as irreducible uncertainty, is the *physical variability present in the system being analyzed*. Under a probabilistic framework, it is normally modeled as random variable, whose probability density function (PDF) is usually prescribed by the observed variability or based on expert experience.

Epistemic uncertainty, also called reducible uncertainty, is *a potential deficiency due to a lack of knowledge in any phase of the modeling process*. It usually originates from assumptions or simplifications introduced in the derivation of the mathematical models (*e.g.* turbulence models). As a consequence, it can be reduced through refined physical models and experimental observations.

For numerical simulations associated with fluid dynamics, some common sources of uncer-

tainties are [51]:

- variability of operating conditions and initial conditions (*e.g.* angle of attack α for flow around the airfoil, the free stream Mach number of the steady flow),
- characterization of the physical domain (geometry, surface roughness, thickness-to-chord ratio of an airfoil),
- inherent heterogeneities of materials in the fluid-structure interaction,
- approximations and assumptions in mathematical model to represent the real physical process (*e.g.* linearizations of physical parameters, the incompressible or inviscid assumption, the two-dimensional approximation, neglect of radiative transfer in many natural convection models).

In order to provide more reliable simulation solutions, rigorous and trustworthy quantification of the numerical errors and uncertainties is required. The field of Uncertainty Quantification (UQ) aims to quantify the effects of the uncertain features of a computational model on certain output quantities of interest (QOI) by characterizing and propagating uncertainties based on mathematical methodologies. UQ is a powerful tool in decision making because it provides a rigorous mathematical measure of the confidence interval of interested quantities. Also, UQ becomes a necessary process for robust design since it provides an objective overview of the system performance in practical operating conditions when exposed to ubiquitous uncertainties.

There exist two general methodologies for Uncertainty Quantification: forward uncertainty propagation and inverse uncertainty quantification. Most forward uncertainty propagation approaches are based on the probabilistic framework [2]. Firstly, the uncertain features associated with the model under study are characterized as random variables based on the observed variability or expert experience using the statistical methods. Then, the presence of uncertainties can be incorporated into the model through the reformulation of the governing equations. After that, the effects of uncertain inputs are propagated through the computational model. Finally, the statistical moments of the quantities of interest are calculated, which provides valuable information to explain the deviation of the deterministic simulation results from the real physical phenomena. Further insights into the physical process can be gained by doing the sensitivity analysis and calculating the full confidence interval of interested quantities.

In the field of CFD, popular UQ methods for the uncertainty propagation are based on the deterministic sampling. These kinds of methods are called ‘*non-intrusive*’ methods since the existing high-fidelity CFD solvers can serve as the black box to produce a set of deterministic solutions. No modification of the existing codes is required. The surrogate model in the stochastic space is constructed by classical approximation methods, *e.g.*, the polynomial interpolation and the orthogonal projection.

1.2 Thesis objectives

Most of the non-intrusive methods rely on the interpolations of the deterministic solutions using the spectral polynomial basis in the stochastic space. They are efficient and applicable to complicated large scale CFD simulations with a moderately low number of uncertain inputs. However, the non-linearity in the fluid dynamics model can exhibit discontinuous solutions in the form of shock waves or contact surfaces in the spatial space as well as in the stochastic space. As a consequence, these efficient methods lack robustness in the case of approximating discontinuous solutions. The surrogate constructed with the spectral basis would exhibit Gibbs oscillations in the stochastic space. Besides, the convergence rate is deteriorated. What's worse, it is very likely that there are unphysical overshoots and undershoot in the statistics and the full confidence interval of the QOI, which makes the UQ analysis less objective and trustworthy.

This thesis focuses on improving the robustness of the existing efficient UQ methods. The main goal is to develop a non-intrusive uncertainty propagation method, which is able to provide reliable results under a limited computational resources. To that end, the robustness concepts from the CFD community are incorporated into the reference Stochastic Collocation (SC) method. The pursued efficient and robust approach is expected to be able to construct a non-oscillatory surrogate using a relatively low number of deterministic sampling points.

The rest of this thesis is organized as follows.

- The aim of Chapter 2 is to give a theoretical background for the subsequent chapters. The mathematical formulation of the stochastic inputs to the PDEs is presented. Several assumptions regarding the random variables and the function space are made. A general literature overview of popular spectral methods for forward uncertainty propagation under the probabilistic framework is given, with special focus on the construction of the polynomial basis and the sparse grid approach. Their properties in terms of the intrusiveness and the accuracy are discussed. Then, the Gibbs phenomenon is discussed in details, followed by a state-of-the-art literature review dealing with it. Finally, the motivations for this thesis work are presented.
- Chapter 3 presents the one-dimensional formulation of the proposed Stochastic Collocation method with ENO robustness (SC-ENO). Firstly, the robustness concepts from the CFD community and their reformulations are discussed. Then, a new discontinuity detection method is proposed and tested. After that, the subcell resolution (SR) approach is introduced briefly. Finally, a discussion of the existing discontinuity detection methods used in UQ is given.
- Chapter 4 shows the principle of the SC-ENO method in the multi-dimensional stochastic space. The proposed discontinuity detection method is extended to multi-dimensional space by the so-called 'dimension by dimension' approach. Two multivariate interpolation methods, *i.e.*, Sauer-Xu Lagrange interpolation and the least interpolation, are introduced. Their robustness and accuracy are investigated. Finally, details about how to combine the SC-ENO approach with the isotropic sparse grid and the dimension-adaptive sparse grid are given.

- Chapter 5 investigates the performance of the SC-ENO method when it is applied to various kinds of discontinuous test functions. Two types of deterministic sampling points, *i.e.*, the full tensor product grid and the sparse grid, are tested. The computational cost of SC-ENO is given.
- Chapter 6 provides the application of the SC-ENO method to the shock tube problem with uncertain initial conditions. Its accuracy and robustness are compared with those of the Stochastic Collocation method and the Subcell Resolution (SR) method.
- Chapter 7 deals with the test case of transonic flow over the RAE 2822 airfoil with uncertain operating conditions. Two kinds of probability distribution of the uncertain inputs are considered. Quantities of interest with different smoothness properties are calculated. Limitations of the SR approach is illustrated.
- Chapter 8 gives the conclusions of this thesis work. Some recommendations are discussed.

Chapter 2

Review of existing numerical methods

In this chapter, the advantages and disadvantages of different uncertainty propagation methods are discussed. First, the mathematical formulation of the random variables and the function space is presented in Section 2.1. Then, the Monte Carlo sampling method is discussed in Section 2.2. After that, the spectral methods based on the generalized Polynomial Chaos expansion are discussed in Section 2.3, including the intrusive and non-intrusive methods. After that, the traditional Stochastic Collocation method in combination with the conventional sparse grid are presented in Section 2.4. Finally, the motivations for this thesis project are presented.

2.1 Mathematical formulation

To propagate the parametric uncertainties through the computational model, we first need to characterize the uncertainties by a finite number of random variables. Let $(\Omega, \mathcal{A}, \mathcal{P})$ be a complete probability space, where Ω is the sample space, $\mathcal{A} \subset 2^\Omega$ the σ -algebra (non-empty collection of subsets of Ω), and \mathcal{P} the probability measure. The mapping $\Omega \rightarrow \mathbb{R}$ defines a random variable ξ , which assigns a real value $\xi(\omega)$ to each element ω of Ω . The set of possible values for $\xi(\omega)$, $\forall \omega \in \Omega$ is called the image of $\xi(\omega)$, which is denoted as $\Xi_\xi \subset \mathbb{R}$. The above definitions can be extended to vectors of random variables. Let $\boldsymbol{\xi} = \{\xi_j(\omega)\}_{j=1}^N : \Omega \mapsto \mathbb{R}^N$ denote a vector of random variables for $\omega \in \Omega$. In particular, let $\rho(\boldsymbol{\xi})$ be the joint Probability Density Function (PDF) of the random vector $\boldsymbol{\xi}$ corresponding to the probability measure \mathcal{P} . Then, the stochastic space is defined as:

$$\Xi = \prod_{j=1}^N \Xi_j \subset \mathbb{R}^N.$$

In this thesis, we assume that Ξ is bounded.

Suppose the computational model under consideration has a d -dimensional bounded physical domain $D \subset \mathbb{R}^d$ ($d = 1, 2, 3$) that is Lebesgue measurable interior. With the incorporation

of random variables, the d -dimensional governing equations of the physical model can be rewritten as an $(N + d)$ -dimensional differential equation:

$$\mathcal{L}(\boldsymbol{\xi}, \mathbf{x}, t; u(\boldsymbol{\xi}, \mathbf{x}, t)) = \mathcal{S}(\boldsymbol{\xi}, t, \mathbf{x}), \quad (\boldsymbol{\xi}, \mathbf{x}) \in \Xi \times D, \quad (2.1.1)$$

where $\mathcal{L}(\omega, \mathbf{x}, t)$ is some differential operator. $\mathbf{x} \in D$ and $t \in [0, T]$ are the spatial and temporal coordinates, and \mathcal{S} is a source term. The solutions of the governing equations $u(\boldsymbol{\xi}, \mathbf{x}, t)$ are called the output quantity of interest (QOI). For convenience, we omit the boundary operator, which can take various forms and have random components. Further, we assume that the boundary ∂D is sufficiently regular and the source term, boundary operator are properly posed, such that (2.1.1) is well-posed.

It should be noted that for each couple values of (\mathbf{x}, t) , the relation between $u(\boldsymbol{\xi}, \mathbf{x}, t)$ and the uncertain parameters $\boldsymbol{\xi}$ constitutes a real-valued function $u(\boldsymbol{\xi}) = f(\boldsymbol{\xi})$, which is affected by the physical model (2.1.1). Then the composition $U = f \circ \boldsymbol{\xi}$ defines a mapping from Ω to \mathbb{R} . Thus, the QOI is also a random variable.

Throughout this thesis, random variables with finite second order moments are considered, whose space is denoted as $L^2(\mathcal{P})$. This assumption is necessary to allow piecewise continuous solutions to the non-linear conservation laws subject to uncertainty. Let $X(\omega)$ and $Y(\omega)$ be two elements in $L^2(\mathcal{P})$. The expectation $\mathbb{E}[X, Y]$ defines an inner product as follows:

$$\mathbb{E}[X, Y] = \langle X(\omega), Y(\omega) \rangle = \int_{\Omega} X(\omega)Y(\omega)d\mathcal{P}(\omega). \quad (2.1.2)$$

Then, the associated norm comes as $\|X\|_{\Omega} = \sqrt{\langle X, X \rangle}$. With the above definitions of the inner product and norm, the space $L^2(\mathcal{P})$ is a Hilbert space. Therefore, we can utilize Fourier-like expansions and orthogonal projections, which are convergent with respect to the norm defined, to approximate the response surface $u(\boldsymbol{\xi}) = f(\boldsymbol{\xi})$ in the same way as in the deterministic context. The statistical moments of the QOI are given by:

$$\mu_{u_i}(\mathbf{x}, t) = \int_{\Xi} u(\boldsymbol{\xi}, \mathbf{x}, t)^i \rho(\boldsymbol{\xi})d\boldsymbol{\xi}. \quad (2.1.3)$$

2.2 Monte Carlo sampling-based techniques

Monte Carlo method is a classical method to propagate uncertainties through system based on random sampling following specific PDFs from the stochastic space. The statistics are readily computed by replacing the integrals (2.1.3) with the average sum over the whole set of samples. Although the convergence rate is relatively slow-approximately $1/\sqrt{n_{MC}}$, n_{MC} is the number of simulations-, it is universally applicable to the available computational tools and easy to parallelize. Also, it is independent of the stochastic dimension, making it suitable for larger number of uncertainties. However, for complex physical system which needs computationally expensive deterministic solver, this method is infeasible due to the fact that a large number of realizations is required to acquire good accuracy even for low-dimensional problems. To accelerate the convergence, Latin Hypercube sampling (LHS) [52] was applied to assess uncertainties in complex systems [34].

2.3 Generalized Polynomial Chaos methods

Nowdays, non-statistical methods based on the *generalized polynomial chaos* (gPC) expansion are the major forces in the field of the uncertainty propagation and the global sensitivity analysis. They are initiated by the work of Wiener ¹ [68], which states that any second-order random field can be expanded as a generalized Fourier series in the form of orthogonal Hermite polynomials in terms of Gaussian random variables. The Hermite polynomials constitutes a complete basis in the Hilbert space $L^2(\mathcal{P})$. The resulting polynomial series converges in the mean-square sense due to the Cameron-Martin theorem [8], and the convergence rate of the spectral expansion depends on the distribution of the random variables that one seeks to represent. To obtain the optimal convergence for random variables following any kind of probability distribution, Xiu and Karniadakis [83] extended the Polynomial Chaos framework to the *generalized polynomial chaos* (gPC) expansion, where random variables following specific distributions are expanded by the corresponding set of polynomials from the Askey scheme [3]. For example, a uniformly distributed function is optimally represented by Legendre polynomials that are orthogonal with respect to the uniform measure. Table 2.3.1 shows the generalized polynomial chaos which provide an optimal basis for different continuous probability distribution types.

Table 2.3.1: **Correspondence between different types of continuous probability distributions and the orthogonal polynomials from the Askey scheme**

Distribution	Density function	Polynomial	Weight function	Support range
Normal	$\frac{1}{\sqrt{2\pi}} e^{-\frac{x^2}{2}}$	Hermite $He_n(x)$	$e^{-\frac{x^2}{2}}$	$[-\infty, \infty]$
Beta	$\frac{(1-x)^\alpha (1+x)^\beta}{2^{\alpha+\beta+1} B(\alpha+1, \beta+1)}$	Jacobi $P_n^{(\alpha, \beta)}(x)$	$(1-x)^\alpha (1+x)^\beta$	$[-1, 1]$
Uniform	$\frac{1}{2}$	Legendre $p_n(x)$	1	$[-1, 1]$
Exponential	e^{-x}	Laguerre $L_n(x)$	e^{-x}	$[0, \infty]$

The spectral gPC approach can achieve optimal convergence provided the probability law of the QOI is known. However, this is not the case for general predictions with uncertainties since the explicit form of the QOI $u(\boldsymbol{\xi}, \mathbf{x}, t)$ in terms of uncertain input $\boldsymbol{\xi}$ is unknown. Therefore, the problem arises how to choose the optimal orthogonal polynomial basis we should choose arises. Nonetheless, as stated in [43], at least the probability distributions of the model uncertain inputs that we try to propagate are known, so people usually utilize the optimal basis based on the known distribution associated with those random parameters.

¹The original Wiener polynomial chaos is presented in Appendix A

2.3.1 Spectral expansion with gPC basis

The gPC expansion is to represent the QOI $u(\boldsymbol{\xi})$ in terms of orthogonal polynomial basis $\{\Psi_j(\boldsymbol{\xi})\}_{j=0}^{\infty}$ in the stochastic space Ξ :

$$u(\boldsymbol{\xi}, \mathbf{x}, t) \approx u_P(\boldsymbol{\xi}, \mathbf{x}, t) = \sum_{j=0}^{\infty} u_j(\mathbf{x}, t) \Psi_j(\boldsymbol{\xi}), \quad (2.3.1)$$

This gPC expansion divides the model response into a deterministic part and a stochastic part, *i.e.*, the coefficients $u_i(\mathbf{x}, t)$ and the polynomial chaos $\Psi_i(\boldsymbol{\xi})$ respectively. The coefficients $u_i(\mathbf{x}, t)$ are determined by the physical space. The randomness of uncertain inputs $\boldsymbol{\xi}$ is transferred into the gPC basis.

Choice of independent random variables

In this thesis, the random variables are assumed to be independent, which is a desirable property for multi-dimensional problem. This widely adopted assumption allows the tensor product construction of the multi-dimensional polynomial basis and the corresponding weighting function. The desired multi-dimensional orthogonality properties can be inherited from the univariate polynomial basis, *i.e.*, the basis functions $\{\Psi_j(\boldsymbol{\xi})\}_{j=0}^{\infty}$ are orthogonal with respect to the joint probability measure $\rho(\boldsymbol{\xi})$

$$\langle \Psi_i, \Psi_j \rangle = \int_{\Xi} \Psi_i(\boldsymbol{\xi}) \Psi_j(\boldsymbol{\xi}) \rho(\boldsymbol{\xi}) d\boldsymbol{\xi} = \langle \Psi_i^2 \rangle \delta_{ij}. \quad (2.3.2)$$

The above multi-dimensional inner product vanishes if any of the one-dimensional inner product is zero. What's more, when the expansion coefficients are solved by the orthogonal projection, the multivariate quadrature rules follow from the tensor products of the one-dimensional quadrature rules. It should be noted that the mutual independence is not a very strong requirement. If the input uncertainties are correlated or have arbitrary distributions that are not covered in the Askey scheme, we can apply "Gram-Schmidt" orthogonalization for computing the optimal orthogonal polynomial basis for any type of input distribution [71].

Construction of multi-dimensional gPC basis

For system involving single random variable ξ , one-dimensional polynomial chaos basis $\psi(\xi)$ can be selected from the Askey scheme. For instance, the first few Legendre polynomials corresponding to the uniform distribution are:

$$\begin{aligned} \psi_0(\xi) &= 1, \\ \psi_1(\xi) &= \xi, \\ \psi_2(\xi) &= \frac{1}{2}(3\xi^2 - 1), \\ \psi_3(\xi) &= \frac{1}{2}(5\xi^3 - 3\xi). \end{aligned} \quad (2.3.3)$$

For N -dimensional parameter space Ξ , if we can take advantage of the component independence of random vector $\boldsymbol{\xi} = \{\xi_1, \dots, \xi_N\}$, then the general polynomial chaos Γ_p of order p is constructed through the product of 1-D gPC basis. Let $\mathbf{i} = (i_1 + \dots + i_N) \in \mathbb{N}_0^N$ be a multi-index with $|\mathbf{i}| = i_1 + \dots + i_N$. The N -variate p -th order polynomial chaos is:

$$\Gamma_p = \left\{ \bigcup_{|\mathbf{i}|=p} \prod_{k=1}^N \psi_{i_k}(\xi_k) \right\}, \quad (2.3.4)$$

where the optimal univariate basis $\psi_{i_k}(\xi_k)$ is chosen for the corresponding random variable ξ_k . The linear space $\bar{\Gamma}_p$ spanned by Γ_p has dimension $\binom{N+p-1}{p}$. For example, the 2-D expansion can be written as:

$$\begin{aligned} u(\boldsymbol{\xi}) = & a_0\psi_0 + a_1\psi_1(\xi_1) + a_2\psi_1(\xi_2) \\ & + a_{11}\psi_2(\xi_1) + a_{21}\psi_1(\xi_2)\psi_1(\xi_1) + a_{22}\psi_2(\xi_2) \\ & + a_{111}\psi_3(\xi_1) + a_{211}\psi_1(\xi_2)\psi_2(\xi_1) + a_{221}\psi_2(\xi_2)\psi_1(\xi_1) + a_{222}\psi_3(\xi_2) \\ & + \dots \end{aligned} \quad (2.3.5)$$

For the sake of the notational convenience and the practical implementation, the above order based expression is simplified in the form of term-based expression like (2.3.1), where there is a one-to-one correspondence between the functional $\Psi(\cdot)$ and $\Gamma(\cdot)$, and also the coefficients u_j and $a_{i_1 i_2 \dots i_n}$. A popular choice for this transform is *graded lexicographic order*, where $\mathbf{i} > \mathbf{j}$ if and only if $|\mathbf{i}| \geq |\mathbf{j}|$ and the first non-zero entry in the difference, $\mathbf{i} - \mathbf{j}$, is negative [80]. Then, the term-based multi-dimensional chaos basis is:

$$\Psi_j(\boldsymbol{\xi}) = \prod_{k=1}^N \psi_{i_k^j}(\xi_k), \quad (2.3.6)$$

where the superscript j in multi-index i_k denotes the j -th term-based basis Ψ_j . A 2-D example of the graded lexicographic order is shown in the Table 2.3.2.

Table 2.3.2: Example of graded lexicographic order of multi-index \mathbf{i} for the 2-D case

order $p = \mathbf{i} $	Multi-index \mathbf{i}	Single-index j
0	(0 0)	0
1	(1 0)	1
	(0 1)	2
2	(2 0)	3
	(1 1)	4
	(0 2)	5
3	(3 0)	6
	(2 1)	7
	(1 2)	8
	(0 3)	9
...

Then, the first few multivariate Legendre polynomials for a 2-D case ($\boldsymbol{\xi} = (\xi_1, \xi_2)$) are:

$$\begin{aligned}\Psi_0(\boldsymbol{\xi}) &= \psi_0(\xi_1)\psi_0(\xi_2) = 1 \\ \Psi_1(\boldsymbol{\xi}) &= \psi_1(\xi_1)\psi_0(\xi_2) = \xi_1 \\ \Psi_2(\boldsymbol{\xi}) &= \psi_0(\xi_1)\psi_1(\xi_2) = \xi_2 \\ \Psi_3(\boldsymbol{\xi}) &= \psi_2(\xi_1)\psi_0(\xi_2) = \frac{1}{2}(3\xi_1^2 - 1) \\ \Psi_4(\boldsymbol{\xi}) &= \psi_1(\xi_1)\psi_1(\xi_2) = \xi_1\xi_2 \\ \Psi_5(\boldsymbol{\xi}) &= \psi_0(\xi_1)\psi_2(\xi_2) = \frac{1}{2}(3\xi_2^2 - 1)\end{aligned}$$

Expansion truncation

Suppose a generalized chaos basis $\{\Psi_j(\boldsymbol{\xi})\}_{j=0}^{\infty}$ is given for the random variables $\boldsymbol{\xi} \in \Xi$. For the computational purpose, a truncated subspace of $\{\Psi_j(\boldsymbol{\xi})\}_{j=0}^{\infty}$ is needed. Under the circumstance that no prior knowledge about the importance of different random variables is available, a usual approach is to truncate the infinite dimension polynomial basis to a certain total order P , *i.e.*, to take all possible combinations of the multi-index i_k satisfying $\sum_{k=1}^N i_k \leq P$, then the spectral expansion of QOI with infinite terms reduces to a finite number of $M + 1$ terms:

$$u(\boldsymbol{\xi}, \mathbf{x}, t) \approx u_P(\boldsymbol{\xi}, \mathbf{x}, t) = \sum_{i=0}^M u_i(\mathbf{x}, t)\Psi_i(\boldsymbol{\xi}), \quad (2.3.7)$$

where M satisfies:

$$M + 1 = \frac{(N + P)!}{N!P!}. \quad (2.3.8)$$

If the QOI have different sensitivities to different random variables, the expansion truncation should be adjusted to make sure that the sensitive dimensions have a higher order of polynomial chaos basis than the insensitive dimensions.

2.3.2 Stochastic Galerkin methods (SGM)

To solve the coefficients $u_i(\mathbf{x}, t)$ of the spectral expansion $u_P(\boldsymbol{\xi}, \mathbf{x}, t)$, one approach is the Stochastic Galerkin method [27]. It is an intrusive method in the sense that the mathematical formulation of the computational model needs to be changed. Consequently, modifications of existing deterministic codes are required, in contrast to the sampling based techniques and non-intrusive methods.

To apply the Galerkin projection, the governing equation (2.1.1) is multiplied by $\Psi_j(\boldsymbol{\xi})$ and integrated over the stochastic space:

$$\int_{\Xi} \rho(\boldsymbol{\xi})\mathcal{L}(\boldsymbol{\xi}, \mathbf{x}, t; u_P(\boldsymbol{\xi}, \mathbf{x}, t))\Psi_j(\boldsymbol{\xi})d\boldsymbol{\xi} = \int_{\Xi} \rho(\boldsymbol{\xi})\mathcal{S}(\boldsymbol{\xi}, t, \mathbf{x})\Psi_j(\boldsymbol{\xi})d\boldsymbol{\xi}, \quad \forall j \in \{0, \dots, M\}. \quad (2.3.9)$$

Consequently, the residual of (2.3.9) is orthogonal to the subspace spanned by $\{\Psi_i\}_{i=0}^M$. Finally, we obtain a system of $M + 1$ coupled deterministic equations in the physical domain \mathcal{D} , which can be achieved by a standard discretization technique.

The Stochastic Galerkin method was successfully applied to various engineering problems [84, 81, 85]. Spectral convergence with respect to the polynomial order can be achieved when the stochastic response are sufficiently smooth. Details of priori error estimates and convergence analysis were given by Babuška *et al.* [4] for elliptic partial differential equations. Although endowed with rigorous mathematical framework, Galerkin-based intrusive methods are more cumbersome to implement for complex problems, such as the full-scale Navier-Stokes simulation of 3-D flows or multi-system simulations with different deterministic codes. To determine the coefficients in the spectral expansion, all dependent variables in the governing equations are substituted by their polynomial chaos expansions. As a result, the whole existing code needs to be re-written. What's worse, every time when a new random parameter is included in the system, the solutions need to be re-calculated and the coupled system of equations need additional work.

2.3.3 Non-intrusive spectral projection methods

Apart from the Stochastic Galerkin method, there are other non-intrusive UQ methods to solve the spectral coefficients, which rely on repeated runs of the deterministic solver at a prescribed set of nodes in the parameter space. The existing deterministic solver can be used as a black box that associates each uncertain parameter ξ to the model output $u(\xi)$.

Recall that the spectral expansion of a second-order random variable $u(\xi)$ on a finite dimensional stochastic subspace of $L^2(\mathcal{P})$:

$$u(\xi) = \sum_{i=0}^M u_i \Psi_i(\xi).$$

By the virtue of the orthogonality and completeness of the basis, the projection coefficients u_i is given by:

$$u_i = \frac{\langle u(\xi), \Psi_i(\xi) \rangle}{\langle \Psi_i(\xi)^2 \rangle} = \frac{1}{\langle \Psi_i(\xi)^2 \rangle} \int_{\Xi} u(\xi) \Psi_i(\xi) \rho(\xi) d\xi. \quad (2.3.10)$$

The denominator in equation(2.3.10) can be computed analytically for multivariate orthogonal polynomials using the product of the square of univariate norms,

$$\langle \Psi_j(\xi)^2 \rangle = \prod_{k=1}^N \langle \psi_{i_k}^j(\xi_k)^2 \rangle. \quad (2.3.11)$$

So the main issue is to evaluate the multidimensional integral (2.3.10). The selection of sampling points for deterministic code evaluations categorizes the non-intrusive techniques into the following two approaches.

Monte Carlo sampling projection

The simplest approach to evaluate of the integral is Monte Carlo method:

$$u_i(\mathbf{x}, t) = \frac{1}{\langle \Psi_i(\boldsymbol{\xi})^2 \rangle \cdot n_{mc}} \sum_{k=1}^{n_{mc}} u(\mathbf{x}, t, \boldsymbol{\xi}_k) \Psi_i(\boldsymbol{\xi}_k). \quad (2.3.12)$$

This random sampling method is well suitable for high-dimensional problems, since the convergence rate is independent of the number of random variables. Application of this method to reacting flow can be found in [57].

Quadrature based projection

Another approach to evaluate the integral is to use Gauss quadrature rules. This method can effectively reduce the number of sampling points in the parameter domain for low-dimensional problems. For one-dimensional integral, we can choose Gaussian quadrature points based on the distribution of the random variables (e.g., Gauss-Hermite, Gauss-Legendre and Gauss-Laguerre for normal, uniform and exponential distributions respectively). The 1-D quadrature rule can be extended to the high-dimensional space via either full or sparse tensor products of one-dimensional quadrature rule. Then the coefficients $u_i(\mathbf{x}, t)$ can be approximated as:

$$\begin{aligned} u_i(\mathbf{x}, t) &= \frac{1}{\langle \Psi_i(\boldsymbol{\xi})^2 \rangle} \int_{\Xi} u(\boldsymbol{\xi}, \mathbf{x}, t) \Psi_i(\boldsymbol{\xi}) \rho(\boldsymbol{\xi}) d\boldsymbol{\xi} \\ &\approx \hat{u}_i(\mathbf{x}, t) = \frac{1}{\langle \Psi_i(\boldsymbol{\xi})^2 \rangle} \sum_{k=1}^{n_s} w_k u(\mathbf{x}, t, \boldsymbol{\xi}_k) \Psi_i(\boldsymbol{\xi}_k), \end{aligned} \quad (2.3.13)$$

where $\boldsymbol{\xi}_k$ are the quadrature points, which are the roots of orthogonal polynomials, w_k are quadrature weights.

Regarding error, projection methods involve two approximations. One arises from the finite term truncation to (2.3.7), the other is due to the approximation to the exact continuous orthogonal PC projection (2.3.10). The difference between the continuous orthogonal projection and the discrete projection is termed as *aliasing error* [79]. It was proved that $\hat{u}(\boldsymbol{\xi}, \mathbf{x}, t) = \sum_{i=0}^M \hat{u}_i(\mathbf{x}, t) \Psi_i(\boldsymbol{\xi})$ converges to $u(\boldsymbol{\xi}, \mathbf{x}, t)$ as $M \rightarrow \infty$ and $n_s \rightarrow \infty$ provided the quadrature rule is convergent.

To sum up, gPC based projection methods can be viewed as a post-processing step after the realizations at the sampling nodes or prescribed quadrature nodes. In contrast to the intrusive Stochastic Galerkin method, where all the coefficients are coupled and solved simultaneously, one can compute particularly interested expansion coefficients without evaluating the rest.

2.3.4 Interpolation approach based on gPC basis

Another way to construct the approximation of response surface $u(\boldsymbol{\xi})$ is to use polynomial interpolation. We start by prescribing a set of $M+1$ sampling points $(\boldsymbol{\xi}_k = \{\xi_1, \xi_2, \dots, \xi_N\}_k, k =$

$0, 1, 2, \dots, M$) in parameter space Ξ for a set of given PC basis $\{\Psi_i(\boldsymbol{\xi})\}_{i=0}^M$. Then run the deterministic codes evaluated at those points. The interpolation condition $u(\boldsymbol{\xi}_k, \mathbf{x}, t) = \sum_{i=0}^M u_i(\mathbf{x}, t)\Psi_i(\boldsymbol{\xi}_k)$, ($k = 0, 1, 2, \dots, M$) results in the following linear system:

$$\begin{pmatrix} \Psi_0(\boldsymbol{\xi}_0) & \Psi_1(\boldsymbol{\xi}_0) & \cdots & \Psi_M(\boldsymbol{\xi}_0) \\ \Psi_0(\boldsymbol{\xi}_1) & \Psi_1(\boldsymbol{\xi}_1) & \cdots & \Psi_M(\boldsymbol{\xi}_1) \\ \vdots & \vdots & \ddots & \vdots \\ \Psi_0(\boldsymbol{\xi}_M) & \Psi_1(\boldsymbol{\xi}_M) & \cdots & \Psi_M(\boldsymbol{\xi}_M) \end{pmatrix} \begin{pmatrix} u_0(\mathbf{x}, t) \\ u_1(\mathbf{x}, t) \\ \vdots \\ u_M(\mathbf{x}, t) \end{pmatrix} = \begin{pmatrix} u(\boldsymbol{\xi}_0, \mathbf{x}, t) \\ u(\boldsymbol{\xi}_1, \mathbf{x}, t) \\ \vdots \\ u(\boldsymbol{\xi}_M, \mathbf{x}, t) \end{pmatrix} \quad (2.3.14)$$

A core issue of this approach is the choice of sampling points, since it has a decisive impact on the interpolation error even though the error is zero at interpolation points. Hosder *et al.* [35] have investigated performance of three different sampling techniques, Random, Latin Hypercube, and Hammersley, in terms of the accuracy and the efficiency. It is shown that the Hammersley and Latin Hypercube sampling achieve a smoother convergence compared to the random sampling.

Oversampling is usually recommended for the robustness against noisy samples, then the linear system (2.3.14) becomes over-determined, which is solved by the Least Square approach. It has been observed [35] that more than twice number of collocation points than the number of the polynomial basis yields a better result in terms of the statistics of the solutions.

2.3.5 Statistics of solutions

The statistics of the QOI can be computed free from the known spectral expansion. The mean of $u(\boldsymbol{\xi}, \mathbf{x}, t)$ can be approximated as:

$$\begin{aligned} \mu_u(\mathbf{x}, t) &:= \mathbb{E}[u(\boldsymbol{\xi}, \mathbf{x}, t)] \approx \mathbb{E}[u_P(\boldsymbol{\xi}, \mathbf{x}, t)] = \mathbb{E}\left[\sum_{i=0}^M u_i(\mathbf{x}, t)\Psi_i\right] \\ &= u_0(\mathbf{x}, t)\mathbb{E}[\Psi_0] + \sum_{i=1}^M u_i(\mathbf{x}, t)\mathbb{E}[\Psi_i] = u_0(\mathbf{x}, t), \end{aligned} \quad (2.3.15)$$

following the fact that $\langle \Psi_i \rangle = 0$ for $j > 0$. Therefore, the zeroth mode of the expansion corresponds to the expectation. The second moments, *e.g.*, the covariance function for any $\mathbf{x}_1, \mathbf{x}_2 \in D$:

$$\begin{aligned} C_u(\mathbf{x}_1, \mathbf{x}_2) &:= \mathbb{E}[(u(\boldsymbol{\xi}, \mathbf{x}_1, t) - \mu_u(\mathbf{x}_1, t))(u(\boldsymbol{\xi}, \mathbf{x}_2, t) - \mu_u(\mathbf{x}_2, t))] \\ &\approx \mathbb{E}[(u_P(\boldsymbol{\xi}, \mathbf{x}_1, t) - u_0(\mathbf{x}_1, t))(u_P(\boldsymbol{\xi}, \mathbf{x}_2, t) - u_0(\mathbf{x}_2, t))] \\ &= \sum_{i=1}^M [u_i(\mathbf{x}_1, t)u_i(\mathbf{x}_2, t)\langle \Psi_i^2 \rangle]. \end{aligned} \quad (2.3.16)$$

The correlation function is:

$$\begin{aligned} R_u(\mathbf{x}_1, \mathbf{x}_2) &:= \mathbb{E}[u(\boldsymbol{\xi}, \mathbf{x}_1, t)u(\boldsymbol{\xi}, \mathbf{x}_2, t)] \\ &\approx \mathbb{E}[u_P(\boldsymbol{\xi}, \mathbf{x}_1, t)u_P(\boldsymbol{\xi}, \mathbf{x}_2, t)] \\ &= \sum_{i=0}^M [u_i(\mathbf{x}_1, t)u_i(\mathbf{x}_2, t)\langle \Psi_i^2 \rangle]. \end{aligned} \quad (2.3.17)$$

The variance of $u(\boldsymbol{\xi}, \mathbf{x}, t)$ for any $\mathbf{x} \in D, t \in T$ is:

$$\begin{aligned} \sigma_u^2(\mathbf{x}, t) &:= \mathbb{E}[(u(\boldsymbol{\xi}, \mathbf{x}, t) - \mu_u(\mathbf{x}, t))^2] \\ &\approx \sum_{i=1}^M u_i^2(\mathbf{x}, t) \mathbb{E}[\Psi_i^2] = \sum_{i=1}^M u_i^2(\mathbf{x}, t) \langle \Psi_i^2 \rangle. \end{aligned} \quad (2.3.18)$$

2.4 Stochastic Collocation method

Stochastic Collocation (SC) is a non-intrusive method to propagate uncertainties through a complex model when a high-fidelity deterministic code is available. It is termed *Stochastic Collocation Method* (SC) due to the pioneering work of Mathelin and Hussaini [51]. Later, many researchers, to name a few, Xiu and Hesthaven [82], Nobile *et al.* [55, 54], Loeven *et al.* [46], Ma and Zabarar [48, 49] improve this method in different aspects.

The key idea of the stochastic collocation approach is to construct the approximating model response $u(\boldsymbol{\xi})$ by interpolating its deterministic values at a pre-specified set of points in the stochastic space, which are called the collocation points. Let $\Theta_N := \{\boldsymbol{\xi}_m\}_{m=1}^{n_s} \in \Xi$ be the prescribed set of nodes in N dimensional parameter space, where n_s is the total number of collocation nodes. The spectral expansion of the approximated solution is formed as a sum of multi-dimensional Lagrange interpolation polynomials:

$$u(\boldsymbol{\xi}, \mathbf{x}, t) \approx \mathcal{I}(u(\boldsymbol{\xi})) = \sum_{m=1}^{n_s} u(\boldsymbol{\xi}_m, \mathbf{x}, t) \mathbf{L}_m(\boldsymbol{\xi}). \quad (2.4.1)$$

The spectral coefficients $u(\boldsymbol{\xi}_m, \mathbf{x}, t)$ are the response values at each of the collocation points, where a deterministic problem is solved. To simplify the notation, the spatial coordinate \mathbf{x} and temporal coordinate t are dropped from here on.

Different from the non-intrusive gPC projection approach, where the expansion coefficients are estimated for the known basis functions, the SC method constructs the polynomial basis from the pre-specified collocation points. The approximation quality and the convergence properties depend critically on the choice of collocation points for sample realizations. Taking advantage of the well-established approximation theory [63, 64], one popular choice of the sampling points is the nested Clenshaw-Curtis nodes, which also are the extrema of Chebyshev polynomials. They are defined as :

$$\xi_j^i = -\cos\left(\frac{\pi(j-1)}{s_i-1}\right), \quad j = 1, \dots, s_i, \quad (2.4.2)$$

where single index $i \in \mathbb{N}$ denotes the level of interpolation, and s_i follows the following relations:

$$s_1 = 1 \quad \text{and} \quad s_i = 2^{i-1} + 1, \quad \text{for} \quad i > 1. \quad (2.4.3)$$

A nested set means that each subsequent set contains all elements of the previous set. It is an essential property for the hierarchical construction of the interpolant as well as the error estimate based on the hierarchical surplus. What's more, it enables us to use all obtained expensive deterministic results of previous levels if a further level of interpolation is needed. Another desirable property of the Chebyshev points is its immunity to the *Runge phenomenon* due to the small value of the Lebesgue constant.

2.4.1 Full tensor-product formulation for multi-dimensions

For the multivariate case, we use the multi-index $\mathbf{i}=(i_1, \dots, i_N) \in \mathbb{N}^N$ with $i_k(k=1, \dots, N)$ to denote the level of interpolation along the k -th dimension. $\xi_{j_k}^{i_k}$ is the j_k -th point in the k -th dimension.

First, we define $I_{s_i}^i$ as a one-dimensional interpolating operator for a smooth function $u : [-1, 1] \rightarrow \mathbb{R}$:

$$I_{s_i}^i(u(\xi)) = \sum_{j=1}^{s_i} u(\xi_j^i) L_j^i(\xi), \quad (2.4.4)$$

based on nodal sets

$$\Theta^i = (\xi_1^i, \dots, \xi_{s_i}^i) \subset [-1, 1], \quad (2.4.5)$$

where

$$L_j^i(\xi) = \prod_{k=1, k \neq j}^{s_i} \frac{\xi - \xi_k^i}{\xi_j^i - \xi_k^i} \quad (2.4.6)$$

such that $L_j^i(\xi_k^i) = \delta_{jk}$ with δ_{jk} as the Kronecker delta. Assume that one-dimensional interpolation formula (2.4.4) are given for each dimension $k(k=1, \dots, N)$, then the interpolation in the entire space $\Xi \subset [-1, 1]^N$ via tensor-product can be written as:

$$\begin{aligned} \mathcal{I}(u(\boldsymbol{\xi})) &= (I_{s_{i_1}}^{i_1} \otimes \dots \otimes I_{s_{i_N}}^{i_N})(u(\boldsymbol{\xi})) \\ &= \sum_{j_1=1}^{s_{i_1}} \dots \sum_{j_N=1}^{s_{i_N}} u(\xi_{j_1}^{i_1}, \dots, \xi_{j_N}^{i_N}) (L_{j_1}^{i_1} \otimes \dots \otimes L_{j_N}^{i_N}). \end{aligned} \quad (2.4.7)$$

s_{i_k} is the number of collocation points used in the k -th dimension. It should be mentioned that different levels and distribution of collocation points in each dimension can be used, which should be adjusted according to the importance of independent random parameters.

2.4.2 Conventional Sparse Grid formulation for multi-dimensions

From the full-tensor product formulations, we can observe that the total number of collocation points is $n_s = \prod_j^N s_{i_j}$, which shows an exponential increase with respect to the dimension N . This well-known numerical challenge *curse of dimensionality* would cause a prohibitive computational cost for the uncertainties propagation of large scale deterministic system. To combat the *curse of dimensionality* inherent to the full tensor-product formulation, the sparse grid approach based on the Smolyak algorithm [61] is incorporated into non-intrusive methods, including the collocation method and the spectral projection method. In contrast to the full tensor-product formulation that treats all dimensions and intersection terms equally, the isotropic sparse grid is a linear combination of subsets of the full tensor-product grid with the property that only low order interaction terms are considered [6]. Consequently, the number of nodes required for the interpolation is reduced by orders of magnitude. A parameter w called *level of approximation* ($w \in \mathbb{N}_0$) controls the polynomial basis coverage of the Smolyak grid.

Following the notations in Section 2.4.1, we define:

$$\Delta^i = I^i - I^{i-1}, \quad (2.4.8)$$

for $i \geq 1$ and set $I^0 = 0$. Then the Smolyak *isotropic* formulas $\mathcal{A}_{w,N}$ is given by:

$$\mathcal{A}_{w,N} = \sum_{|\mathbf{i}| \leq w+N} (\Delta^{i_1} \otimes \dots \otimes \Delta^{i_N}). \quad (2.4.9)$$

The multi-index $\mathbf{i}=(i_1, \dots, i_N) \in \mathbb{N}^N$ denotes the level of interpolation along each dimension. Let $|\mathbf{i}| = i_1 + \dots + i_N$. Equivalently, the above formula can be rewritten as [67]:

$$\mathcal{A}_{w,N} = \sum_{w+1 \leq |\mathbf{i}| \leq w+N} (-1)^{w+N-|\mathbf{i}|} \binom{N-1}{w+N-|\mathbf{i}|} \cdot (I^{i_1} \otimes \dots \otimes I^{i_N}). \quad (2.4.10)$$

To compute $\mathcal{A}_{w,N}$, we only need to evaluate function on the “sparse grid”:

$$\Theta_N \equiv \mathcal{H}_{w,N} = \bigcup_{w+1 \leq |\mathbf{i}| \leq w+N} (\Theta^{i_1} \times \dots \times \Theta^{i_N}), \quad (2.4.11)$$

where the set of abscissas used by I^i is:

$$\Theta^i = (\xi_1^i, \dots, \xi_{m_i}^i) \subset [-1, 1]. \quad (2.4.12)$$

If the nested Clenshaw-Curtis nodes are used, we have $\Theta^i \subset \Theta^{i+1}$ and thereby $\mathcal{H}_{w,N} \subset \mathcal{H}(w+1, N)$. Then (2.4.11) becomes:

$$\mathcal{H}_{w,N} = \bigcup_{|\mathbf{i}|=w+N} (\Theta^{i_1} \times \dots \times \Theta^{i_n}). \quad (2.4.13)$$

Comparison of the tensor and sparse grid of level $w = 4$ is illustrated in Figure 2.4.1. It can be observed that the sparse grid involves a significantly reduced number of points. The ratio of number of nodes for tensor and sparse grids increases with the dimension.

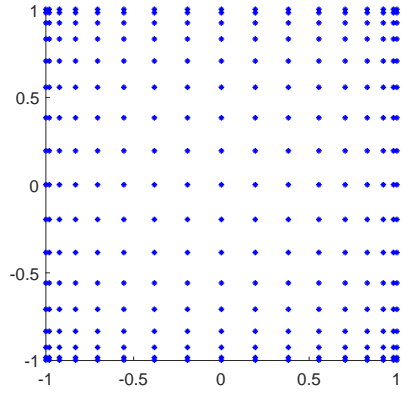
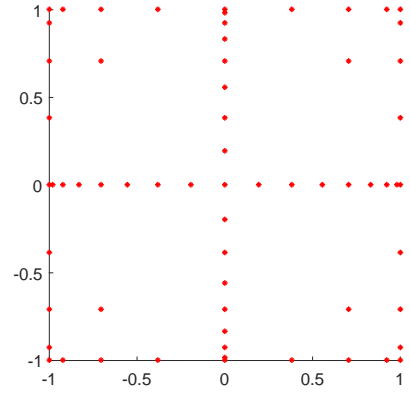
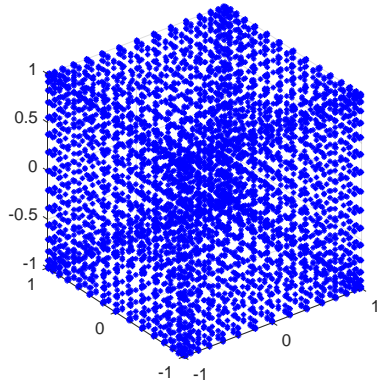
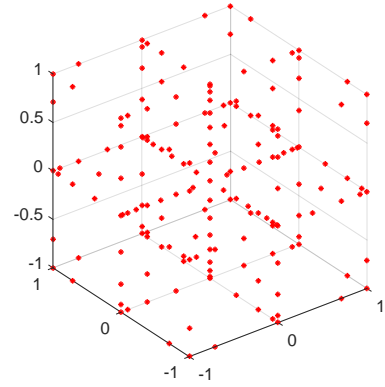
(a) $N = 2$, tensor grid, $n_s = 289$ (b) $N = 2$, sparse grid, $n_s = 65$ (c) $N = 3$, tensor grid, $n_s = 4913$ (d) $N = 3$, sparse grid, $n_s = 177$

Figure 2.4.1: Comparison of the tensor and the sparse grid of level $w = 4$ with the Clenshaw-Curtis abscissas.

As for the interpolation error, we consider the function space:

$$F_N^l = \{f : [-1, 1]^N \rightarrow \mathbb{R} \mid \partial^{|\mathbf{s}|} f \text{ continuous, } s_i \leq l, \forall i\} \quad (2.4.14)$$

where $\mathbf{s} \in \mathbb{N}^N$ and $\partial^{|\mathbf{s}|}$ is the usual N -variate partial derivative of order $|\mathbf{s}|$. Then, the interpolation error in terms of the maximum norm follows [6]:

$$\|f - \mathcal{A}_{w,N}(f)\|_\infty \leq C_{N,l} \cdot M^{-l} \cdot (\log M)^{(l+2)(N-1)+1}, \quad (2.4.15)$$

where $M = \dim(\mathcal{H}_{w,N})$ is the number of interpolation points. For analytic functions ($l \rightarrow \infty$), the convergence will be exponential. However, despite the improvement over the full tensor product grids, the sparse grid still suffer from the curse of dimensionality due to the dependence on the dimension in the logarithmic terms.

2.5 Motivation for a new approach

The aforementioned non-statistical methods rely on the spectral expansion using the polynomial basis. Therefore, the convergence rate depends on two factors: the smoothness of the underlying function and the dimensionality of the parameter space. For general computational models governed by non-linear conservation laws, which are usually encountered in fluid dynamics, the convergence is usually less favorable since the smooth requirement cannot be met. More often than not, many physical phenomena are represented by piecewise smooth functions. The steep gradients or discontinuities in the physical space, *e.g.*, shock waves in hypersonic flow field would result in their counterparts in the stochastic space. Therefore, the spectral expansions may yield the Gibbs oscillations in the stochastic space, as shown in Figure 2.5.1. There are following features associated with the *Gibbs phenomenon* [29, 30, 9]:

- The oscillation away from the discontinuity decays rather slowly. The error at a fixed location ξ decreases as $O(n^{-1})$, where n is the order of the polynomial basis.
- The overshoots and undershoots near the discontinuity do not diminish with increasing level of approximation, *i.e.*, the infinity error stays almost constant with respect to n .
- The integral error L_p for $p \geq 1$ decreases as $O(n^{-\frac{1}{p}})$

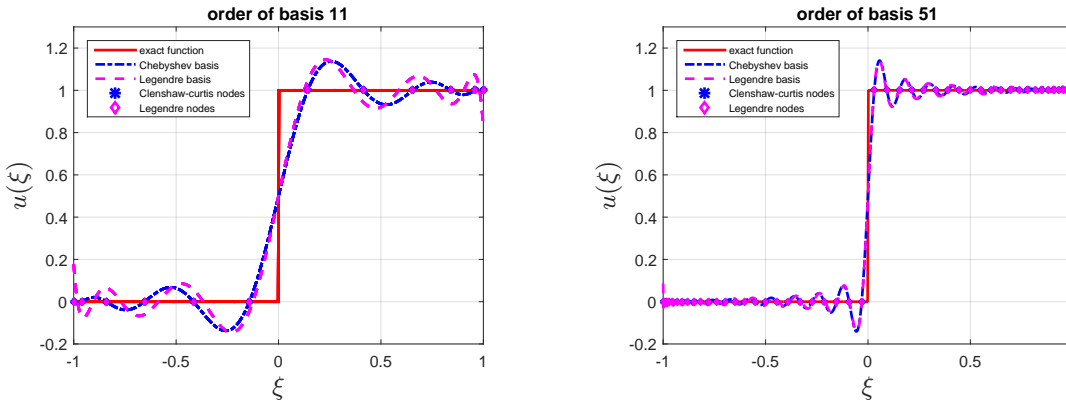


Figure 2.5.1: Gibbs phenomenon

These oscillations naturally enlarge the interval of model response in the stochastic space. For certain values of uncertain inputs ξ , the resulting output $u(\xi)$ may stand for some non-physical quantities such as the negative static pressure. The situation becomes even worse for time-dependent problems (*e.g.*, fluid-structure interaction problems), where *stochastic drift* [25] may become unacceptably large during the long-term time integration. To circumvent the difficulty of approximating discontinuous function, methods based on discretization of the parameter space were developed. The piecewise polynomial basis with local supports are utilized to ensure the convergence in the smooth region, similar to what has been done in deterministic numerical methods.

In [19, 5], finite element basis functions were used in the random space to approximate locally the stochastic dependence of the solution. The wavelet basis expansion method was also utilized to address this problem [44, 45]. It relies on an orthogonal projection of uncertain data and solution variables onto a multi-wavelet basis. A Galerkin procedure in the parameter space is employed to compute the coefficients of the expansion, which inevitably transform the corresponding stochastic equations to a set of coupled deterministic algebraic equations.

The multi-element generalized polynomial chaos method (MEgPC) [65, 66] was introduced to address discontinuities in the random space while preserving the convergence rate of the gPC method. The main idea of MEgPC is to decompose the space of random inputs into small elements. The local decay rate of the variance and the element size were used as indicators to split a random element into two equal parts when a certain condition is met. Subsequently, in each sub-element a new random variable with respect to a conditional probability density function (PDF) is defined, then the generalized polynomial chaos (gPC) method with orthogonal basis is implemented element by element. Since the degree of perturbation in each element is reduced proportionally to the size of random elements, a low order gPC basis in each element is enough to maintain the desired accuracy. Finally, the local solutions in all elements are summed up to form the global approximation. Due to the element-wise approximation, the undesirable Gibbs oscillation are confined a limited number of elements surrounding the discontinuities and the approximation away from the discontinuities is able to maintain the high accuracy. To avoid computational complexity of the Galerkin projection, which increases with the number of stochastic dimensions and the number of expansion terms, the authors in [65, 66] later extended (MEgPC) to the multi-element probabilistic collocation method (ME-PCM) [22], where tensor product or sparse grid collocation is used in each element.

A similar adaptive approach based on Newton-Cotes quadrature in simplex elements was proposed in [78]. In this approach, the stochastic response is approximated by a piecewise polynomial by subdividing the parameter space into simplex elements. The Newton-Cotes quadrature rule is employed in the approximation of the statistical moments. The elements are refined adaptively using a refinement measure based on the curvature of the approximating response weighted by the probability represented by the element.

As a matter of fact, efficient localization of discontinuities has been an active research topic in many scientific computing fields. It is called *edge detection* in image processing. There have been many traditional edge detection methods. One recent method called *polynomial annihilation edge detection* [1] gains popularity. It is based on local Taylor expansions like the traditional ENO or WENO scheme. A high order reconstruction of the jump function is obtained based on the global approximation of sampling nodes. The order of reconstruction needs to be specified in advance and it affects the resolution of the jump function. The edges are identified by comparing the values of jump function and a certain threshold value. Taking advantage of the polynomial annihilation edge detection method, a different methodology dealing with discontinuous functions was proposed in [38] recently. The novel feature of this method is that the parameter space is partitioned into multiple elements defined by the underlying discontinuities, in direct contrast to the traditional multi-element methods where the sub-domains are obtained by splitting the axes in the parameter space [38]. To resolve the discontinuities, a discontinuities detector is employed, which is based on the

combination of the polynomial annihilation edge detection and the adaptive sparse grid. After the decomposition of the whole parameter space, the surrogate in each element is constructed by the least orthogonal interpolation method [53].

For UQ applications to industrial problems, it happens that more than one QOI from the same computational model are wanted for a better understanding of the effects of the uncertainties. More often than not, different QOI has different smoothness property in the random space, *e.g.*, the static pressure at various physical locations around the airfoil surface. Under such circumstances, the adaptive methods need different deterministic sampling values for distinctive QOI. This would result in a huge computational cost.

Apart from the above mentioned adaptive methods dealing with discontinuities, a novel spectral method called iterative generalized polynomial chaos (i-gPC) was proposed in [56]. This method, with a post-processing nature, automatically builds a recursive approximation based on iterative formulations of the orthogonal polynomial basis with respect to the stochastic properties of the solutions. It has been shown that with increasing number of iterations and large number of quadrature points, the oscillations are restrained in the immediate vicinity of the discontinuity [56]. This method proves to be robust when compared with other non-intrusive methods on the Woodward-Colella benchmark of a high-speed channel flow with a forward step in [47]. Although no additional deterministic simulations/samples are needed during the whole process, the *aliasing error* may become large during the iterations.

To conclude, existing methods dealing with the discontinuous response in the parameter space have shown satisfactory results with regards to some computationally cheap models. However, a large number of sampling points or polynomial basis is needed to achieve a relatively good accuracy, which makes them impractical to use for time-consuming large scale CFD simulations under the case of limited computational resources. Besides this, most non-intrusive methods are based on adaptive refinements, making it impossible for parallelizations. Consequently, the whole process may take a long continuous time. For the economical purpose, a consistent non-adaptive method using the same set of deterministic sampling values to conduct the stochastic post-processing is needed. In the next chapter, the one-dimensional formulation of the proposed method is presented.

Chapter 3

Robust one-dimensional Stochastic Collocation with discontinuities detection

This chapter presents a novel non-adaptive Stochastic Collocation method with essentially non-oscillatory (ENO) robustness (SC-ENO), which is designed to eliminate the spurious oscillations associated with discontinuous response surface. The robustness concepts, such as Local Extremum Conserving (LEC), Monotonicity Preserving (MP), are incorporated into the non-intrusive Stochastic Collocation (SC) method with structured deterministic sampling points. The LEC limiter has been applied in the Simplex Stochastic Collocation (SSC) method [73, 74], where it is used to reduce the order of polynomial basis in each local simplex element. Different from the SSC method, the proposed method works on a structured sampling points. It first resolves the locations of discontinuities by the limiter, and then constructs high order surrogate inside each smooth sub-domains. In the following, robustness concepts from the CFD community are discussed in Section 3.1. Then, the novel approach is shown in Section 3.2. Another method for predicting the location of discontinuity in the parameter space is discussed in Section 3.3. Finally, the popular *polynomial annihilation edge detection* method and the proposed SC-ENO method are discussed in Section 3.4.

3.1 Robustness concepts from the CFD community

As we know, the classical spatial discretization methods, such as the finite difference and related finite volume methods, are based on local interpolations of data at discretized grids with polynomials or other simple functions. From the classical approximation theory, the order of accuracy of the interpolation is proportional to the number of nodes in the interpolation stencil, provided the function to be approximated is smooth. However, fixed interpolation stencil of second or higher order would result in *Gibbs oscillations* once it contains discontinuities.

In the past three decades, to deal with the piecewise smooth property of the generic solu-

tion for hyperbolic conservation laws, people have developed many robust methods to suppress the oscillations around the discontinuities. In 1987, ENO (Essentially Non-Oscillatory) scheme was proposed by Harten *et al.* [33], which is able to obtain the uniformly high order accurate and essentially non-oscillatory interpolation for piecewise smooth functions [60]. Based on the fact that the divided difference can measure the smoothness of the function inside the stencil, they utilized a hierarchy construction that begins with one or two cells, then adds one cell at a time to the stencil from the two candidates on the left and right based on the two values of the Newton divided differences. Although the ENO schemes are indeed uniformly high order accurate, it is not suitable for the uncertainty propagation problem due to the inherently different nature of spatial discretization and the non-intrusive sampling in the parameter space. Limited by the expensive computational cost of a single sampling for large scale CFD simulations, it is impractical to achieve convergence by a relatively fine mesh/grid/sampling or adaptive refinement. Consequently, the order of interpolation stencil cannot be maintained uniformly high across the whole random space. For example, if there are more than one discontinuities in the random space and they are close to each other, then the order of interpolation achieved by the classical ENO scheme is limited by the distance between the discontinuities in the parameter space.

Before ENO was developed, limiters were used to eliminate spurious oscillations. In effect, the order of polynomial basis near the discontinuities is reduced to linear. In [73, 74], reformulation of this kind of robustness principle was proposed with regards to the parameter space and Simplex Stochastic Collocation (SSC) method was developed. In the SSC method, the Local Extremum Conserving (LEC) limiter is used to control the size of the local interpolation stencil to avoid overshoots across the discontinuities. The adaptive refinement of sampling grid is controlled by a local error estimator which is based either on the root mean square of hierarchical surpluses or on the combination of the local probability measure and the polynomial order. Later, the ENO type stencil selection was introduced into the Simplex Stochastic Collocation (SSC) method [74]. For each simplex element in the stochastic space, the stencil with the highest polynomial degree is selected from the set of candidate stencils to construct the local response surface approximation. Consequently, the high order interpolation can be extended to the discontinuity locations. Recently, an improved version of SSC is proposed in [20], which is more efficient and suitable for high-dimensional problems.

Inspired by the SSC method, some robustness concepts from the CFD community are incorporated into the Stochastic Collocation method in an attempt to suppress the Gibbs oscillations. They are introduced in the following sections.

3.1.1 Local extremum conserving limiter

Like other non-intrusive UQ methods, firstly a set of samples $u(\boldsymbol{\xi}_k)$ are obtained by solving the deterministic problems at the structured sampling points $\boldsymbol{\xi}_k, k = 1, \dots, n_s$, where n_s is the total number of nodes. The whole parameter space Ξ can be viewed as a summation of elements $\Xi = \bigcup_J^{n_s-1} \Xi_J$, each of which is bounded by the sampling points $\boldsymbol{\xi}_k$. Then, approximation $w_J(\boldsymbol{\xi})$ is constructed for each element. The following definition is reproduced from [72].

Definition 3.1.1 (Local Extremum Conserving (LEC)). *Approximation $w_J(\boldsymbol{\xi})$ of sam-*

ples $u(\xi_k)$ in Ξ_J is LEC with respect to $u(\xi_k)$ in Ξ_J if

$$\min_{\xi \in \Xi_J} w_J(\xi) = \min_{\xi_k \in \Xi_J} u(\xi_k) \quad \wedge \quad \max_{\xi \in \Xi_J} w_J(\xi) = \max_{\xi_k \in \Xi_J} u(\xi_k). \quad (3.1.1)$$

Interpolation operator I is LEC in Ξ_J if the resulting approximation $w_J(\xi)$ is LEC with respect to $u(\xi_k)$ in Ξ_J for all $u(\xi_k)$.

Local approximation $w_J(\xi)$ for element Ξ_J using the sampling values at its vertices always satisfies LEC limiter. To aim for higher order polynomial basis, more sampling points are needed for the interpolation stencil of each element. However, oscillation appears whenever the stencil contains discontinuities or high gradients inside. In that case, the LEC limiter would not be satisfied and the reduction of the order is needed, as indicated in Figure 3.1.1. In this sense, the LEC limiter can preserve the monotonicity of the underlying function to some extent.

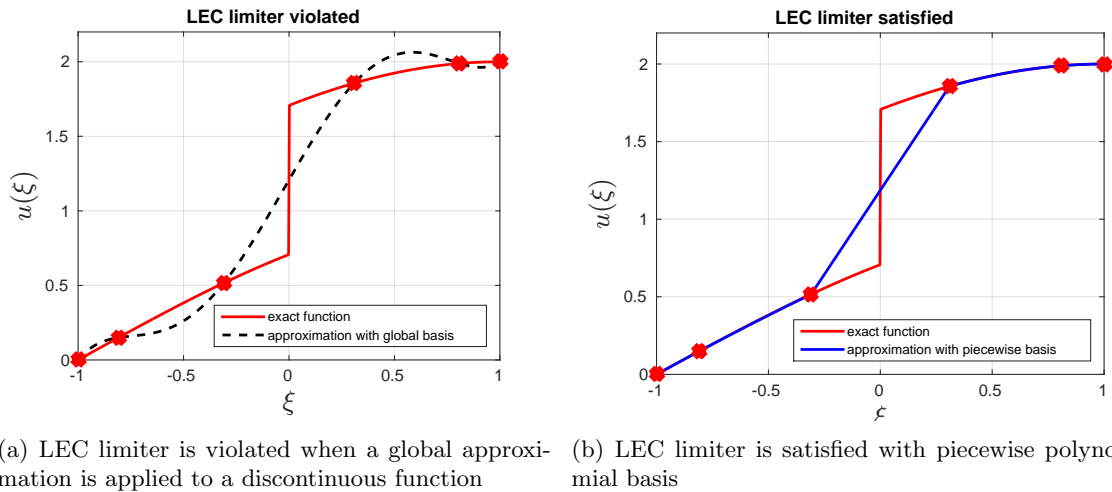


Figure 3.1.1: The LEC limiter forbids overshoots by reducing the polynomial order.

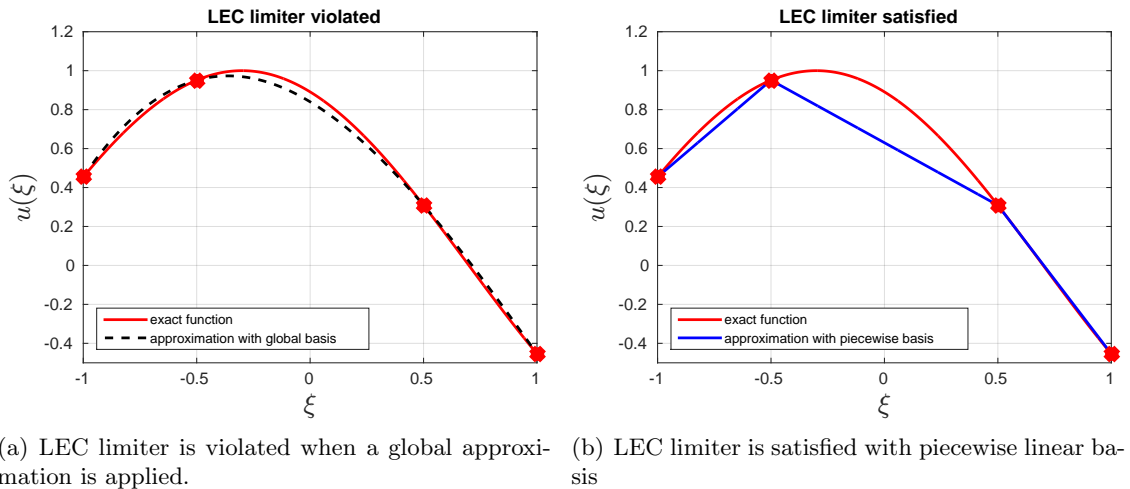


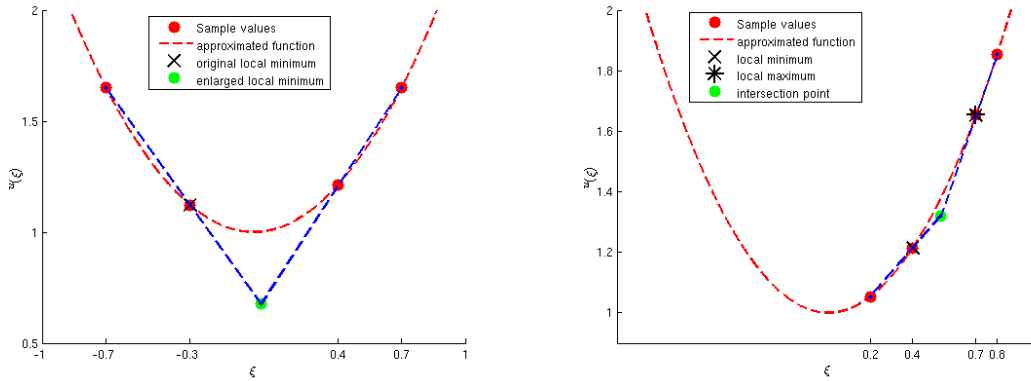
Figure 3.1.2: The LEC limiter forbids local smooth extrema.

However, the original LEC limiter has the disadvantage that it reduces interpolation to first-order accuracy for smooth non-monotonic functions at local extrema. To demonstrate this, we consider the following non-monotonic smooth test function: $u(\xi) = \sin\left(\frac{\pi}{2}(\xi + 1.3)\right)$. The plots are in Figure 3.1.2. As a result of the LEC limiter, the approximation is reduced to first-order.

3.1.2 Monotonicity Preserving limiter

To solve the problem of misinterpretation of smooth extrema as discontinuities, another robustness concept Monotonicity Preserving (MP) is introduced. To show how it works, we use a smooth non-monotonic quadratic function: $u(\xi) = \frac{4}{3}\xi^2 + 1$. For ease of clarification, we take four samples $\xi = [-0.7, -0.3, 0.4, 0.7]$ to construct the polynomial approximation.

Since the original LEC limiter does not allow overshoots in the approximating surrogate $w(\xi)$ with respect to the sample values $[u(-0.7), u(-0.3), u(0.4), u(0.7)]$, the approximation would be reduced to piecewise linear function around the local minimum at $\xi = 0$. Consequently, the interpolation error in the continuous element $[-0.3, 0.4]$ is not acceptable. To cope with that, we propose a modified LEC limiter, which enlarges the interval of the limiter automatically, *i.e.* the extremum of the sample values, near the real local extrema. A similar formulation is developed by Suresh and Huynh [62] in the context of the Monotonicity Preserving (MP) limiter in Finite Volume Methods. First, we seek the intersection points (ξ_{int}, u_{int}) of neighboring straight lines passing through two adjacent samples. Then the local extremum of each element $[\xi_J, \xi_{J+1}]$ is determined by comparing three values $[u_{int}, u(\xi_J), u(\xi_{J+1})]$ instead of the original two values $[u(\xi_J), u(\xi_{J+1})]$.



(a) Enlarged intervals of the LEC limiter for non-monotonic function (b) Unchanged intervals of the LEC limiter for monotonic function

Figure 3.1.3: The LEC limiter combined with monotonicity preserving concept

As we can see from Figure 3.1.3(a), the local minimum for the continuous element $[-0.3, 0.4]$ is changed from the original sample value $u(-0.3)$ to the green intersection point of two lines passing through neighbouring sample values. On the other hand, for smooth monotonic functions, the interval of the LEC limiter remains unchanged automatically because the intersection point u_{int} is between $[u(\xi_J), u(\xi_{J+1})]$, as can be seen in Figure 3.1.3(b). Compared

to an existing MP limiter [76], the modified LEC limiter does not need any threshold value to determine the existence of the smooth local extremum. It is expected to give the same robust results for both monotonic and non-monotonic functions. It should be noted that the enlarged interval of local extrema depends not only on the sample values $u(\xi_k)$ but also on the sampling nodes ξ_k . Therefore, a high oscillatory response surface is allowed if enough sampling points are given,

3.2 Stochastic Collocation with ENO robustness in 1-D

In classical spectral expansions of functions with a polynomial basis, the high-order terms determine the regularity of the approximation. For Lagrange interpolation, each polynomial basis has the same order, thus the same magnitude of variance. When a larger number of nodes is involved for interpolation, the interpolation becomes more capable to represent a continuous function with many extrema accurately. On the other hand, the fewer nodes are involved, the more robust the approximation becomes. Guided by this idea, essentially non-oscillatory property can be achieved by using the LEC limiter and MP limiter to limit the order of polynomial basis. Actually, for the 1-dimensional space, the process of constructing surrogate with the ENO property can also be viewed as a process of resolving discontinuities in the parameter space. In the following part, an efficient and robust methodology for detecting discontinuous elements is presented.

To resolve the discontinuities in one dimensional parameter space Ξ , we first perform Stochastic Collocation with a global basis as described in Section 2.4. The number of nodes s_i is determined by a given computational budget and desired accuracy requirement. Then, the space is partitioned into $s_i - 1$ elements, *i.e.*, $\Xi = \bigcup_{j=1}^{s_i-1} \Xi_j$. The term *element* used here is different from the one used in multi-element probabilistic collocation method (ME-PCM) [22, 65, 66], since no new polynomial basis is generated again inside each element and the sampling is global still.

The main computational cost is spent on the realization of samples $u(\xi_k)$ since it is fair to assume that manipulation of polynomial approximation is not expensive. The approximations $I(u(\xi_{mc,J}))$ at Monte Carlo integration points $\xi_{mc,J}, mc_J = 1, \dots, s_{mc,J}$ inside each element Ξ_j are used for computing the statistical moments of the solution and for the LEC limiter.

Then, if discontinuities exist in parameter space, the oscillations around it will trigger the LEC limiter. After that, the number of nodes will be dropped one by one until the remaining nodes $\{\xi_1, \xi_2, \dots, \xi_k\}, k < s_i$ produce a robust approximation of the elements enclosed by nodes ξ_1 and ξ_k . Here, ‘robust’ means that the LEC limiter is satisfied and undesired oscillations between each two nodes are suppressed. In practice, the dropping of nodes could start from either side of the interval $[\xi_1, \xi_{s_i}]$. However, it should be emphasized that ‘robust’ does not exclude naturally the discontinuities out of the interval $[\xi_1, \xi_k]$. In some rare cases, the LEC limiter could also be satisfied even if the discontinuity lies between nodes ξ_{k-1} and ξ_k . So the next step is to determine which side the discontinuity lies with

respect to the node ξ_k . Here, we employ a straightforward jump discontinuity detector, which is very similar to the shock detector used in discretization schemes in the CFD community. If sample values $|u(\xi_k) - u(\xi_{k+1})| < |u(\xi_k) - u(\xi_{k-1})|$, the discontinuity locates between ξ_{k-1} and ξ_k , and vice versa. Then, a first-order approximation is applied to the discontinuous element $\Xi_{disc_i}, disc_i \in \{1, \dots, s - 1\}$. This scanning process restart again for the elements which have been dropped before, *i.e.*, elements between nodes ξ_{disc_i+1} and ξ_s . This scanning process finishes until all elements in the whole parameter space Ξ have been interpolated ‘robustly’. Finally, the parameter space is partitioned into disjoint smooth elements with the discontinuous element as interface, and the global interpolation is replaced by piecewise interpolation. A pseudo-code is presented in alg. 1 for a better clarification.

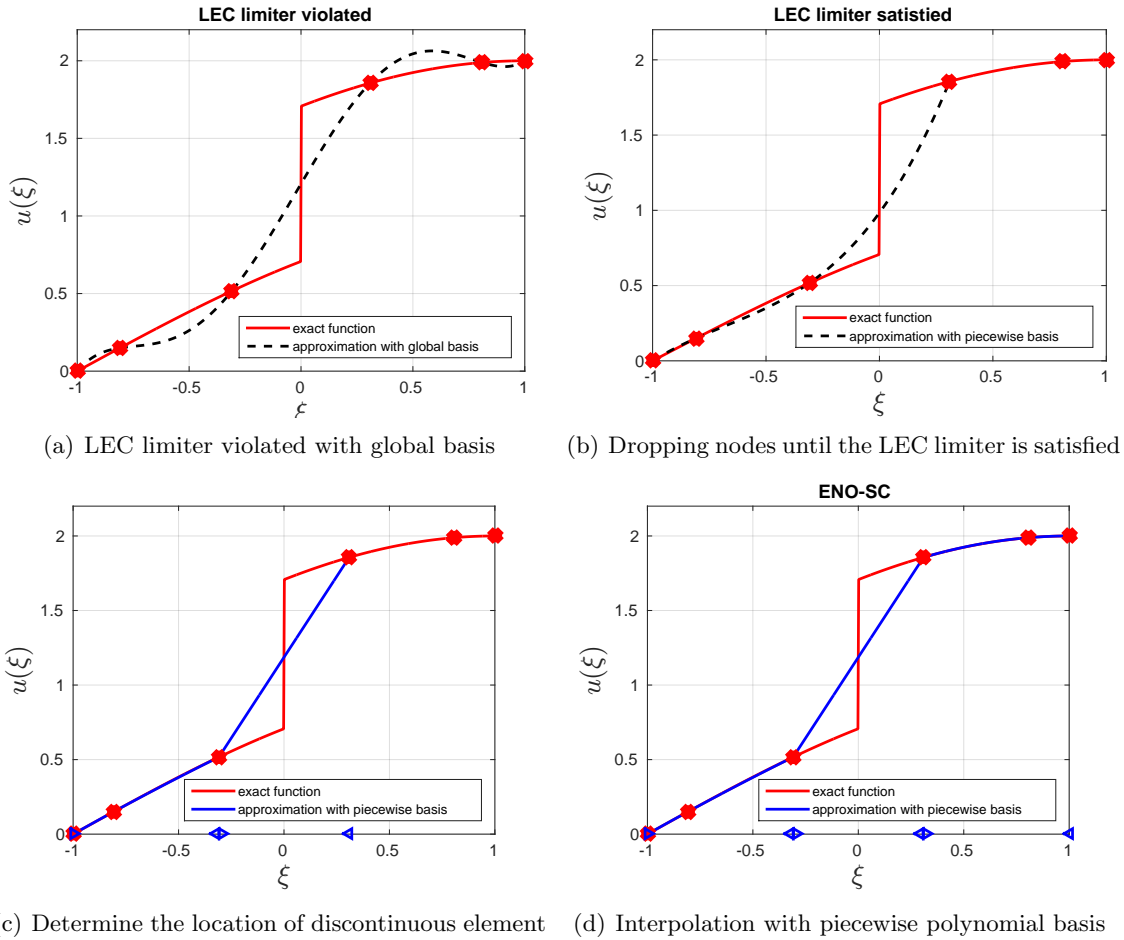
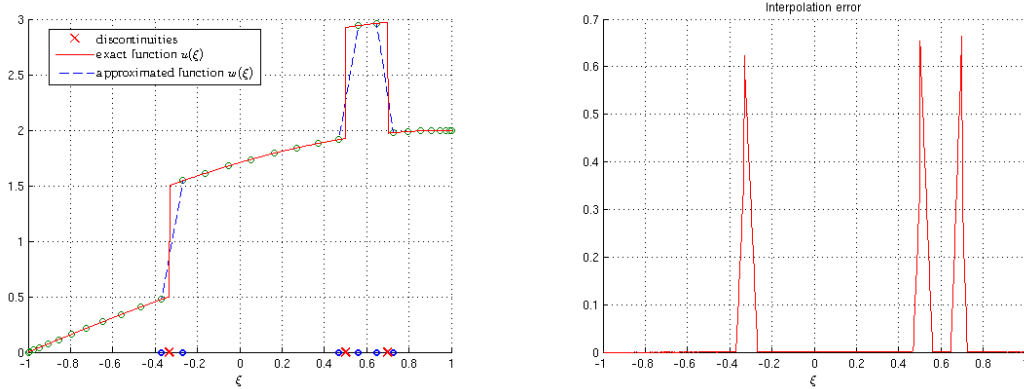


Figure 3.2.1: Discontinuity detection for $u(\xi) = \sin(\frac{\pi}{4}(\xi + 1)) + H(\xi)$ with 6 sampling nodes

To see how this method works, we consider a simple discontinuous function with smooth background $u(\xi) = \sin(\frac{\pi}{4}(\xi + 1)) + H(\xi)$, where $H(x) = \int_{-\infty}^x \delta(s)ds$ is the Heaviside step function. First, we perform interpolation with global basis. The LEC limiter is violated due to the oscillations, as we can see from Figure 3.2.1(a). Then, we drop the nodes used for constructing the basis one by one from the right side until the LEC limiter is satisfied (Figure 3.2.1(b)). For this example, the LEC limiter is satisfied using the first four nodes. Next, we determine on which side the last node lies to the discontinuity by comparing the nearby

The approximated solution constructed using the SC-ENO approach with $s = 30$ is shown in Figure 3.2.2(a), together with the exact solution. It can be seen that the locations of the discontinuities (denoted by red crosses) are well resolved and the local linear interpolations are employed for discontinuous elements (bounded by blue dots) and higher order interpolation in the smooth parts.



(a) Approximation $w(\xi)$ with piecewise polynomial basis

(b) Interpolation error

Figure 3.2.2: Example 3.2.1 approximated with piecewise polynomial basis based on 30 samples

The proposed SC-ENO method can identify the locations of discontinuities with a resolution proportional to the element size. The interpolation error inside the discontinuous elements dominates the whole error of the piecewise approximation. To get an more accurate location of the discontinuity, a natural choice is to insert sampling nodes inside the discontinuous elements until a tolerance value of resolution is reached. Actually, this tolerance value is the final size of the discontinuous element, which is inversely proportional to the number of sampling nodes.

Now, let's consider a 1-dimensional test case, where we can only afford h deterministic solutions under a limited computational budget. The underlying function in the parameter space can be smooth or discontinuous. Suppose those h sampling nodes can be chosen freely in the parameter space. Using the aforementioned robust approximation method, there are two different approaches to use those sampling values to achieve the best accuracy. One choice is to choose $l \leq h$ sampling nodes correspond to a certain level of approximation using the Chebyshev extrema points according to 2.4.3. Then run the deterministic solver with those l uncertain input values. Lastly, the approximation is constructed at one time using the SC-ENO method. Another choice is to use those computational resources step by step rather than one-time. Since the post-processing is much cheaper compared to the deterministic solver, the approximation procedure can start with a low level of approximation. Then, we can choose to add more sampling nodes according to the smoothness of the constructed response surface. If there is no discontinuity detected, the remaining deterministic solutions can be obtained at those sampling nodes belonging to a higher level of approximation.

Then, the SC-ENO method is applied to all of the sampling nodes. This would yield the same approximation result as the first choice. If there exists a discontinuity in the parameter space, the remaining sampling nodes are supposed to be added inside those discontinuous elements to narrow the size of the discontinuous element. It is true that the second choice is able to obtain smaller approximation error in the vicinity of the discontinuity because the linear interpolation become steeper. However, the accuracy away from the discontinuity may not be as good as expected due to the limited number of sampling points, which is equivalent to a low order of polynomial basis.

In this thesis work, the first approach is chosen for the sake of the parallelization of the deterministic solver. Besides, due to the nested nature of the Chebyshev points, at least a finer resolution of the discontinuity can be expected with an increasing level of approximation, even though it may not be optimal for the same number of sampling nodes.

3.3 Subcell Resolution

Admittedly, a robust approximation of the discontinuous function can be achieved by using a linear interpolation across the jump discontinuity. However, the response surface in the elements containing the discontinuity remains the same as long as the location of the discontinuity is between the sampling nodes that are used for linear interpolation. In other words, the discontinuity does not affect the stochastic response surface unless it moves across a sampling point. At that moment, the response surface changes discontinuously. If the discontinuity in the parameter space is caused by a discontinuity in the physical space, this linear interpolation would result in a staircase approximation of the integral value of the solution in the physical space, *e.g.* the mean and standard deviation. To get rid of it, we need a subcell resolution to achieve more accurate approximations of discontinuities in the parameter space.

The notion of subcell resolution (SR) was developed by Harten [32] in the Finite Volume Method (FVM) to obtain accurate approximations of discontinuities in the physical space. Reformulation of SR concept into the Stochastic Collocation methods was introduced in [75]. Its basic strategy is to extract the discontinuity location \mathbf{x}_{disc} in the physical space from each of the deterministic simulations for the sampled random parameter values $\boldsymbol{\xi}_k$. Then, the physical discontinuities \mathbf{x}_{disc} are interpolated in the parameter dimensions to derive a relation for the location of the physical discontinuities \mathbf{x}_{disc} as a function of the random parameters $\boldsymbol{\xi}$. In most real cases, this function $\mathbf{x}_{disc} = f(\boldsymbol{\xi})$ is smooth and monotonic in the parameter space. Then, for each physical location, the predicted locations of discontinuity are obtained in the form of a hyperplane in the stochastic space. With the subcell resolution, the interpolation from the smooth elements can be extended to the predicted discontinuity locations in the discontinuous elements, replacing the local linear interpolation by a higher order interpolation.

Remark 3.3.1 (Limitation of the Subcell Resolution). It should be noted that the extraction of the physical discontinuity is problem-dependent. In some cases, the spatial jump is not strong enough, *e.g.*, a shock wave weakened by the viscous boundary layer. As a result, the locations of physical discontinuities \mathbf{x}_{disc} are hard to parameterize and then interpolate as a

function of the random parameters ξ .

3.4 Discussion of discontinuity detection methods

In this thesis work, besides the SC-ENO method and the SR approach, edge detection technique based on the polynomial annihilation method was once considered as a candidate approach to address the Gibbs oscillations in the parameter space. In literature, an efficient approach, which is based on the polynomial annihilation and active learning, was proposed to localize the discontinuities in complex simulations last year [28]. Although improvements in terms of the number of deterministic sampling nodes were achieved, this approach was not adopted due to the following reasons. First of all, only a sufficiently large number of sampling points can guarantee a quality result. Otherwise, the approximated locations of discontinuity may be far away from the true discontinuity. Secondly, the distribution of the sampling nodes may not be optimal in terms of the accuracy of the constructed surrogate model. The active learning process starts with an *initialization phase* [28], during which the sampling points are assigned to different regions and the polynomial annihilation is used to perform a first “guess” of the discontinuity location. After that, adaptive refinement is performed around the guessed location. As a result, sampling points are clustered in a narrow band. It is likely that the approximation away from the discontinuity loses the accuracy.

For both the polynomial annihilation method and the SC-ENO method, the inputs are the sampling nodes obtained from deterministic simulations. Compared to the expensive costs of deterministic simulations, the computational cost of both methods can be seen negligible. Hence, they can be viewed as *post-processing* procedure. From the author’s experience, both of them suffer from low resolution and noisy environment. Low resolution, which is due to the limited number of sampling nodes, may result in an inaccurate location of the discontinuity for the polynomial annihilation method and a misidentification of a steep gradient as a discontinuity for the SC-ENO method. The key difference between the two methods is as follows: for the polynomial annihilation method, we need a threshold value for the jump function and we can get an approximated location of the discontinuities; while for the SC-ENO method, no threshold value is needed and we can get an approximated interval in which the discontinuity lies.

In practice, the underlying function may be discontinuous in its derivatives rather than function values. Besides that, there may exist strong gradient in the response surface. All of these are likely to result in oscillating response surface. Under this condition, the aforementioned discontinuity detection method, such as the SR approach and the polynomial annihilation technique still works. However, there is a risk that the constructed response surface that is supposed to be continuous becomes a discontinuous one. For such continuous non-differentiable underlying function, the proposed SC-ENO remains a reliable robust approximation method because it is based on the limiter suppressing oscillations. An example is given in the following.

Example 3.4.1 (1-D continuous non-differentiable function). *Consider a continuous non*

differentiable function $u(\xi)$ with a steep gradient between $[0.1 - 0.35]$.

$$u(\xi) = \begin{cases} \xi^2, & \xi < 0.1 \\ 3.96\xi - 0.386, & 0.1 \leq \xi \leq 0.35 \\ \cos(\xi - 0.35) & \xi > 0.35 \end{cases} \quad (3.4.1)$$

As we can see from Figure 3.4.1(a), although the underlying function is continuous, overshoots still exist around the steep gradient region if the spectral basis is used. For this test case, the SC-ENO resolves the sharp region quite well, where a linear interpolation is applied.

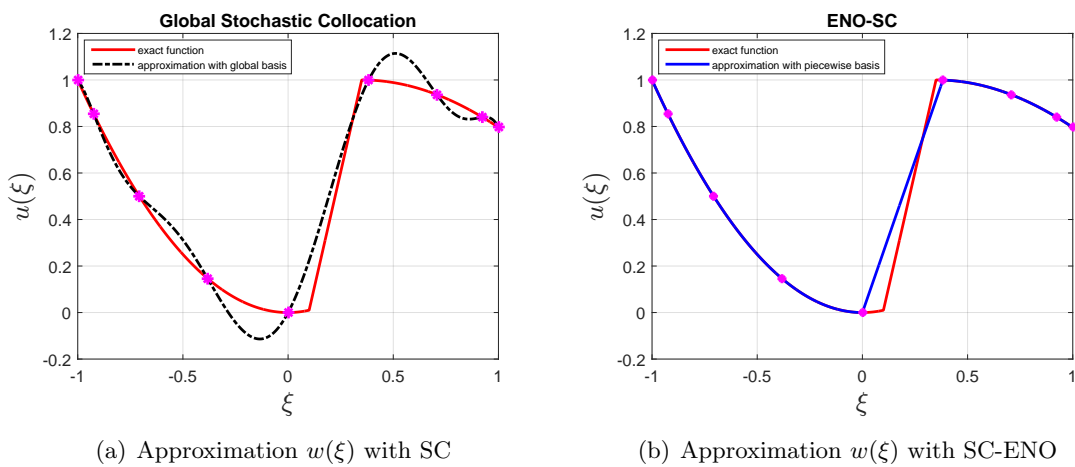


Figure 3.4.1: Example 3.4.1 approximated with the global SC and SC-ENO method based on 9 samples

More 1-dimensional numerical examples are presented in chapter 5. Before that, the multi-dimensional formulation of the SC-ENO method is given in the following chapter.

Chapter 4

Multi-dimensional Stochastic Collocation with ENO robustness

In this chapter, the multi-dimensional formulation of the proposed SC-ENO method is presented. Firstly, a new method for the discontinuity localization in multi-dimensional space is introduced in Section 4.1. Then, a matching algorithm used for the domain classification is described in Section 4.2. After that, several multivariate interpolation methods used for the surrogate construction are discussed in Section 4.3. Finally, the combination of the SC-ENO method with the dimension adaptive sparse grid approach [26] is discussed.

4.1 Discontinuities detection in the multi-dimensional space

The proposed one-dimensional ENO based discontinuity detection method can be extended to the multi-dimensional space by a dimension by dimension approach. Following the same procedure for the 1-D case, we first run the deterministic simulations at the prescribed structured sampling nodes that are formed by the tensor product of the 1-D quadrature nodes. Suppose the number of sample nodes for each dimension is s_{i_k} ($k = 1, \dots, N$), then the entire parameter space is decomposed into $n_e = \prod_{k=1}^N (s_{i_k} - 1)$ hypercube elements, *i.e.* $\Xi = \bigcup_{J=1}^{n_e} \Xi_J$. Every N -dimensional hypercube element contains $2N$ hypercubes of $(N - 1)$ -dimension on the boundaries. For example, a 2-dimensional square has 4 sides or lines; a 3-dimensional cube has 6 2-dimensional faces; a 4-dimensional tesseract has 8 cubes. Without loss of generality, an N -dimensional hypercube element is identified as the discontinuous element if any of its boundary hypercubes of $(N - 1)$ -dimension contains discontinuity. If we repeat this detecting process starting from the highest dimension, the problem amounts to detecting all the 1-dimensional line segments with discontinuities embedded in the N -dimensional hypercube. Therefore, an N -dimensional hypercube element is identified as a discontinuous element if it contains a discontinuous line on the boundary. In practical implementations, the tracking of discontinuous line elements $\Xi_{disc_i}^k$, with $disc_i^k \in \{1, \dots, s_{i_k} - 1\}$ and $k \in \{1, \dots, N\}$ can be achieved by performing the 1-D detection Algorithm (1) for

each dimension ξ_k . During this process, all but the k -th dimension are fixed by a given coordinate.

Example 4.1.1 (Multi-dimensional discontinuities detection). *To illustrate the proposed discontinuities detection method, we consider the following function [37]:*

$$u(\boldsymbol{\xi}) = \begin{cases} 1, & \sum_{i=1}^k \xi_i^2 < r^2, \quad k \leq N \\ 0 & \text{otherwise} \end{cases} \quad (4.1.1)$$

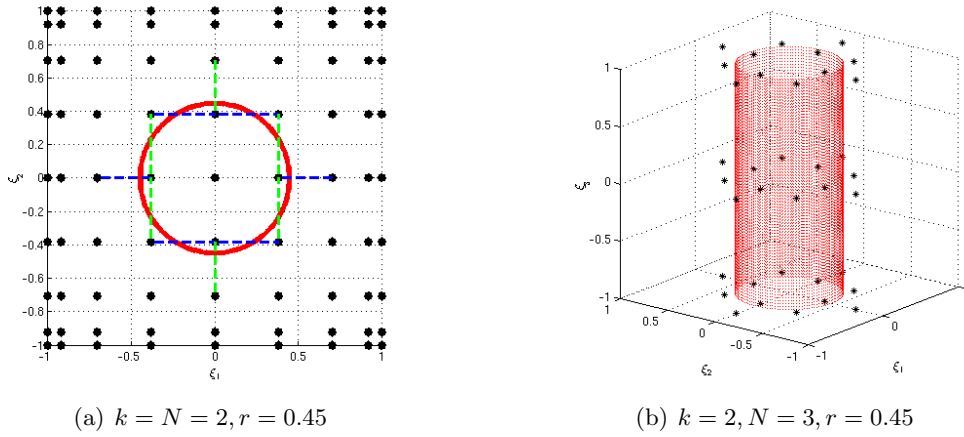


Figure 4.1.1: Discontinuity detection method applied to Example 4.1.1

Generally, the discontinuities are associated with all the random variables, *i.e.* $k = N$, then the whole parameter space is decomposed in all dimensions. Fig. 4.1.1(a) shows a discontinuous curve on a two dimensional domain. In this case, the 1-D detection Algorithm (1) is applied to each dimension (ξ_1, ξ_2). Here, the sample nodes are the tensor product Clenshaw-Curtis points with the level of interpolation $i_1 = i_2 = 4$. As we can see from Fig. 4.1.1(a), the discontinuous line elements, which are indicated by blue dashed lines, are spotted when the first dimension ξ_1 is scanned. Similarly, green dashed lines show the discontinuous elements along the second dimension ξ_2 . Then, all the elements of rectangular shape with dashed lines are flagged as discontinuous elements. However, if the discontinuities lie in the lower-dimensional space, the global spectral expansion will be maintained in the dimensions without discontinuities. Consider the Example 4.1.1 with $k = 2, N = 3$, the discontinuity manifold is the surface of a cylinder. There does not exist a jump discontinuity in the ξ_3 dimension. As a result, the desired accuracy can be achieved with a lower level of interpolation i_3 compared to the other dimensions. Here, we choose $i_1 = i_2 = 4, i_3 = 2$. Fig. 4.1.1(b) shows the result of the discontinuity detection method. The discontinuity surface is represented by the dense red dots. Black dots stand for the end points of discontinuous line elements. If we cut the cylinder horizontally (by fixing the ξ_3 coordinate), the same result will show up as Fig. 4.1.1(a).

4.2 Domain classification

Once the discontinuities enclosed by discontinuous elements are resolved, the whole parameter space is partitioned into disjoint smooth sub-domains bounded by discontinuities. Due to the arbitrary shape of the discontinuities, the resulting smooth sub-domains would no longer be hypercube-shaped. The next task is to construct accurate polynomial approximations inside each smooth element using the existing simulation results on unstructured sample nodes. First, we need to classify the sampling nodes into each continuous sub-domain. Thanks to the structured nature of tensor product grids, the classification of grids can be achieved by classifying hypercube elements. Then, all the vertices of each hypercube elements in the same category are in the same smooth sub-domains.

Assume that the discontinuous elements are well resolved by the discontinuities detection algorithm. The remaining continuous elements are classified by a tracing algorithm. Initially, all the continuous elements are categorized as unclassified and a random continuous element is picked. Then we examine its neighboring elements in all axial directions. If they are not discontinuous elements, then they all belong to the same class as the original element. This scanning process is repeated for each newly-classified element and continues until it stops yielding new elements. As a result, we can conclude that all the elements belonging to the same class 1 have been totally covered. Now, we pick randomly another unclassified continuous element and start looking for the elements belonging to the class 2. This process goes on until all the continuous elements have been classified. Finally, the domain classification process is complete. The pseudo-code of this domain classification process is outlined in Algorithm 2.

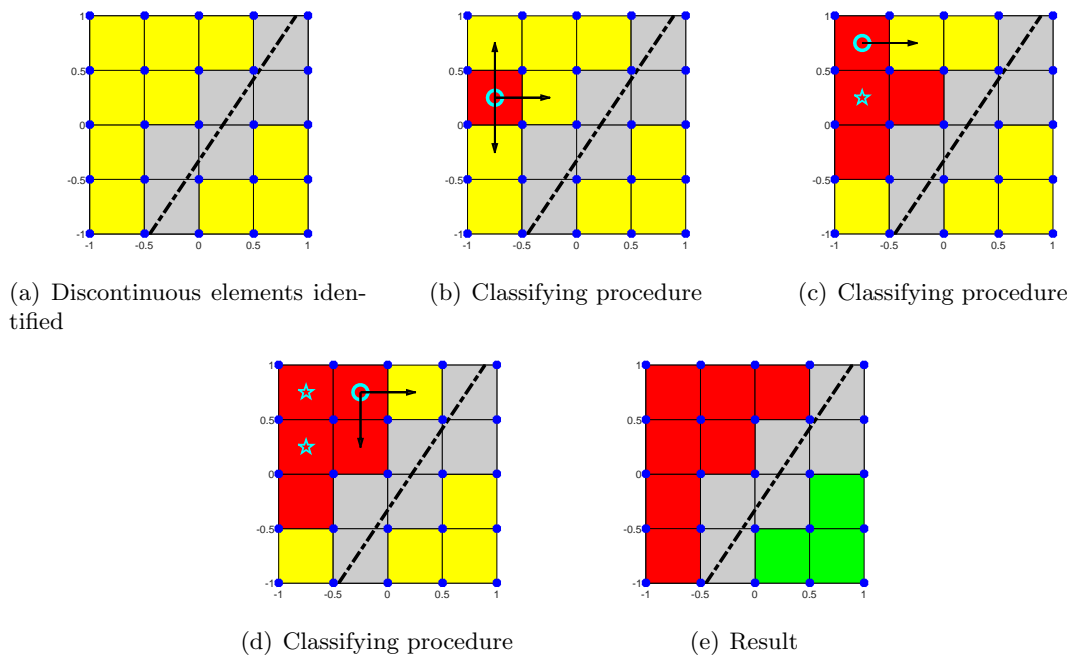


Figure 4.2.1: Domain classification applied to a two-dimensional example

A 2-dimensional example with 5 nodes in each dimension is presented to show how this algorithm works. For the ease of explanation, equiv-distant points are used. Suppose the jump discontinuity is a straight line running across the two dimensional domain, which is denoted by the black dash-dot line in Figure 4.2.1. After the discontinuity detection step, the grey discontinuous element are found and the whole domain is decomposed into two smooth sub-domains. The continuous elements are represented by the yellow squares. Firstly, a random continuous element, which is denoted by the red element with a cyan circle at the center in Figure 4.2.1(b), is picked and classified into 1_{st} sub-domain. Its neighbours in all dimensions are checked to see if they are continuous ones. At the same time, the checked element is flagged with a cyan pentagon in Figure 4.2.1(c). The same checking process continues for each newly-classified element until all the elements lying on one side of the discontinuity are categorized into the same class. Finally, the two smooth sub-domains, which are indicated by red and green colors, are obtained, as shown in Figure 4.2.1(e)

Algorithm 2 N -dimensional domain classification

Input: N -dimensional array I indicating the smoothness of each hypercube element
 $k = 0$
 unc : set of index of smooth elements
while $unc \neq \emptyset$ **do**
 $k = k + 1$
 $class(k) = unc(1)$
 $num = 1$
 $asnum = 0$
 while $asnum \neq num$ **do**
 $index = class(k)(asnum + 1)$
 for $i = 1 : N$ **do**
 Check the two neighbouring elements of element $unc(index)$ in dimension i .
 Classify them as class k if they are continuous elements.
 Store the index in order.
 end for
 $num = \#(class(k))$
 $asnum = asnum + 1$
 end while
 $unc = unc \setminus class(k)$
end while
Output: $class(k)$ indicating the index of elements belonging to class k

4.3 Multivariate interpolation on unstructured grids

After classifying the vertices of each smooth element, the sampling nodes belonging to each class becomes unstructured since each smooth region may not be of hypercube shape. The next step is to construct an approximation response surface for each of the sub-domain. In order to be consistent with the notation convention used in the multivariate interpolation, symbol x is used to denote the unstructured sampling points in the stochastic space in contrast to structured ones ξ . Actually, the remaining problem can be seen as a multivariate

interpolation problem. Although the univariate interpolation is a well-established field, the problem becomes tricky for the multivariate case ¹. To show this, we need a few definitions.

Definition 4.3.1 (Lagrange interpolation problem). *Given a finite point set $\Theta_d = \{x_1, \dots, x_S\}^2$ with elements $x_j = (x(1), \dots, x(d)) \in \mathbb{R}^d$. The values to be interpolated are denoted by y_1, \dots, y_S . The Lagrange interpolation problem is to find a polynomial $p \in F$, such that*

$$p(x_j) = y_j, \quad j = 1, \dots, S, \quad (4.3.1)$$

where F , called the interpolation space, is a subspace of the space of all d -variate polynomials Π^d .

Definition 4.3.2 (Posedness). *The Lagrange interpolation problem in Definition 4.3.1 for the points $\Theta_d = \{x_1, \dots, x_S\}$, is called posed in F if there exists a unique polynomial $p \in F$, such that*

$$p(x_j) = y_j, \quad j = 1, \dots, S.$$

Definition 4.3.3 (Haar space). *Suppose $\Upsilon \subseteq \mathbb{R}^d$. Let $B \subset \mathcal{C}(\Upsilon)$ be a finite dimensional subspace with polynomial basis b_1, \dots, b_S . Then B is a **Haar space** on Υ if the determinant of the Vandermonde matrix formed by any set of points $\Theta_d = \{x_1, \dots, x_S\} \in \Upsilon$ does not vanish, i.e.*

$$\det(b_k(x_j)) \neq 0$$

Remark 4.3.1. The existence of Haar spaces guarantees the posedness of the Lagrange interpolation problem. It has been proved that univariate polynomials of degree $\leq S - 1$ form a S -dimensional Haar space for a set of 1-dimensional data $\{x_1, \dots, x_S\}$. For the multivariate case, there is no guarantee due to the following theorem.

Theorem 4.3.1 (Haar-Mairhuber-Curtis theorem [50, 12]). *Suppose that $\Upsilon \subseteq \mathbb{R}^d$ contains an interior point³. There exists no Haar space on Υ for dimension $d \geq 2$.*

In [21], an interpretation of the Haar-Mairhuber-Curtis theorem is given as follows: *If we want to have a well-posed multivariate scattered data interpolation problem, we can no longer fix in advance the set of basis functions we plan to use, instead **the basis should depend on the data locations**.* Guided by this idea, two types of interpolation methods with basis dependent on the point locations are tested in this thesis. They are introduced in the following sections. After that, their performances are illustrated and compared.

4.3.1 Sauer-Xu multivariate Lagrange interpolation

The multivariate Lagrange interpolation method developed by T.Sauer and Y.Xu [59] is able to find the interpolation space for scattered sampling nodes set Θ_d . Its main idea is to successively construct the Lagrange fundamental polynomial basis L_1, \dots, L_S satisfying the

¹A general survey of all the results before the 21st century is given in [23].

²We use N in the previous sections to denote the stochastic dimension

³ x is an interior point of $\Upsilon \subseteq \mathbb{R}^d$ if there exists an open ball with radius $\delta > 0$ and center at x that is completely contained in Υ .

conditions $L_i(x_j) = \delta_{ij}, i, j = 1, \dots, S$. Then, the interpolant of the function $f(x)$ can be written as:

$$\mathcal{I}(f(x)) = \sum_{j=1}^S f(x_j) L_j(x). \quad (4.3.2)$$

Suppose Π_n^d is a M -dimensional space of polynomials with elements of total degree at most n . Its basis are denoted by $\{q_j\}_{j=1}^M$ and follow a certain graded order. Let $P_j^{[i]}$ denotes the Lagrange polynomial corresponding to the j th point at the i th step. Following an induction process, suppose that $P_1^{[k]}, \dots, P_k^{[k]}$ are already constructed for some $k \geq 1$ from $\{q_j\}_{j=1}^k$ and $\{x_j\}_{j=1}^k$ with the following condition

$$P_i^{[k]}(x_j) = \delta_{ij}, \quad i, j = 1, \dots, k \leq S \quad (4.3.3)$$

satisfied. These basis $P_1^{[k]}, \dots, P_k^{[k]}$ are linearly independent and span a k -dimensional subspace of Π_n^d . Then, for the next point x_{k+1} , we first pick a basis q_{k+1} from the subspace $\Pi_n^d \setminus \{P_j^{[k]}\}_{j=1}^k$ such that $q_{k+1}(x_{k+1}) \neq 0$. Then, $q_{k+1}(x)$ is replaced by

$$q_{k+1}(x) = q_{k+1}(x) - \sum_{i=1}^k q_{k+1}(x_i) P_i(x). \quad (4.3.4)$$

to make $q_{k+1}(x_i) = 0, i \in \{1, \dots, k\}$. After this, the corresponding Lagrange basis for the point x_{k+1} is constructed by:

$$P_{k+1}^{[k+1]}(x) = \frac{q_{k+1}(x)}{q_{k+1}(x_{k+1})}. \quad (4.3.5)$$

With this newly added basis $P_{k+1}^{[k+1]}(x)$, we need to further change the previous basis as follows

$$P_j^{[k+1]}(x) = P_j^{[k]}(x) - P_j^{[k]}(x_{k+1}) P_{k+1}^{[k+1]}(x), \quad j = 1, \dots, k, \quad (4.3.6)$$

to make sure the previous basis vanish at x_{k+1} .

It should be noted that if the Lagrange interpolation problem is posed with respect to Θ_d , there must exist some $j \in \{k+1, \dots, S\}$ such $q_j(x_{k+1}) \neq 0$ at the j th step. Without loss of generality, we assume that $q_{k+1}(x_{k+1}) \neq 0$.

The above algorithm works as long as the points set Θ_d in posed in Π_n^d . Otherwise, we can enlarge the polynomial space by increasing the total order n . From the Kergin interpolation [39], we know that there always exist a subspace $\Pi_p^d \subseteq \Pi_{S-1}^d$ with $p > n$ such that the Lagrange interpolation problem with respect to Θ_d is posed in Π_p^d . This algorithm is easy to implement since only the natural operations on polynomials, *i.e.*, addition, multiplication by scalars and point evaluation, are required. However, from the author's experience, it takes much longer time for high dimensional scattered points. What's more, the numerical stability is an inevitable issue inherent to this method since division $P_k(x) := \frac{Q_i(x)}{Q_i(x_k)}$ exists in the algorithm. In [59], some improvements were recommended, such as the use of Bernstein-Bezier polynomial basis. It is observed that a better stability is accomplished by pivoting strategies when searching for index j such that $q_j(x_{k+1}) \neq 0$. That is, determine j such that q_j has maximal absolute value at x_{k+1} . A pseudo-code for this algorithm is given in Appendix B.

4.3.2 Least interpolation

In this section, another multivariate interpolation method, called *least interpolation* [16], is presented. For the notation convenience, the elements of the finite point set Θ ⁴ are denoted as $\{\theta_1, \dots, \theta_S\}$ with $\theta_j \in \mathbb{R}^d$. This method constructs the right interpolation space Π_Θ with some nice properties, which are listed in Appendix D. First, we show some necessary definitions concerning the interpolant.

Definitions

Multi-index $\alpha = (\alpha(1), \dots, \alpha(d))$, $\alpha(i) \geq 0$, $i = 1, \dots, d$ denotes the order of derivative of a d -dimensional function. We define $D^\alpha := \prod_j D_j^{\alpha(j)}$ as a multivariate differential operator, with D_j being the differentiation with respect to the j th argument. The power series expansion (*i.e.*, the Taylor series expansion around the origin), of a function p analytic at the origin reads as follows:

$$p = \sum_{\alpha} \frac{\theta^\alpha}{\alpha!} D^\alpha p(0), \quad (4.3.7)$$

where $\theta^\alpha = \theta(1)^{\alpha(1)} \dots \theta(d)^{\alpha(d)}$. The **least** operator \downarrow , by definition, gives the **least** term p_\downarrow as the first nontrivial term in the power series expansion of p . If g_\downarrow has degree k , then

$$g_\downarrow = \sum_{|\alpha|=k} \frac{\theta^\alpha}{\alpha!} D^\alpha g(0).$$

When the **least** operator \downarrow is applied to a linear space H of functions analytic at the origin, the following function space is obtained:

$$H_\downarrow := \text{span}\{f_\downarrow : f \in H\}.$$

It was proved in [16] that

$$\dim H_\downarrow = \dim H \quad (4.3.8)$$

The **exponential** e_θ **with frequency** θ has the power series expansion:

$$e_\theta := e^{\theta \cdot x} = 1 + \theta \cdot x + (\theta \cdot x)^2/2 + \dots, \quad (4.3.9)$$

with $\theta \cdot x = \sum_{j=1}^d \theta(j)x(j)$ the ordinary scalar product of two d -vectors θ and x . Because exponentials e_θ with different frequencies θ is linearly independent [17], they form a basis of the function space

$$\text{exp}_\Theta := \text{span}\{e^{\theta \cdot x} : \theta \in \Theta\} \quad (4.3.10)$$

and $\dim \text{exp}_\Theta = \#\Theta$.

This method relies on a *pairing* operation, which is defined as follows:

$$\langle g, f \rangle := \sum_{\alpha} D^\alpha g(0) D^\alpha f(0) / \alpha!, \quad g, f \in \Pi. \quad (4.3.11)$$

⁴The previous subscript d is omitted for simplification.

It follows that the pairing of a function f with respect to the exponential e_θ amounts to the polynomial evaluation $f(\theta)$, *i.e.*,

$$\langle e_\theta, f \rangle = \sum_{\alpha} D^\alpha e_\theta(0) D^\alpha f(0) / \alpha! = f(\theta), \quad (4.3.12)$$

because

$$D^\alpha e_\theta(x) = \prod_j D_j^{\alpha(j)} e_\theta(x) = \prod_j \theta(j)^{\alpha(j)} e^{\theta \cdot x} = \theta^\alpha e^{\theta \cdot x}. \quad (4.3.13)$$

Proposition 4.3.2. [17] *The polynomial interpolant in the form*

$$\mathcal{I}_\Theta f := \sum_{j=1}^S g_{j\downarrow} \frac{\langle g_j, f \rangle}{\langle g_j, g_{j\downarrow} \rangle} \quad (4.3.14)$$

is the unique interpolant satisfying $\mathcal{I}_\Theta f = f$ on Θ , with g_1, g_2, \dots, g_S a basis for \exp_Θ (particularly, $S = \#\Theta$) and

$$\langle g_i, g_{j\downarrow} \rangle = 0 \iff i \neq j. \quad (4.3.15)$$

The proof of this proposition can be found in [17]. As we can see from the proposition, the space spanned by $\{g_{1\downarrow}, \dots, g_{S\downarrow}\}$ is the posed polynomial space for interpolation at Θ . Since $\dim \Pi_\Theta = \dim(\exp_\Theta) = \#\Theta = S$, we have

$$\Pi_\Theta = \text{span}\{g_{1\downarrow}, g_{2\downarrow}, \dots, g_{S\downarrow}\}. \quad (4.3.16)$$

Construction of the basis

We can construct the interpolation space $\Pi_\Theta = \text{span}\{g_{1\downarrow}, g_{2\downarrow}, \dots, g_{S\downarrow} : g \in \exp_\Theta\}$ from the basis $\{e^{\theta \cdot x} : \theta \in \Theta\}$ for \exp_Θ by a variant of the Gram-Schmidt process [15]. In the following, we will denote $e^{\theta_i \cdot x}$ by f_i for ease of explanation. Suppose we already have g_1, g_2, \dots, g_{j-1} available, which span the same space spanned by f_1, f_2, \dots, f_{j-1} , next we achieve the orthogonality:

$$\langle g_{i\downarrow}, g_j \rangle = 0, \quad , i < j, \quad (4.3.17)$$

by computing

$$g_j := f_j - \sum_{i < j} g_i \frac{\langle g_{i\downarrow}, f_j \rangle}{\langle g_{i\downarrow}, g_i \rangle}. \quad (4.3.18)$$

In order to achieve another orthogonality

$$\langle g_{j\downarrow}, g_i \rangle = 0, \quad , i < j, \quad (4.3.19)$$

we make the further modification:

$$g_i \leftarrow g_i - g_j \frac{\langle g_{j\downarrow}, g_i \rangle}{\langle g_{j\downarrow}, g_j \rangle}. \quad (4.3.20)$$

The denominator in the above equation (4.3.20) is non-zero since $g_j \neq 0$, which results from the linear independence of the f_i . It should be noted that the above modification (4.3.20) does not change the biorthogonality in equation (4.3.17) due to the following reasons:

- If $\deg(g_{j\downarrow}) > \deg(g_{i\downarrow})$, $g_{i\downarrow}$ does not change from (4.3.20) because $(g_{j\downarrow}) >$ interacts only with the expansion terms of (g_i) of order k in $\langle g_{j\downarrow}, g_i \rangle$, where $\deg(g_{j\downarrow}) = k$.
- If $\deg(g_{j\downarrow}) < \deg(g_{i\downarrow})$, g_i does not change since $\langle g_{j\downarrow}, g_i \rangle = 0$.
- If $\deg(g_{j\downarrow}) = \deg(g_{i\downarrow})$, $\langle g_{j\downarrow}, g_i \rangle = \langle g_{i\downarrow}, g_j \rangle = 0$, which is already achieved in (4.3.17).

Finally, (4.3.17) and (4.3.19) combines to make (4.3.15), and we obtain the basis $\{g_{1\downarrow}, g_{2\downarrow}, \dots, g_{S\downarrow}\}$ for Π_Θ . In [17, 14, 15], extensive discussions about the connection of this method to Gauss elimination were made. An effective approach for the construction of basis for Π_Θ satisfying (4.3.15) is proposed in [17], which is based on Gauss elimination of the Vandermonde matrix by segments (*i.e.*, by degree-by-degree). An improved version in terms of numerical stability is given in [15], where it is also verified that the earlier Gram-Schmidt like algorithm applied to $f_i := e^{\theta_i \cdot x}$, $i = 1, \dots, S$, is Gauss elimination with *column* pivoting applied to the Vandermonde matrix. In Appendix C, details of Gauss elimination with *row* pivoting are presented, which yields not only the same polynomial space as the column pivoting, but also a ‘good’ ordering of the points in Θ .

4.3.3 Comparison of the multivariate interpolation methods

So far, two multivariate interpolation methods have been introduced. In this section, the performances of them together with the conventional fixed basis method solved by Gauss elimination with row pivoting are investigated with respect two simple examples. Without loss of generality, two dimensional domain is considered. Let (x, y) stands for the 2-D variable.

Example 4.3.1. Let $\Theta = \{(-0.5, -0.5), (0, 0), (0.5, 0.5)\} \subset \mathbb{R}^2$, the values of the function to be interpolated are $f(-0.5, -0.5) = 1$, $f(0, 0) = 3$, $f(0.5, 0.5) = 5$.

For all methods, the polynomial basis needs to be prescribed. As we can see from the numerical example provided below, the ordering of the polynomial basis has an influence on the interpolant. If we use the graded lexicographic ordering of the monomial basis for the Vandermonde matrix V :

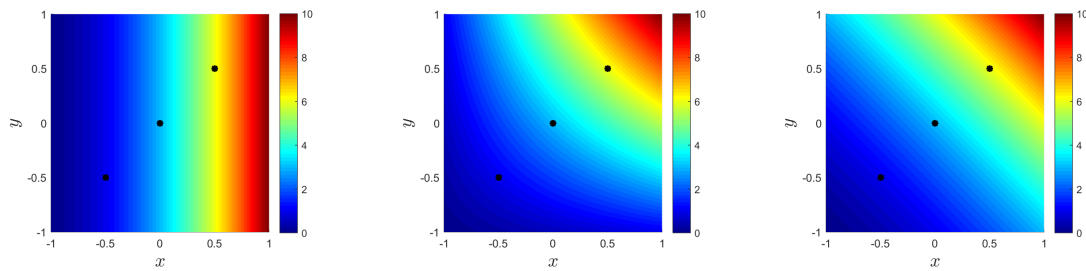
$$(0, 0), (1, 0), (0, 1), (2, 0), (1, 1), (0, 2), \dots,$$

it is easy to verify that $\det(V) = 0$. In other words, the Lagrange problem is not posed for the interpolation space $F = \text{span}\{()^{\alpha_1}, ()^{\alpha_2}, ()^{\alpha_3}\}$ with $\alpha_1 = (0, 0)$, $\alpha_2 = (1, 0)$ and $\alpha_3 = (0, 1)$. However, if we use the Sauer-Xu Lagrange interpolation algorithm, the interpolant $f(x, y) = 2x^2 + 5x + 3$ is obtained. The plot of the results is shown in Figure 4.3.1(a). Suppose we use a different ordering of the monomial basis, *i.e.*, put the interaction term first among the basis with the same total order:

$$(0, 0), (1, 0), (0, 1), (1, 1), (2, 0), (0, 2), \dots,$$

then the interpolant $f(x, y) = 2xy + 2.5x + 2.5y + 3$ is obtained by the Sauer-Xu algorithm, whose plot is shown in Figure 4.3.1(b). This interpolant seems more ‘correct’ since the

gradient of the response surface at all locations is more or less parallel to the straight line connecting the three interpolation points. Now, if we rotate the coordinate system by 45° and define a new variable $s = x + y$, then the original two dimensional interpolation problem is reduced to a one dimensional problem: $f(x, y) = g(s)$ with $g(-1) = 1, g(0) = 3, g(1) = 5$. The univariate interpolant admits a quadratic expansion: $g(s) = 0.5s^2 + 2.5s + 3$. The corresponding 2-D interpolant is $f(x, y) = 0.5x^2 + 0.5y^2 + xy + 2.5x + 2.5y + 3$, which is plotted in Figure 4.3.1(c). Actually, this interpolant is the result obtained from the least interpolation method with the graded lexicographic ordering of the monomial basis. This example demonstrate the one proved property of the least interpolation method, *i.e.*, **coordinate system independence** [16]. The full property descriptions can be found in Appendix D. Although only three function values are known, five polynomial expansion coefficients can be determined uniquely.



(a) Interpolant $f(x, y) = 2x^2 + 5x + 3$ obtained by the Sauer-Xu method
 (b) Interpolant $f(x, y) = 2xy + 2.5x + 2.5y + 3$ obtained by the Sauer-Xu method with re-ordered monomial basis
 (c) Interpolant $f(x, y) = 0.5x^2 + 0.5y^2 + xy + 2.5x + 2.5y + 3$ obtained with the least interpolation method

Figure 4.3.1: Comparison of the interpolation for Example 4.3.1

It should be noted that all the above three interpolants are of the same highest total order. Also, they are correct in the sense that they all interpolate the values exactly at those three points (depicted by black dots) exactly. However, the last interpolation makes more sense since the value changes linearly in the direction of the three points while stays constant in the orthogonal direction. From this example, we can observe that the Sauer-Xu algorithm still works when the conventional fixed basis method fails and the ordering of the polynomial basis exerts a big influence on the interpolant. However, although it is numerically stable, there is a risk that the constructed interpolant becomes ‘illogical’ away from the interpolation points. To show this, we consider the following example:

Example 4.3.2. Let $\Theta = \{(-1, -1), (-1, 1), (0, -1), (0, 1), (1, -1), (1, 1)\} \subset \mathbb{R}^2$, the functions values are $f(-1, -1) = 3, f(-1, 1) = 4, f(0, -1) = 5, f(0, 1) = 6, f(1, -1) = 7, f(1, 1) = 8$.

This example is a common case when the proposed SC-ENO method is applied to a discontinuous function. These 6 nodes may constitute a smooth sub-domains with two smooth elements. The interpolant obtained by least interpolation method is $f(x, y) = 2x + 0.5y + 5.5$, as shown in Figure 4.3.2(a). By contrast, the interpolant obtained by the Sauer-Xu algorithm with a monomial basis is $f(x, y) = 2x^3 + 0.5y^3 + 5.5y^2$. If the Legendre polynomial basis is employed, then the interpolant becomes $f(x, y) = 5x^3 + 1.25y^3 + 8.25y^2 - 3x - 0.75y - 2.75$. As we can see from the Figure 4.3.2, even if the values are interpolated exactly at those six

points, the interpolants obtained from the Sauer-Xu algorithm appear to lose the underlying structure of the function and is too complicated away from the interpolation points. This example demonstrate another desired property of the least interpolation method, *i.e.*, **the constructed interpolant has the minimal possible degree.**

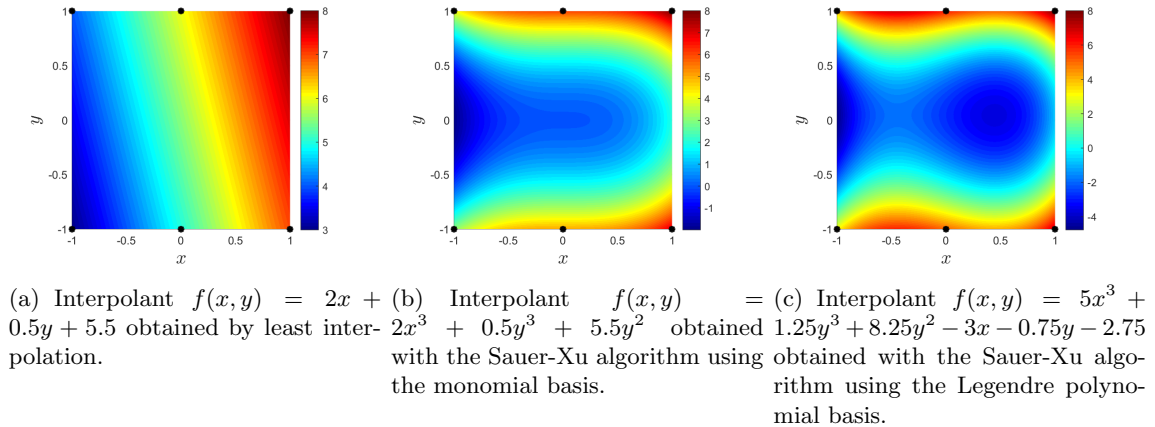


Figure 4.3.2: Comparison of the interpolation for Example 4.3.2.

From the above two examples, we can see that the Sauer-Xu multivariate Lagrange interpolation algorithm is better than the fixed basis method, but it lacks robustness. It seems that the *least interpolation method* is an accurate and stable multivariate interpolation method for scattered data points, which is able to exploit the underlying structure of the interpolation points when necessary. From the author's experience of test, it would produce the most accurate surrogate based on the sampling nodes obtained from the domain classification. However, in some rare cases, *e.g.*, if the underlying function is highly oscillatory in each smooth sub-domains and the locations of sampling nodes Θ are very irregular (partially due to the shape of the discontinuities), this method may result in a model response with some singularities. As a consequence, robustness cannot be maintained. An example is shown as follows.

Suppose the smooth region resulting from the discontinuity detection is shown in Figure 4.3.3(a). There are 51 sampling points in this smooth region, which are the subset of the tensor product Clenshaw-Curtis points and denoted by the black dots. The underlying smooth function $f(x, y) = \cos(3(x + y))$ is highly oscillatory. The interpolant obtained by the least interpolation method is shown in Figure 4.3.3(b). In this example, the distribution of the sampling nodes are far apart. What's more, the number of sampling points is so large that the interpolation space has to be of maximum order of 10 to be posed. As a consequence, the interpolant exhibits abnormal values away from the sampling points. This phenomenon would become worse for high-dimensional case [53]. To remedy this, we propose a more robust interpolation method that matches the proposed discontinuity detection method.

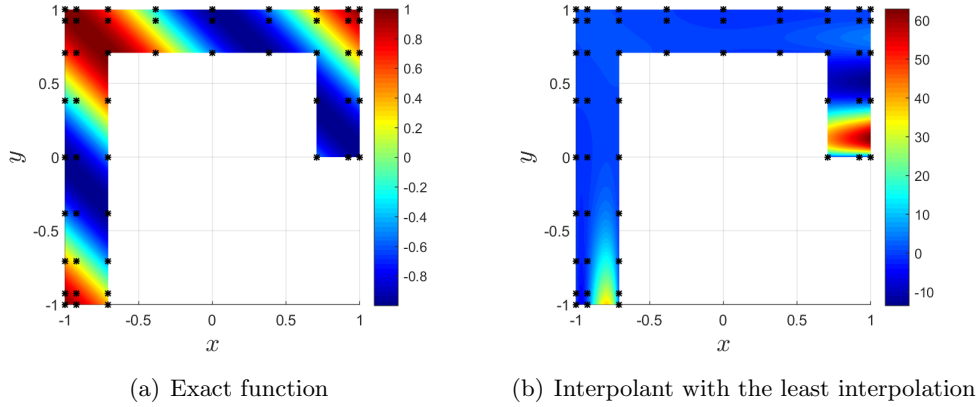


Figure 4.3.3: Unstable behaviour of the least interpolation.

4.3.4 Element-wise interpolation

We recall that the sampling points in the whole stochastic space are formed by the tensor product. In the discontinuities detection step, the continuous elements Ξ_J , with $J \in \{1, \dots, n_e\} \setminus \{disc_1, \dots, disc_n\}$ ⁵, are found by enforcing the modified LEC limiter dimension by dimension. To avoid the occurrence of singularities in the surrogate constructed in smooth sub-domains, a natural choice is to decrease the number of points used for the construction of the polynomial basis. At a cost of reducing the order of the basis, the robustness is strengthened. One possible choice is to construct the interpolant element-wisely by finding the interpolation stencil with fewer points for each smooth element.

Here, we propose to utilize stencil formed by structured subset of the unstructured grids in each smooth sub-domain. To that end, we start by defining the admissible interpolation stencil S_J for element Ξ_J as the one with structured nodes from the smooth sub-domains as well as containing all the vertices of element Ξ_J , thus $S_J = \{\xi_{k_{J,1}}, \dots, \xi_{k_{J,2N}}, \dots\}$. Therefore, the piecewise linear interpolation is assured and a higher degree interpolation can be constructed by adding more neighbouring sampling nodes ξ_k . Generally, the admissible candidate stencils for each smooth element are not unique and they formed a set $\{S_{J,i}\}_{i=1}^{r_J}$ with $r_J \geq 1$. Therefore, a criteria need to be chosen in order to determine which stencil should be picked. For the sake of the best utility of sample results and the high accuracy, we choose the stencil $S_J \in \{S_{J,i}\}$ for Ξ_J with the largest number of sample nodes:

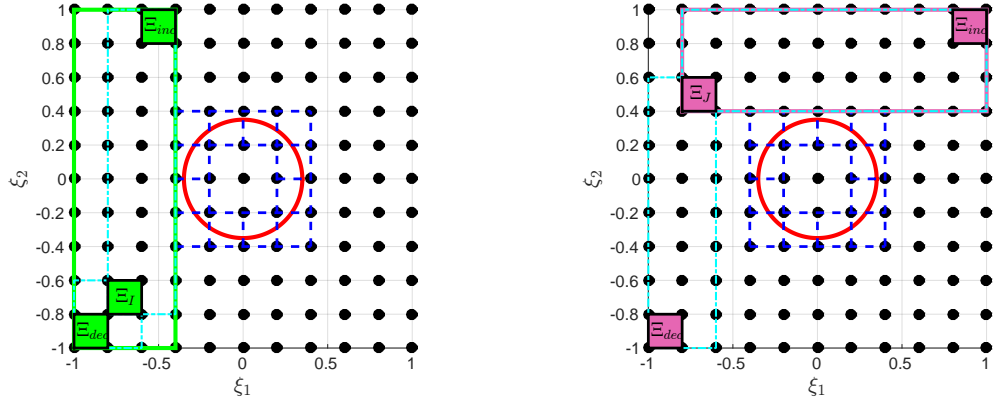
$$S_J = S_{J,i}, \quad \text{with } i = \underset{i \in \{1, \dots, r_J\}}{\operatorname{argmax}} \operatorname{card}(S_{J,i}). \quad (4.3.21)$$

Because the stencil S_J is constructed by the tensor product of grids in each dimension, the problem can be reformulated as follows:

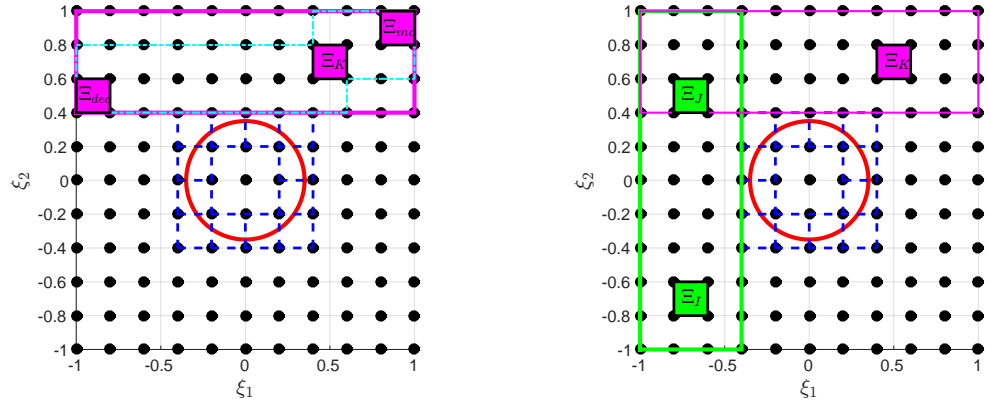
$$S_J = S_{J,i}, \quad \text{with } i = \underset{i \in \{1, \dots, r_J\}}{\operatorname{argmax}} \prod_{j=1}^N (\xi_{end}^{i,j} - \xi_{start}^{i,j} + 1), \quad (4.3.22)$$

⁵ $\{disc_1, \dots, disc_n\}$ is index set of all the discontinuous elements.

where $\xi_{end}^{i,j}, \xi_{start}^{i,j} \in \{\xi_1^{i,j}, \dots, \xi_{s_{ij}}^{i,j}\}$ are the starting and end indices of samples ξ_k^i belonging to the i -th candidate stencil in the j -th dimension. If multiple stencils have the same number of sample nodes, then the one with the minimum average Euclidean distance of the sampling points ξ_k to the center of Ξ_J is chosen.



(a) Stencil for element Ξ_I after diagonal expansion (b) Stencil for element Ξ_J after diagonal expansion



(c) Stencil for element Ξ_K after diagonal expansion (d) final stencil for element Ξ_I, Ξ_J, Ξ_K after updating process (second step)

Figure 4.3.4: Stencil selection algorithm applied to Example 4.1.1, with $k = N = 2$.

Constructing and checking all candidate stencils S_J for all elements Ξ_J is impractical due to the increased complexity for high-dimensional problems. Here, an efficient construction of the interpolation stencil for all smooth elements Ξ_J is proposed, which comprises of the following two steps. Firstly, a temporary neighbour stencil \hat{S}_J is constructed for each Ξ_J by expanding the stencil along the N -dimensional diagonal centering on the hypercube Ξ_J until it touches the discontinuous element Ξ_{disc_i} or the boundaries. In other words, based on all the vertices of element Ξ_J , $\{\xi_{k,J,1}, \dots, \xi_{k,J,2N}\}$, the indices of boundary samples in each dimension are either increased or decreased in at least one dimension. During this process, the temporary neighbour stencil is updated to contain as many sample nodes as possible. Subsequently, two temporary stencils are obtained by expanding in two diagonal directions. Each one of these two stencils is composed of all the sample nodes enclosed in a larger hypercube that contains Ξ_J as one of its corner. The other two corner hypercubes opposite to Ξ_J obtained by increasing and decreasing along diagonal are denoted as Ξ_{inc} and Ξ_{dec} .

Then, we assume that the interpolation stencil is further expanded by using Ξ_{inc} and Ξ_{dec} as the starting and ending element in the diagonal line of the expanded stencil. It should be noted that there may be discontinuous elements in this expanded stencil. If so, one of the previous temporary neighbor stencil with a larger cardinality is chosen. If there is no continuous element around Ξ_J , then $\hat{S}_J = \{\xi_{k_{J,1}}, \dots, \xi_{k_{J,2^N}}\}$. Next, an updating process is run for each \hat{S}_J since there may exist another larger stencil \hat{S}_I that contains all the samples of \hat{S}_J . Meanwhile, the requirement of minimum average Euclidean distance is checked if candidate stencils have the same number of samples. Consequently, the final interpolation stencil for element Ξ_J will be the one with the largest number of sample nodes and the minimum average distance.

Due to the inherent property of the hypercube tessellation, the two-step stencil selection algorithm provides an interpolation stencil with the largest number of sample nodes by restricting the stencil selection to a subset of all possible stencils. In Fig. 4.3.4, we demonstrate our algorithm on a two-dimensional parameter space with two smooth sub-domains as in Example 4.1.1. Equiv-distant sample nodes are used for ease of explanation. Discontinuous elements are denoted by closed dashed blue lines. Stencils for elements are sets of samples enclosed by lines with corresponding color. Cyan dashed-dots lines indicate the process of diagonal expansion. Original interpolation stencil for element Ξ_I is maintained. Interpolation stencils for element Ξ_J and Ξ_K are replaced by a larger stencil with the minimum average distance during the second step.

After the stencil selection step, the surrogate for each element Ξ_J can be constructed with its own stencil S_J . To increase efficiency, an extra step is taken to remove the overlap of interpolation stencils, which is extremely important for high-dimensional problems. Consequently, a smallest set of stencils with the property that all elements are covered just once is obtained. Then, the interpolation space is constructed by the tensor product space

$$P_{\mathbf{s}} = \text{span}\{\xi^\alpha : \alpha < \mathbf{s}\} \quad (4.3.23)$$

where vector $\mathbf{s} \in \mathbb{R}^N$ denote the number of sampling nodes in each dimension for certain interpolation stencil. Although we can construct artificially non-tensor-product polynomial spaces on purpose, it is stated in [58] that *it is reasonable to use tensor product space when interpolating on a tensor product grid*. It is consistent with the fact that a tensor product space is always obtained when the least interpolation method is used to interpolate on tensor product grids, as shown in Appendix D.

In this thesis work, the least interpolation method and the proposed element-wise interpolation method are used for the surrogate construction in the smooth regions. Their performances with respect to some discontinuous test functions are discussed with more details in the next chapter. So far, the formulation of the SC-ENO is based on tensor product grids. In the following, its combination with the sparse grid is presented.

4.4 SC-ENO with the dimension adaptive sparse grid

The proposed SC-ENO method is a post-processing step based on the deterministic values at tensor product sampling grids. To make it more efficient for high-dimensional problem, we propose to combine the SC-ENO method with the sparse grid approach [31, 7]. As we show in Section 2.4.2, the sparse grid be formulated as a linear combination of tensor product grids. The reduction of the number of sampling points is achieved by the manipulation of the multi-indices \mathbf{i} , which controls the number of sampling points in each dimension. For the isotropic sparse grid case, \mathbf{i} belongs to a *hyperbolic index set*:

$$\mathbb{I}_{iso} := \{\mathbf{i} \in \mathbb{N}_+^N, \mathbf{i} \leq N + w\}, \quad (4.4.1)$$

where $w \geq 0$ is the approximation level. In effect, the high order interaction terms are ruled out. The interpolant, denoted by $\mathcal{A}_{w,N}$, is as follows:

$$\mathcal{A}_{w,N} = \sum_{\mathbf{i} \in \mathbb{I}_{iso}} (\Delta^{i_1} \otimes \cdots \otimes \Delta^{i_N}). \quad (4.4.2)$$

where $\Delta^i = I^i - I^{i-1}$ for $i \geq 1$ and $I^0 = 0$. If we expand the above formula and substitute every Δ^i by $I^i - I^{i-1}$, then $\mathcal{A}_{w,N}$ becomes a linear combination of $I^{i_1} \otimes \cdots \otimes I^{i_N}$ with $\mathbf{i} = (i_1, \dots, i_N) \in \mathbb{N}^N$ and $\mathbf{i} \in \mathbb{I}_{iso}$. Because each $I^{i_1} \otimes \cdots \otimes I^{i_N}$ works a tensor product grid, then the SC-ENO approach can be applied to it.

However, the isotropic sparse grid does not take into account the sensitivity of the output with respect to the different uncertain parameters. An equal importance is still assigned to low-order interaction terms between different dimensions. In most applications, the different dimensions are not equally important. In other words, an seemingly high-dimensional problem possess a low effective dimension. In that case, more sampling/interpolation nodes are supposed to be given to those important dimensions.

To this end, many approaches were developed to detect the important correlations and interactions between dimensions, *e.g.*, ANOVA-type (Analysis of Variance) decomposition. Around ten years ago, the dimensional adaptive sparse grid method based on posteriori error indicator was developed for the multivariate integration problem [26], which is regarded as a generalization of the conventional isotropic sparse grid. The index set \mathbb{I} is gradually expanded based on the error indicators (to be addressed below). In this thesis project, this adaptivity concept is incorporated into the proposed SC-ENO method. For completeness, this method is summarized in the following as described in [26]. First of all, a few definitions are listed.

Definition 4.4.1 (Admissible index set). *An index set \mathbb{I} of multi-indices \mathbf{i} , is called admissible if for all $\mathbf{k} \in \mathbb{I}$, the following condition is satisfied,*

$$\mathbf{k} - \mathbf{e}_j \in \mathbb{I} \quad \text{for } 1 \leq j \leq N, k_j > 1, \quad (4.4.3)$$

where \mathbf{e}_j is the j -th unit vector. In other words, for every index $\mathbf{k} \in \mathbb{I}$, the admissible index set contains all indices that have smaller entries than \mathbf{k} in at least one dimension.

Definition 4.4.2 (Forward neighbour index). *The forward neighbour index of an index \mathbf{k} is defined as the N indices $\{\mathbf{k} + \mathbf{e}_j, 1 \leq j \leq N\}$.*

Definition 4.4.3 (Backward neighbour index). *The backward neighbour index of an index \mathbf{k} is defined as the N indices $\{\mathbf{k} - \mathbf{e}_j, 1 \leq j \leq N\}$.*

Definition 4.4.4 (Active index set). *The active index set \mathbb{A} contains those indices of \mathbb{I} whose error indicators have been computed but the error indicators of all their forward neighbours have not been calculated yet.*

Definition 4.4.5 (Old index set). *The old index set \mathbb{O} contains all the other indices of the index set \mathbb{I} . In other words, the active index set \mathbb{A} contains the forward neighbours of the old index set \mathbb{O} .*

4.4.1 Error estimate

The error indicator of a multi-index \mathbf{k} plays an important role in indicating the necessity of future refinement in its forward neighbours. It can depend either on the integral value or on the point value. For example, we can define an error indicator $g(\mathbf{k})$ that depends on the expectation of difference formulas:

$$g_{\mathbb{E}}^{\mathbf{k}} = |\mathbb{E}[\Delta^{\mathbf{k}}]| = |\mathbb{E}[\Delta^{k_1} \otimes \dots \otimes \Delta^{k_N}]|. \quad (4.4.4)$$

Also, we can incorporate *hierarchical surpluses* into the error indicator:

$$g_{hs}^{\mathbf{k}} = \frac{1}{n(\mathbf{k})} \sum_{\mathbf{j}} |w_{\mathbf{j}}^{\mathbf{k}}|, \quad (4.4.5)$$

where $w_{\mathbf{j}}^{\mathbf{k}}$ are the *hierarchical surpluses* of the sub-grid $\Theta_{\Delta}^{\mathbf{k}} = \Theta_{\Delta}^{k_1} \times \dots \times \Theta_{\Delta}^{k_N}$ and $n(\mathbf{k}) = \#\Theta^{\mathbf{k}}$. Suppose the given sampling nodes are nested, *i.e.*, $\Theta^{k-1} \in \Theta^k$, then $\Theta_{\Delta}^k = \Theta^k \setminus \Theta^{k-1}$. The multi-index \mathbf{j} runs over all the points in the sub-grid $\Theta_{\Delta}^{\mathbf{k}}$.

For problems where the function evaluations at sampling nodes are expensive, we can take the number of involved work into account:

$$g_{\#}^{\mathbf{k}} = s_{k_1} \cdots s_{k_N}, \quad (4.4.6)$$

where s_k is the number of nodes in certain dimension given by equation (2.4.3).

Besides, we can take a weighted combination of these error indicators. The weights, which are problem dependent, indicate the relative importance of different error indicators. As for the stopping criteria, we define a global error estimator, which is the sum of all $g^{\mathbf{k}}$ in the active index set \mathbb{A} ,

$$\eta := \sum_{\mathbf{k} \in \mathbb{A}} g^{\mathbf{k}}. \quad (4.4.7)$$

4.4.2 Adaptive procedure

The dimensional adaptive sparse grid interpolant

$$\mathcal{A}_{\mathbb{I}} = \sum_{\mathbf{i} \in \mathbb{I}} (\Delta^{i_1} \otimes \cdots \otimes \Delta^{i_N}). \quad (4.4.8)$$

is constructed by performing the following the procedures:

1. Starts with unit index set $\mathbf{1} = (1, \dots, 1)$. $\mathcal{A} = \{\mathbf{1}\}$ and $\mathcal{O} = \emptyset$.
2. Select the index with the largest error indicator from the active index set and put it into the old index set.
3. Subtract its error indicator from the global error estimator.
4. Add the new admissible forward neighbours of this index and compute their error indicators.
5. Update the solution through equation (4.4.8) using all the function evaluations.
6. End this cycle process if the global error estimate falls below a given threshold value or the work count $\#\Theta_N$ exceeds a given amount. Return the solution given by equation (4.4.8).

4.4.3 Loss of the hierarchical structure

The existing applications of the sparse grid approach to uncertainty quantification use either spectral basis or piecewise multi-linear basis [41, 54, 40]. With the aid of nested 1-D grid, it is possible to construct the conventional sparse grid interpolation based on the hierarchical structure instead of the linear combinations of interpolants on tensor product grids [41]. It is shown that the hierarchical construction is more efficient [42] since it enables the parallelization of the post-processing step and new runs of deterministic solvers at refined grids. What's more, the hierarchical structure make it possible to obtain a error indicator of the current level of approximation. However, this more efficient construction structure is not applicable to the SC-ENO approach. The reasons are given as follows.

Suppose the nested Clenshaw-Curtis nodes Θ^i is used, the 1-dimensional interpolation formula of level i is given by

$$I^i(u) = \sum_{\xi^i \in \Theta^i} L_{\xi^i} \cdot u(\xi^i), \quad (4.4.9)$$

where, L_{ξ^i} are basis functions satisfying $a_{\xi^i}(\xi_j) = \delta_{ij}$. The hierarchical construction is based on the fact that $I^i(u)$ can represent exactly $I^{i-1}(u)$ if multi-linear basis or spectral basis are used, *i.e.*,

$$I^{i-1}(u) = I^i(I^{i-1}(u)). \quad (4.4.10)$$

By contrast, the proposed SC-ENO method utilize problem-dependent piecewise local basis. Therefore, relation (4.4.10) does not hold any more. For this reason, the hierarchical construction cannot be applied to SC-ENO method. A simple example is given as follows to demonstrate this loss of the hierarchical structure.

Example 4.4.1 (Loss of the hierarchical structure). *Let the underlying solution $u(\xi)$ contains one Heaviside step functions $H(x)$ and a smooth background function:*

$$u(\xi) = \sin\left(\frac{\pi}{4}(\xi + 1)\right) + H(\xi + 1/3) \quad (4.4.11)$$

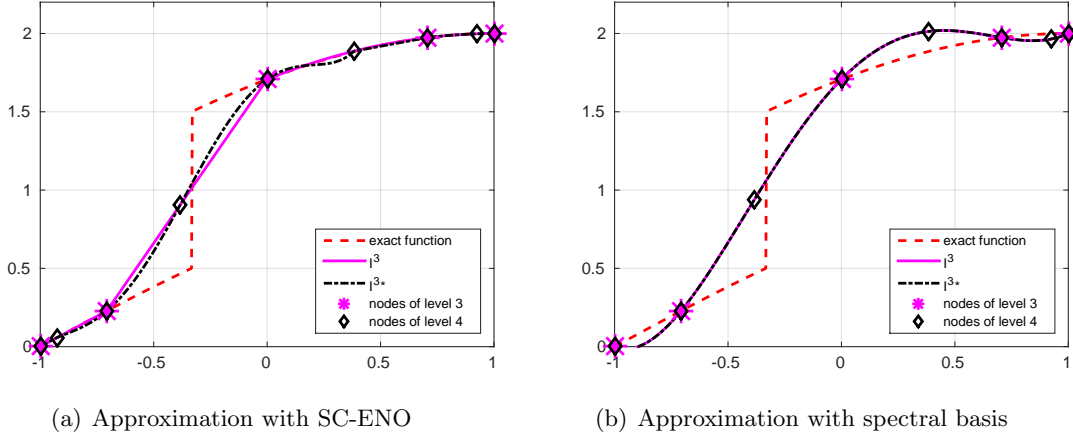


Figure 4.4.1: Loss of hierarchical structure

As we can see from Figure 4.4.1(a), $I^{3*} = I^4(I^3(u)(\xi^4))$ is obtained by interpolation using the level 4 nodes and corresponding values $I^3(u)(\xi^4)$. However, due to the presence of the discontinuity, the piecewise basis of I^3 and the spectral basis of I^{3*} are different, thus $I^3 \neq I^{3*}$ (indicated by the difference between the black line and magenta line). Consequently, equation (4.4.10) does not hold any more. If spectral basis or linear basis is used, $I^{i-1}(u) = I^i(I^{i-1}(u))$ is always guaranteed regardless the smoothness.

This concludes the description of the SC-ENO approach combined with the sparse grid. The performance of the SC-ENO method is presented in the next chapter.

Chapter 5

Numerical examples

This chapter presents numerical results of the proposed SC-ENO method applied to some discontinuous test functions. First of all, the test functions are set up in Section 5.1. Then, the comparison between the traditional stochastic collocation method and the proposed SC-ENO method are made for moderate low-dimensional parameter space in Section 5.2. Meanwhile, the performance of different multivariate interpolation methods are investigated. It should be noted that only low levels of interpolation nodes are considered because the main aim of this work is to improve the accuracy and robustness of uncertainty propagation for complex computational models. Finally, the proposed SC-ENO method is combined into the dimensional adaptive method to combat the *curse of dimensionality* and some results are presented to show its performance.

5.1 Test functions

To investigate the performance of the SC-ENO method, we consider the following three benchmark test functions with discontinuities of arbitrary strengths and manifolds from the Genz function set [24, 38].

$$u^{sphere}(\boldsymbol{\xi}) = \begin{cases} 1 + cu^1(\boldsymbol{\xi}), & \sum_{i=1}^N \xi_i^2 < e^2 \\ cu^1(\boldsymbol{\xi}) & \text{otherwise} \end{cases} \quad (5.1.1)$$

$$u^{cube}(\boldsymbol{\xi}) = \begin{cases} 1 + cu^1(\boldsymbol{\xi}), & \|\xi_i\| < e, \forall i \in \{1, \dots, N\} \\ cu^1(\boldsymbol{\xi}) & \text{otherwise} \end{cases} \quad (5.1.2)$$

$$u^{plane}(\boldsymbol{\xi}) = \begin{cases} cu^1(\boldsymbol{\xi}) + u_N^2(\boldsymbol{\xi}), & 3\xi_1 + 2\xi_2 \leq 0.01 \\ cu^1(\boldsymbol{\xi}) & \text{otherwise} \end{cases} \quad (5.1.3)$$

where

$$u^1(\boldsymbol{\xi}) = \exp\left(-\sum_{i=1}^2 \xi_i^2\right) - \xi_1^3 - \xi_2^3, \quad (5.1.4)$$

$$u_N^2(\boldsymbol{\xi}) = 2 + \frac{1}{2} \cos(\pi(\xi_1 + \xi_2 + 0.3)) + \frac{1}{4N} \sum_{i=2}^N \xi_i^2. \quad (5.1.5)$$

All the test functions above contain a smooth background function $u^1(\boldsymbol{\xi})$ and a jump discontinuity. The jump value can be a constant 1 or a varying function $u_N^2(\boldsymbol{\xi})$. The constant c is a parameter controlling the strengths of the discontinuities as well as the smoothness and variation of the background function. The smaller the value of c is, the smoother the background function is, and the stronger the discontinuity becomes. The parameter e controls the range of the discontinuities. The Gaussian term $\exp(-\sum_{i=1}^2 \xi_i^2)$ in the first two dimensions have large mixed derivatives and thus the increase of accuracy can always be expected with increasing level of interpolation nodes. Figure 5.1.1 shows the response surfaces of these test functions for two-dimensional cases with $c = 0.2, e = 0.7$ and $c = 1, e = 0.7$.

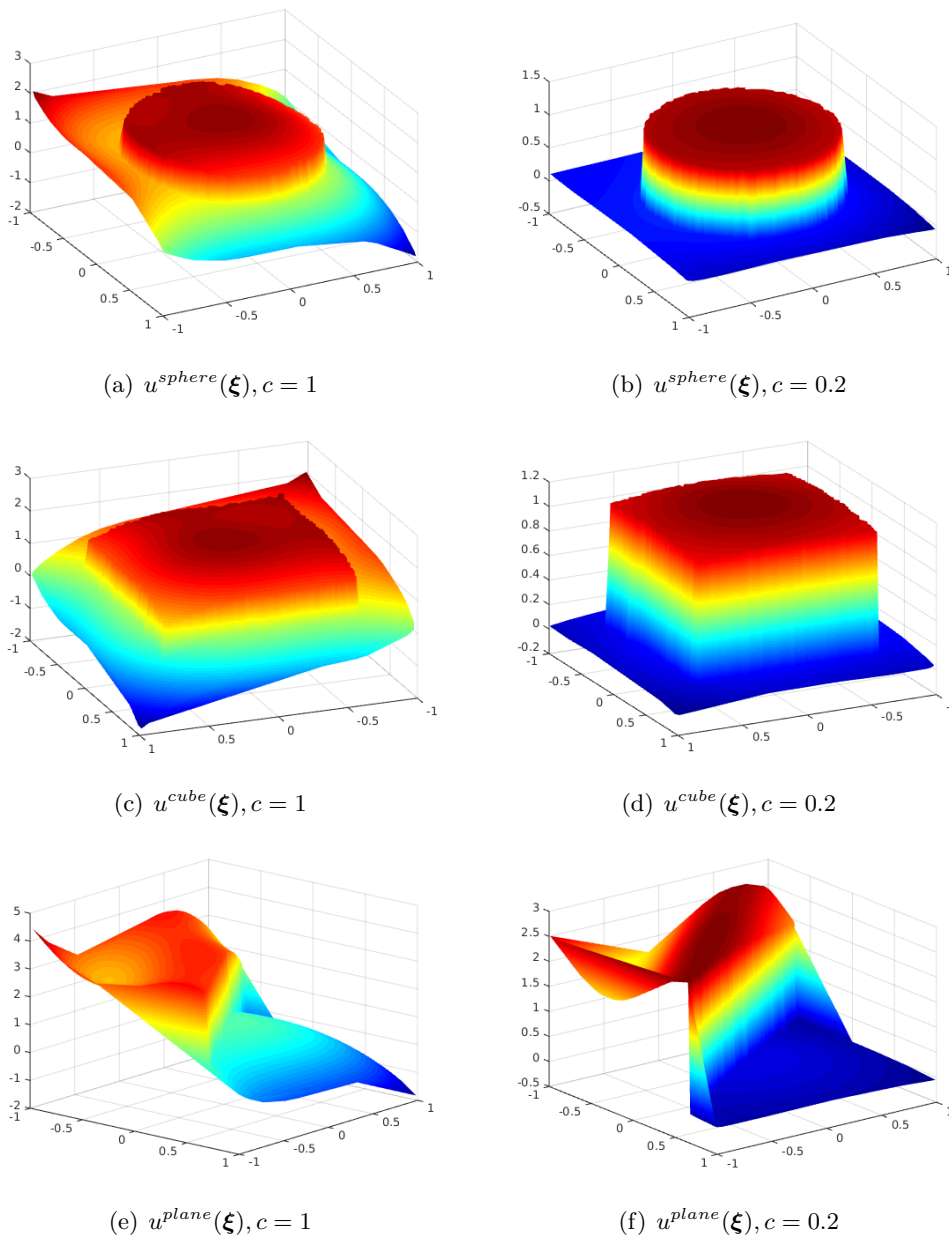


Figure 5.1.1: Response surfaces of the two-dimensional benchmark test functions.

To compare the accuracy and calculate the statistics of output quantity, we run Monte Carlo simulations on the surrogate response surface $w(\boldsymbol{\xi})$. Without loss of generality, we consider discontinuous functions $u(\boldsymbol{\xi}) : \Xi = [-1, 1]^N \mapsto \mathbb{R}$ with N uniformly distributed random parameters. For random parameters following other kinds of probability distribution, the corresponding random number generator will be used to generate the Monte Carlo points. We generate $s_{mc} = 10,000$ Monte Carlo samples on $[-1, 1]^N$. These Monte Carlo samples are classified inside each of the hypercube element $\{\Xi_J\}_{J=1}^{n_e}$. These Monte Carlo simulations are very cheap because they do not involve the expensive deterministic solver. The statistics and the $\mathcal{L}^1, \mathcal{L}^2, \mathcal{L}^\infty$ error can be approximated by:

$$\mu_u \approx \left(\frac{1}{s_{mc}} \cdot \sum_{i=1}^{s_{mc}} w(\boldsymbol{\xi}_i) \right) \quad (5.1.6)$$

$$\sigma = \sqrt{\frac{1}{s_{mc}} \sum_{i=1}^{s_{mc}} (w(\boldsymbol{\xi}_i) - \mu)^2} \quad (5.1.7)$$

$$\|u(\boldsymbol{\xi}) - w(\boldsymbol{\xi})\|_1 \approx \frac{1}{s_{mc}} \cdot \sum_{i=1}^{s_{mc}} \|u(\boldsymbol{\xi}_i) - w(\boldsymbol{\xi}_i)\| \quad (5.1.8)$$

$$\|u(\boldsymbol{\xi}) - w(\boldsymbol{\xi})\|_2 \approx \sqrt{\frac{1}{s_{mc}} \cdot \sum_{i=1}^{s_{mc}} \|u(\boldsymbol{\xi}_i) - w(\boldsymbol{\xi}_i)\|^2} \quad (5.1.9)$$

$$\|u(\boldsymbol{\xi}) - w(\boldsymbol{\xi})\|_\infty \approx \max_{i \in s_{mc}} \|u(\boldsymbol{\xi}_i) - w(\boldsymbol{\xi}_i)\| \quad (5.1.10)$$

5.2 Comparison between traditional SC and SC-ENO

In this section, we illustrate the improvement of accuracy and robustness of the proposed piecewise Stochastic Collocation method compared to the traditional Stochastic Collocation method. To rule out the influence of different multivariate interpolation methods, one-dimensional parameter space is considered first. Then, the performance of the *least interpolation* method and *element-wise interpolation* method is investigated for the two-dimensional case. Finally, numerical results for the moderate high-dimensional case is presented.

5.2.1 One-dimensional case

For the one-dimensional parameter space, the test functions $u^{sphere}(\boldsymbol{\xi})$ and $u^{cube}(\boldsymbol{\xi})$ are the same, so we consider $u^{sphere}(\boldsymbol{\xi})$ and $u^{plane}(\boldsymbol{\xi})$. Here, constant parameter e is chosen to be 0.6 and $c = 0.5$. We perform Stochastic Collocation for each function with Clenshaw-Curtis nodes from level 2 to 8 as indicated in equation (2.4.3). The $\mathcal{L}^1, \mathcal{L}^2$ error are given in Figure 5.2.1.

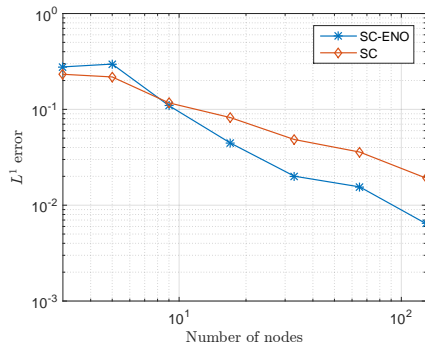
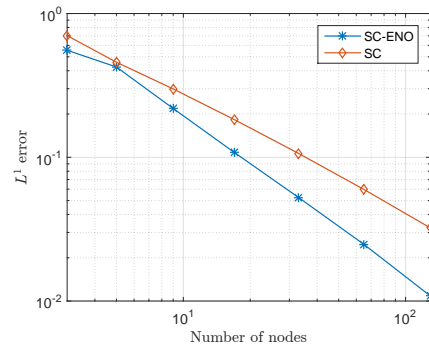
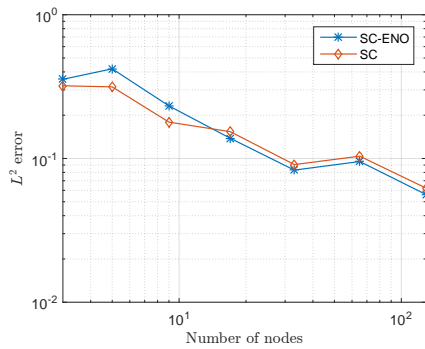
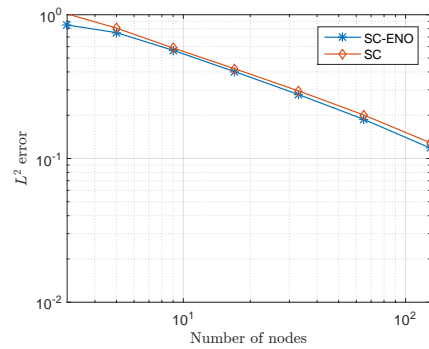
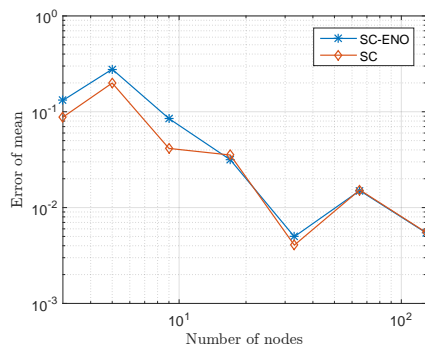
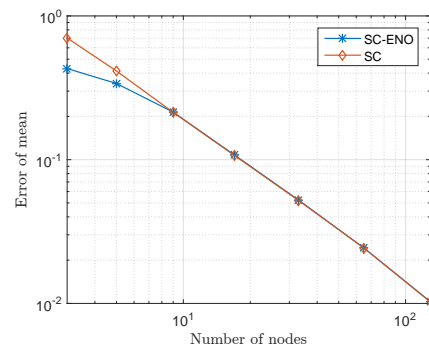
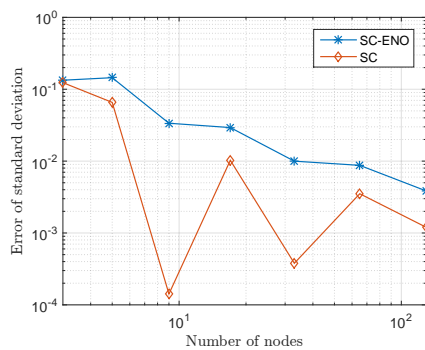
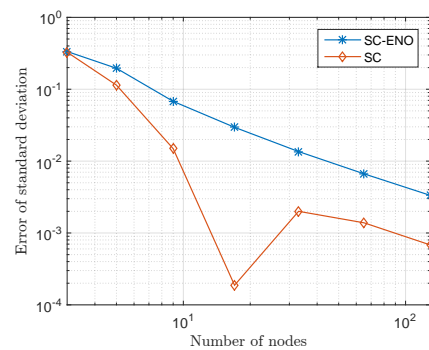
(a) \mathcal{L}^1 error comparison for $u^{sphere}(\xi)$ (b) \mathcal{L}^1 error comparison for $u^{plane}(\xi)$ (c) \mathcal{L}^2 error comparison for $u^{sphere}(\xi)$ (d) \mathcal{L}^2 error comparison for $u^{plane}(\xi)$ (e) Mean value error comparison for $u^{sphere}(\xi)$ (f) Mean value error comparison for $u^{plane}(\xi)$ (g) Standard deviation error comparison for $u^{sphere}(\xi)$ (h) Standard deviation error comparison for $u^{plane}(\xi)$

Figure 5.2.1: Error comparison between traditional SC and SC-ENO on one-dimensional test MS functions $u^{sphere}(\xi)$ and $u^{plane}(\xi)$. Huiqing Wang

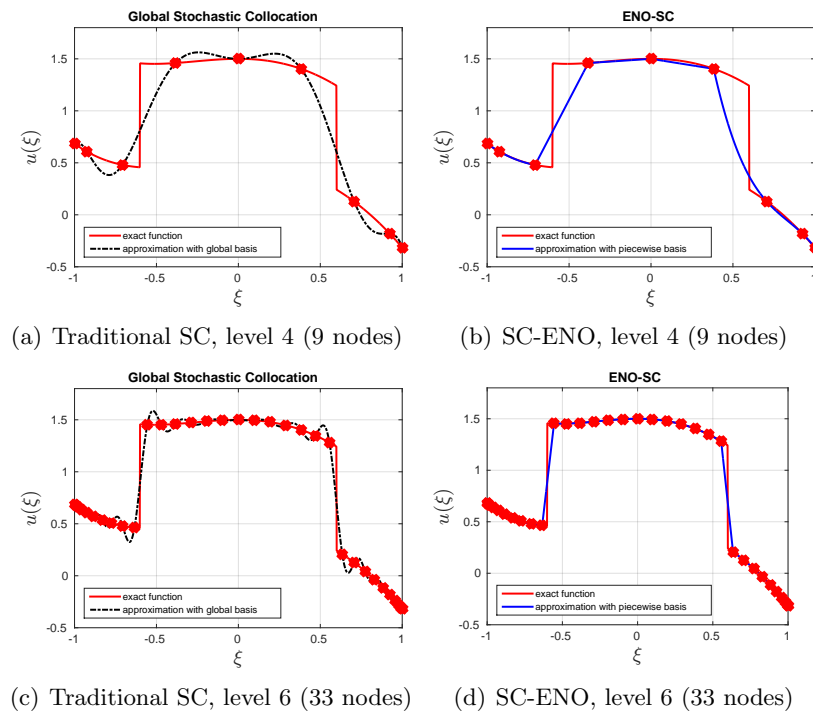


Figure 5.2.2: Response surface for one-dimensional test function $u^{sphere}(\xi)$ with $c = 0.5$, $e = 0.6$.

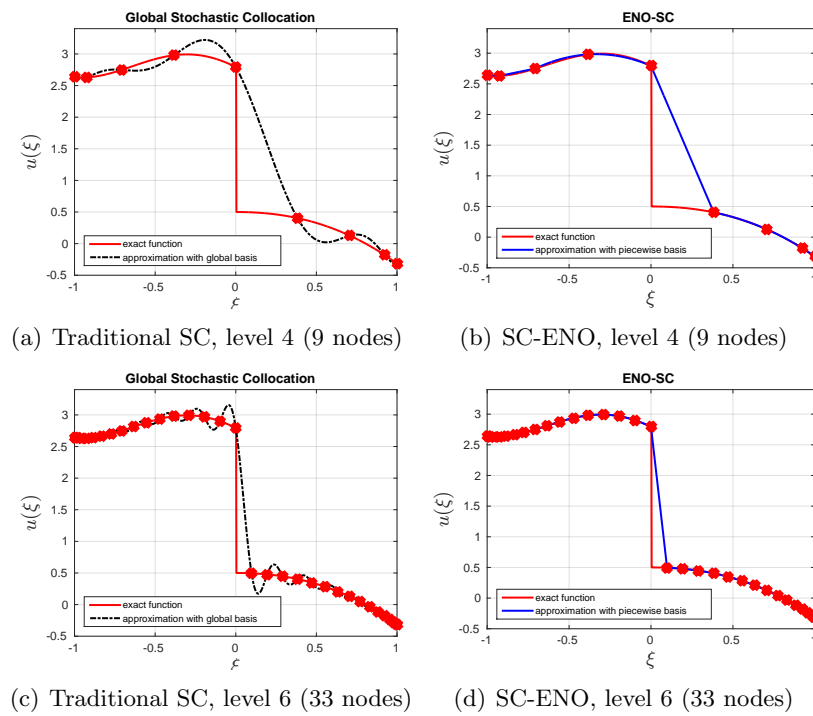


Figure 5.2.3: Response surface for one-dimensional test function $u^{plane}(\xi)$ with $c = 0.5$, $e = 0.6$.

It can be seen that the accuracy of the approximation obtained by the SC-ENO approach increases as the number of the collocation nodes increases. Contrary to the expectation, the accuracy of the SC-ENO method is not as good as traditional SC for low level of nodes. However, it does not mean traditional SC is better. As we can see from the approximated response surface in Figure 5.2.2 and Figure 5.2.3, traditional SC results in several overshoots and undershoots around the discontinuities, which may be unphysical realizations for real cases. By contrast, SC-ENO is able to construct a robust response surface at a relatively low level of the collocation nodes.

It should be noted that the main source of error for the SC-ENO methods comes from the linear approximation inside the discontinuous elements. Even though the error from the smooth elements can be decreased by increasing the number of nodes, the \mathcal{L}^∞ error inside the discontinuous elements stays almost the same and is influenced by the jump value. That's the reason why there is only slightly improved performance. Since we are dealing with discontinuous test functions, the linear interpolation is the reasonable approximation we can use for the elements containing discontinuities. The more sampling nodes we use, the smaller the size of the discontinuous element becomes, and thus the linear interpolation gets closer to a jump discontinuity. In terms of the statistical quantities, *i.e.*, mean and standard deviation, the performance of the SC-ENO is not as good as the SC method for these two test functions.

5.2.2 Two-dimensional case on tensor grid

For the multi-dimensional case, we consider all the two-dimensional test functions with $c = 0.5$ for the sake of visualizing the response surface. Deterministic sampling of test functions is performed for each function with Clenshaw-Curtis nodes from level 2 to 6. Equal importance is given to each dimension due to the underlying isotropic property. The $\mathcal{L}^1, \mathcal{L}^2$ error are given in Figure 5.2.4.

Like the one-dimensional case, the convergence of SC-ENO is slightly faster than the traditional SC method. In terms of the mean value and standard deviation, both the SC and SC-ENO method converges to the exact value as the number of sampling points increase. Their performance varies with respect to different test functions. Numerical tests have been performed for these three test functions using different values of shape parameter c and e . It is observed that the convergence rate differs a lot when the test functions changes. Therefore, we cannot conclude which method is better in terms of the statistical quantities. Further, we can see from Figure 5.2.5 that the response surface obtained by the SC-ENO method is more robust with the spurious oscillations around the discontinuities eliminated.

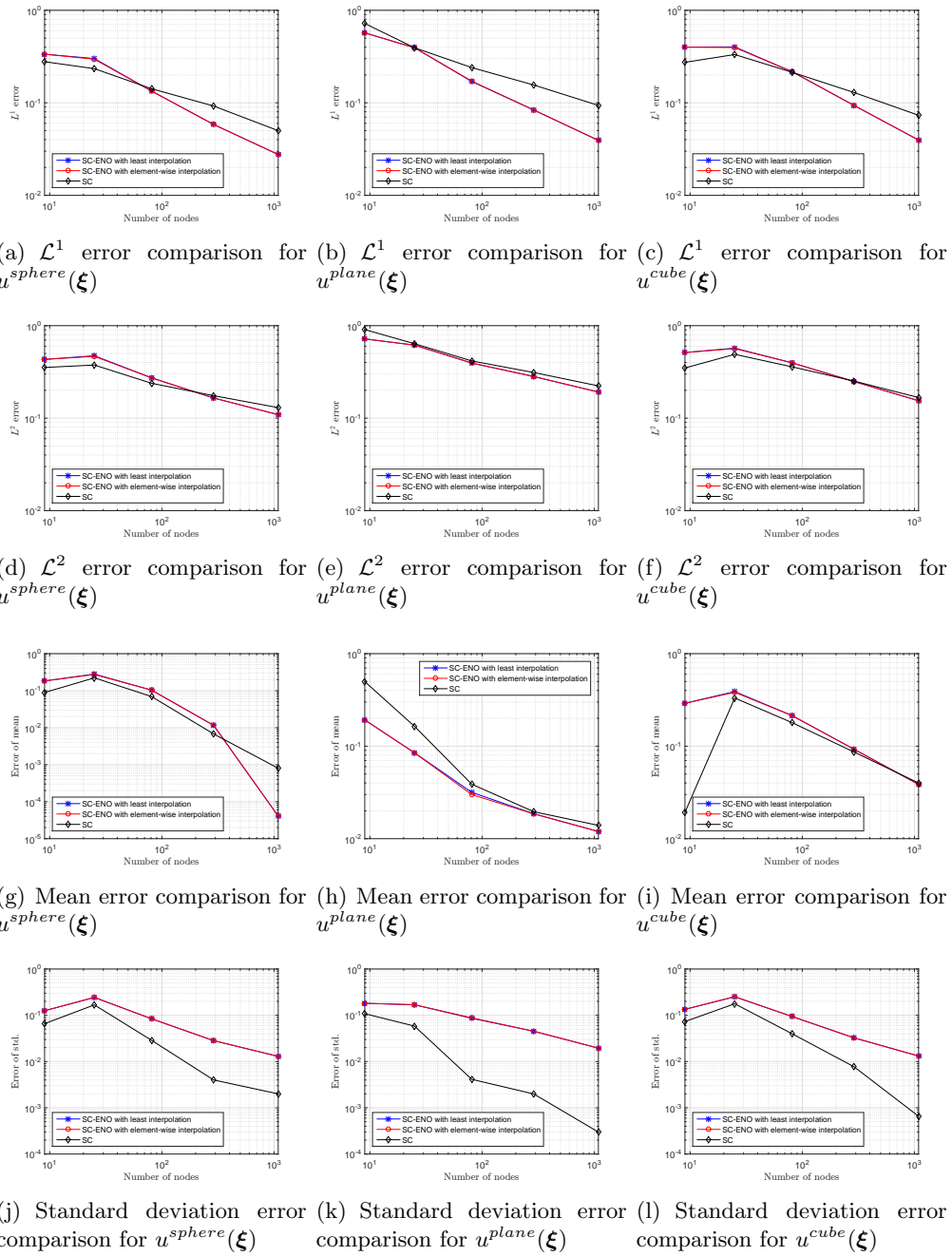


Figure 5.2.4: Error comparison between traditional SC and SC-ENO for two-dimensional test functions $u^{sphere}(\xi)$, $u^{plane}(\xi)$ and $u^{cube}(\xi)$, $c = 0.5$, $e = 0.7$.

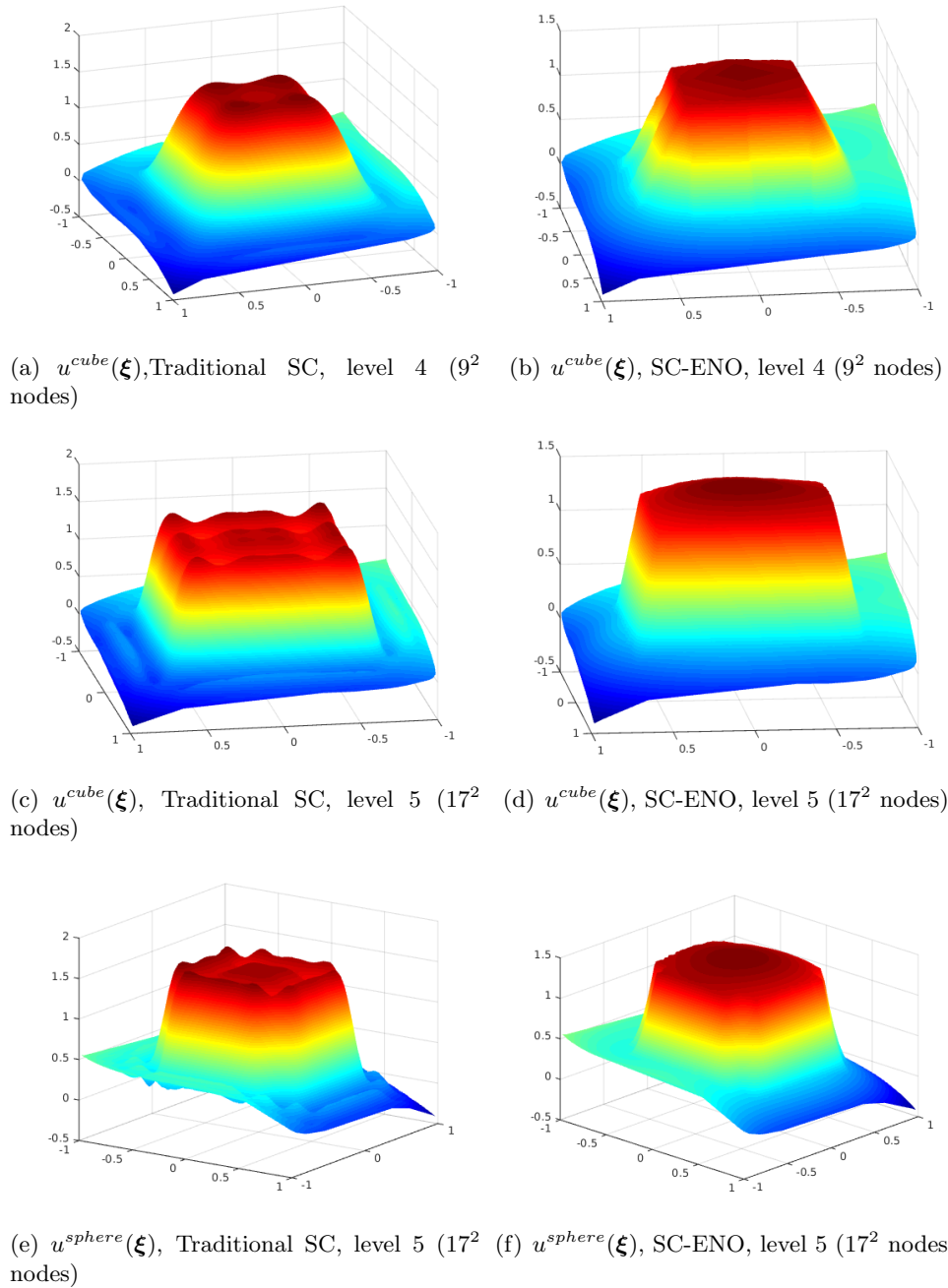


Figure 5.2.5: Response surface for two-dimensional test functions with $c = 0.5$, $e = 0.7$.

Comparison of surrogate constructions inside smooth sub-domains

For the multi-dimensional stochastic space, the choice of the multivariate interpolation methods has an effect on the approximation in each smooth region. Comparison of multivariate interpolations methods are already discussed in Section 4.3.3. Here, comparisons between the least interpolation method and the element-wise interpolation method are made for these discontinuous test functions.

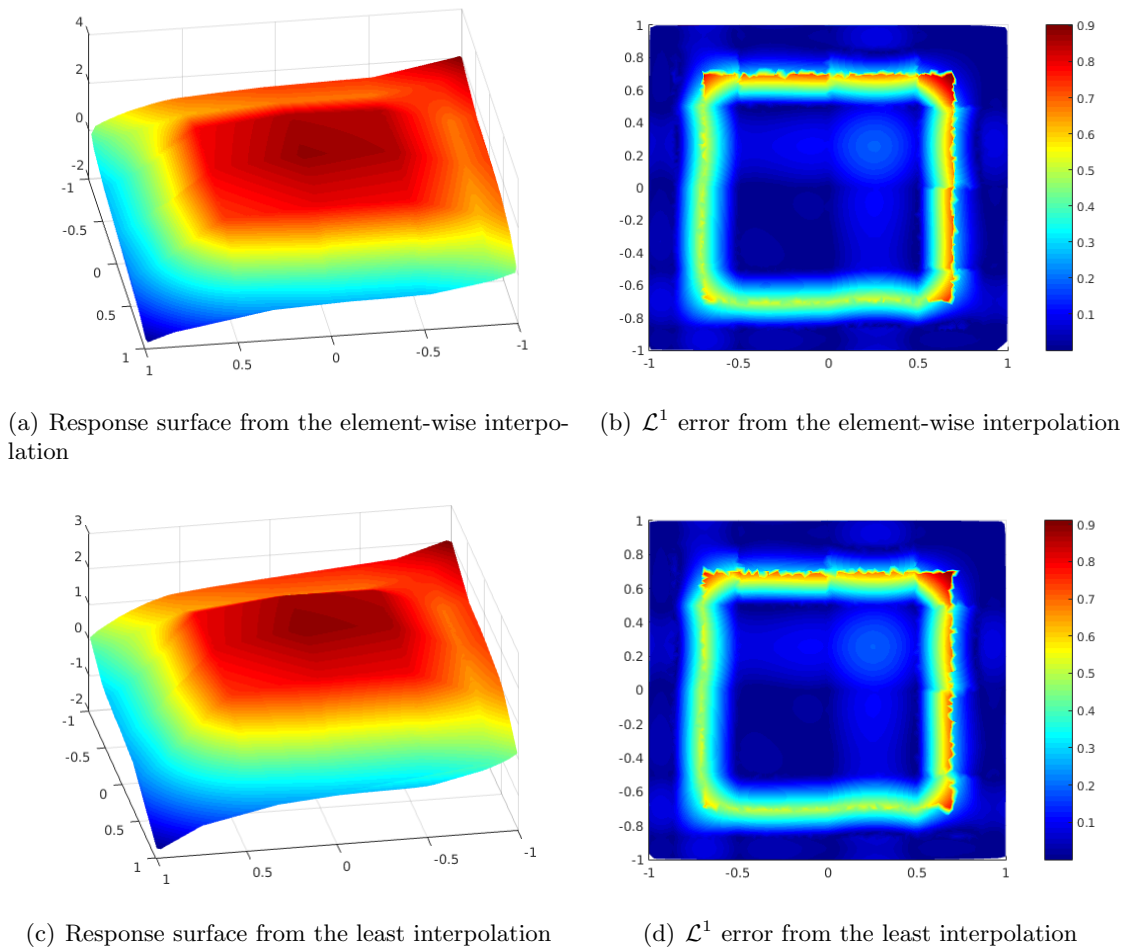


Figure 5.2.6: Comparison between the element-wise interpolation method and the least interpolation method on test functions $u^{cube}(\boldsymbol{\xi})$. with $c = 1$, $e = 0.7$. $\#nodes=7^2$.

As we can see from the Figure 5.2.4 and 5.2.6, both methods do not show a huge difference in terms of accuracy. The disparity between these methods grows smaller with increasing level of nodes. However, compared to the least interpolation, the element-wise interpolation method is more robust, but it loses its continuity of derivatives along the borders of each hypercube element since the patched surrogate is constructed by combining the element-wise approximation. Each element is assigned with its own interpolation stencil of hyper-rectangular shape.

5.2.3 Post-processing time

The proposed SC-ENO method is inherently a post-processing of the given sample values. Therefore, it is theoretically applicable to any dimension. Without loss of generality, tests

are run on a simple high-dimensional step function:

$$u^{step}(\boldsymbol{\xi}) = \begin{cases} 1, & \|\xi_i\| < 0.9, \forall i \in \{1, \dots, N\} \\ 0 & \text{otherwise.} \end{cases} \quad (5.2.1)$$

The error comparison and the post-processing time of the SC-ENO method are given in Table 5.2.1. Since the discontinuity exists in all dimensions, the same number of nodes is needed for each dimension. Here, the full tensor product grid is employed, so the total number of nodes is 5^N .

Table 5.2.1: **Error comparisons and processing time for $u^{step}(\boldsymbol{\xi})$ with 5 nodes in each dimension**

N	SC			SC-ENO			time
	$\epsilon_{\mathcal{L}^1}$	$\epsilon_{\mathcal{L}^2}$	$\epsilon_{\mathcal{L}^\infty}$	$\epsilon_{\mathcal{L}^1}$	$\epsilon_{\mathcal{L}^2}$	$\epsilon_{\mathcal{L}^\infty}$	
1	$9.83 \cdot 10^{-2}$	$1.37 \cdot 10^{-1}$	$5.29 \cdot 10^{-1}$	$3.96 \cdot 10^{-2}$	$1.25 \cdot 10^{-1}$	$6.58 \cdot 10^{-1}$	0.2s
2	$1.49 \cdot 10^{-1}$	$1.93 \cdot 10^{-1}$	$7.26 \cdot 10^{-1}$	$7.59 \cdot 10^{-2}$	$1.75 \cdot 10^{-1}$	$8.22 \cdot 10^{-1}$	0.3s
3	$1.83 \cdot 10^{-1}$	$2.35 \cdot 10^{-1}$	$7.38 \cdot 10^{-1}$	$1.04 \cdot 10^{-1}$	$2.08 \cdot 10^{-1}$	$8.64 \cdot 10^{-1}$	0.9s
4	$2.12 \cdot 10^{-1}$	$2.67 \cdot 10^{-1}$	$9.72 \cdot 10^{-1}$	$1.31 \cdot 10^{-1}$	$2.36 \cdot 10^{-1}$	$8.65 \cdot 10^{-1}$	5.5s
5	$2.31 \cdot 10^{-1}$	$2.89 \cdot 10^{-1}$	1.170	$1.53 \cdot 10^{-1}$	$2.59 \cdot 10^{-1}$	$9.38 \cdot 10^{-1}$	157s

If the discontinuity is of lower-dimensional structure, then we can restrict attention to the parameters ξ causing the discontinuity. For other smooth dimensions, the number of nodes thus can be reduced dramatically to achieve the required accuracy. For example, test function $u^{plane}(\boldsymbol{\xi})$ is a discontinuous function with discontinuity lying in the dimension ξ_1 and ξ_2 . For dimension $\xi_i, i \in \{3, \dots, N\}$, only 3 nodes are needed for each dimension to interpolate accurately the second-order term $\frac{1}{4N} \sum_{i=2}^N \xi_i^2$.

5.3 Sparse grid

This section will show how the traditional SC and SC-ENO methods perform for the discontinuous test functions on the sparse grid. In order to compare with the results of the full tensor product grid, the constant parameter is chosen the same, *i.e.*, $c = 0.5$, $e = 0.7$.

5.3.1 Standard sparse grid

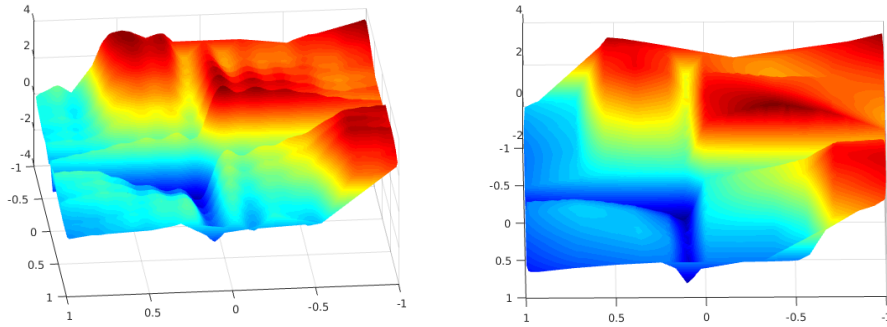
The results obtained with conventional sparse grid for two-dimensional test function $u^{plane}(\boldsymbol{\xi})$ are given in Table 5.3.1 and 5.3.2 . The response surface of level $w = 5$ are given in Figure 5.3.1.

Table 5.3.1: Conventional sparse grid with global basis for $u^{plane}(\boldsymbol{\xi})$, $N = 2$

Approximation	Level 1	Level 2	Level 3	Level 4	Level 5	Level 6
Number of points	5	13	29	65	145	321
$\epsilon_{\mathcal{L}^1}$	$8.19 \cdot 10^{-1}$	$7.29 \cdot 10^{-1}$	$6.79 \cdot 10^{-1}$	$5.43 \cdot 10^{-1}$	$4.78 \cdot 10^{-1}$	$4.04 \cdot 10^{-1}$
$\epsilon_{\mathcal{L}^2}$	1.01	$9.08 \cdot 10^{-1}$	$9.27 \cdot 10^{-1}$	$7.95 \cdot 10^{-1}$	$7.26 \cdot 10^{-1}$	$6.57 \cdot 10^{-1}$
$\epsilon_{\mathcal{L}^\infty}$	3.17	2.84	2.94	2.72	2.84	2.67
ϵ_μ	$2.76 \cdot 10^{-1}$	$8.08 \cdot 10^{-2}$	$2.97 \cdot 10^{-1}$	$3.08 \cdot 10^{-1}$	$2.30 \cdot 10^{-1}$	$1.82 \cdot 10^{-1}$
ϵ_σ	$4.31 \cdot 10^{-2}$	$1.98 \cdot 10^{-1}$	$1.85 \cdot 10^{-1}$	$1.12 \cdot 10^{-1}$	$8.98 \cdot 10^{-2}$	$9.37 \cdot 10^{-2}$

Table 5.3.2: Conventional sparse grid with SC-ENO for $u^{plane}(\boldsymbol{\xi})$, $N = 2$

Approximation	Level 1	Level 2	Level 3	Level 4	Level 5	Level 6
Number of points	5	13	29	65	145	321
$\epsilon_{\mathcal{L}^1}$	$7.38 \cdot 10^{-1}$	$6.21 \cdot 10^{-1}$	$5.56 \cdot 10^{-1}$	$4.67 \cdot 10^{-1}$	$4.32 \cdot 10^{-1}$	$3.69 \cdot 10^{-1}$
$\epsilon_{\mathcal{L}^2}$	1.01	$7.57 \cdot 10^{-1}$	$7.90 \cdot 10^{-1}$	$6.67 \cdot 10^{-1}$	$6.73 \cdot 10^{-1}$	$5.67 \cdot 10^{-1}$
$\epsilon_{\mathcal{L}^\infty}$	3.17	2.58	2.67	2.21	2.37	2.19
ϵ_μ	$2.88 \cdot 10^{-1}$	$5.35 \cdot 10^{-2}$	$2.20 \cdot 10^{-1}$	$1.97 \cdot 10^{-1}$	$1.02 \cdot 10^{-1}$	$2.16 \cdot 10^{-1}$
ϵ_σ	$4.29 \cdot 10^{-2}$	$4.50 \cdot 10^{-2}$	$6.12 \cdot 10^{-3}$	$5.53 \cdot 10^{-3}$	$4.77 \cdot 10^{-2}$	$7.36 \cdot 10^{-2}$



(a) Conventional sparse grid with traditional SC, level $w = 5$ (145 nodes) (b) Conventional sparse grid with SC-ENO, level $w = 5$ (145 nodes)

Figure 5.3.1: Response surface for test functions $u^{plane}(\boldsymbol{\xi})$ with $c = 0.5$, $e = 0.7$.

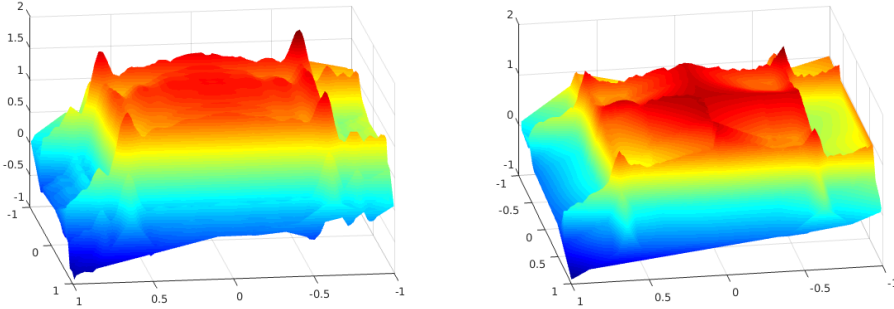
The results obtained with conventional sparse grid for two-dimensional test function $u^{cube}(\boldsymbol{\xi})$ are given in Table 5.3.3 and 5.3.4 . The response surface of level $w = 5$ are given in Figure 5.3.2.

Table 5.3.3: Conventional sparse grid with global basis for $u^{cube}(\xi)$, $N = 2$

Approximation	Level 1	Level 2	Level 3	Level 4	Level 5	Level 6
Number of points	5	13	29	65	145	321
$\epsilon_{\mathcal{L}^1}$	$3.12 \cdot 10^{-1}$	$5.93 \cdot 10^{-1}$	$2.40 \cdot 10^{-1}$	$1.89 \cdot 10^{-1}$	$1.25 \cdot 10^{-1}$	$9.34 \cdot 10^{-2}$
$\epsilon_{\mathcal{L}^2}$	$3.99 \cdot 10^{-1}$	$7.06 \cdot 10^{-1}$	$3.33 \cdot 10^{-1}$	$2.80 \cdot 10^{-1}$	$2.11 \cdot 10^{-1}$	$1.67 \cdot 10^{-1}$
$\epsilon_{\mathcal{L}^\infty}$	1.32	1.75	1.23	0.955	0.961	0.888
ϵ_μ	$1.41 \cdot 10^{-1}$	$5.93 \cdot 10^{-2}$	$8.83 \cdot 10^{-2}$	$3.14 \cdot 10^{-2}$	$2.78 \cdot 10^{-2}$	$3.24 \cdot 10^{-2}$
ϵ_σ	$3.81 \cdot 10^{-2}$	$1.59 \cdot 10^{-1}$	$6.02 \cdot 10^{-2}$	$3.90 \cdot 10^{-2}$	$4.17 \cdot 10^{-2}$	$2.02 \cdot 10^{-2}$

Table 5.3.4: Conventional sparse grid with SC-ENO for $u^{cube}(\xi)$, $N = 2$

Approximation	Level 1	Level 2	Level 3	Level 4	Level 5	Level 6
Number of points	5	13	29	65	145	321
$\epsilon_{\mathcal{L}^1}$	$6.07 \cdot 10^{-1}$	$5.73 \cdot 10^{-1}$	$2.76 \cdot 10^{-1}$	$1.81 \cdot 10^{-1}$	$1.15 \cdot 10^{-1}$	$1.14 \cdot 10^{-1}$
$\epsilon_{\mathcal{L}^2}$	$7.18 \cdot 10^{-1}$	$7.16 \cdot 10^{-1}$	$3.63 \cdot 10^{-1}$	$2.81 \cdot 10^{-1}$	$2.06 \cdot 10^{-1}$	$2.09 \cdot 10^{-1}$
$\epsilon_{\mathcal{L}^\infty}$	1.86	1.49	1.09	1.00	0.943	0.925
ϵ_μ	$5.86 \cdot 10^{-1}$	$5.72 \cdot 10^{-1}$	$1.75 \cdot 10^{-2}$	$2.71 \cdot 10^{-2}$	$2.65 \cdot 10^{-2}$	$6.65 \cdot 10^{-2}$
ϵ_σ	$1.86 \cdot 10^{-2}$	$1.77 \cdot 10^{-2}$	$8.01 \cdot 10^{-2}$	$3.68 \cdot 10^{-2}$	$4.07 \cdot 10^{-2}$	$5.07 \cdot 10^{-2}$



(a) Conventional sparse grid with traditional SC, level $w = 5$ (145 nodes) (b) Conventional sparse grid with SC-ENO, level $w = 5$ (145 nodes)

Figure 5.3.2: Response surface for test functions $u^{cube}(\xi)$ with $c = 0.5$, $w = 0.7$.

We can see from above two examples that conventional sparse grid is not a good choice for discontinuous function. The SC-ENO method outperforms the traditional SC slightly in terms of the accuracy. However, although it is guaranteed that there is no oscillation for each response surface constructed on the sub-tensor product grids, there is a possibility that the linear combination of the non-oscillatory response surfaces would yield a oscillatory one.

Now, we investigate the results obtained by both the SC-ENO method and SC method on the isotropic sparse grid or the tensor grid. For the 2-dimensional test function $u^{plane}(\xi)$, the convergence in terms of \mathcal{L}^1 , \mathcal{L}^2 error and statistical quantities are shown in Figure 5.3.3. It is observed that the SC-ENO method on the full tensor product grid tends to achieve the best result in all aspects, except for the standard deviation. Also, we can see that for

this discontinuous function, the interpolation based on the tensor product grid yields a more stable convergence behaviour than the sparse grid. For another 2-dimensional test function $u^{cube}(\boldsymbol{\xi})$, the results obtained on the sparse grid are slightly better than the tensor grid in terms of the \mathcal{L}^1 and \mathcal{L}^2 error. From the above two examples, it is observed that there is no method or grid distribution that outperforms the others. But in terms of the capability in eliminating spurious oscillations, the SC-ENO method on the full tensor product grid is better, especially when the dimensionality of the stochastic space is low.

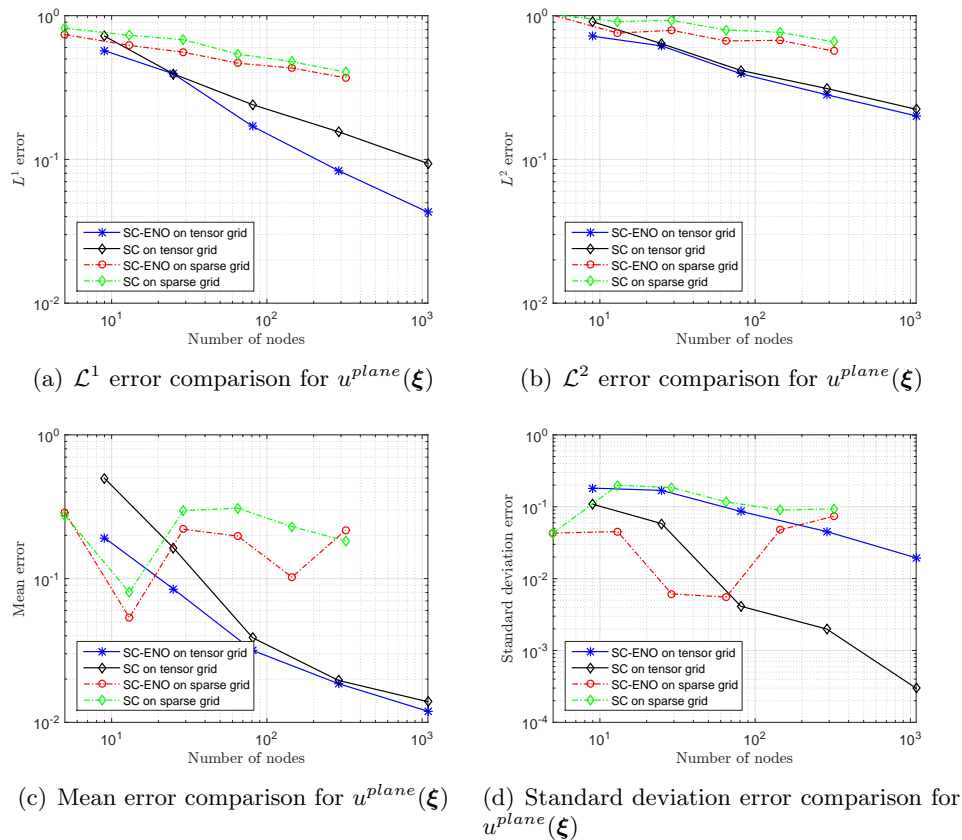


Figure 5.3.3: Error comparison between traditional SC and SC-ENO for two-dimensional test function $u^{plane}(\boldsymbol{\xi})$ on the sparse grid and tensor grid.

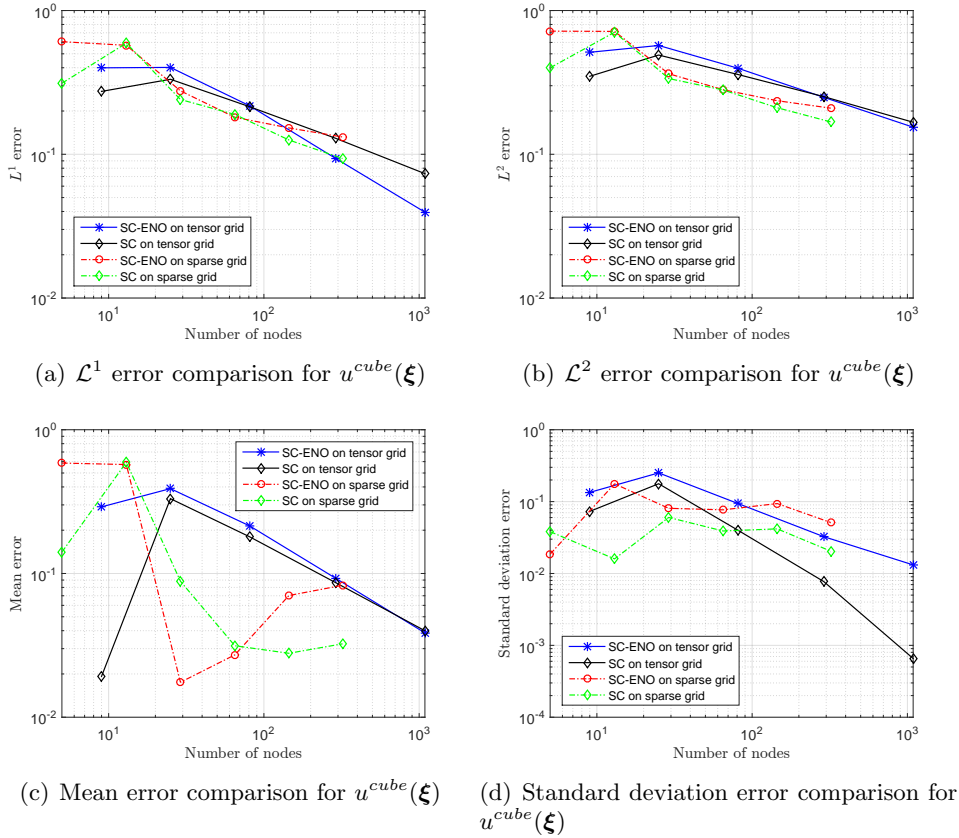


Figure 5.3.4: Error comparison between traditional SC and SC-ENO for two-dimensional test function $u^{cube}(\xi)$, $c = 0.5$, $e = 0.7$ on the sparse grid and tensor grid.

5.3.2 Dimension adaptive sparse grid

In this section, we investigate the performance of the the SC-ENO method combined with dimension adaptive sparse grid method. A even weighted combination of the expectation (4.4.4) and amount of work (4.4.6) is used as the error estimate, *i.e.*, $g^{\mathbf{k}} = 0.5(1/g_{\#}^{\mathbf{k}} + g_{\mathbb{I}}^{\mathbf{k}})$. As for the stopping criteria, the number of nodes is used instead of global error. As we can see from the following examples of adaptive index evolution, the dimension-adaptive algorithm tends to refine low order interaction term. However, the refinements in low order interaction term does not lead to convergence. The error stays almost unchanged, which makes it unreliable to be stopping criteria.

First, test are run on the two-dimensional functions $u^{cube}(\xi)$ and $u^{plane}(\xi)$. We force the adaptive algorithm stop if about 150 nodes are used. The final index set \mathbb{I} is shown in Figure 5.3.5. The response surface is shown is Figure 5.3.2.

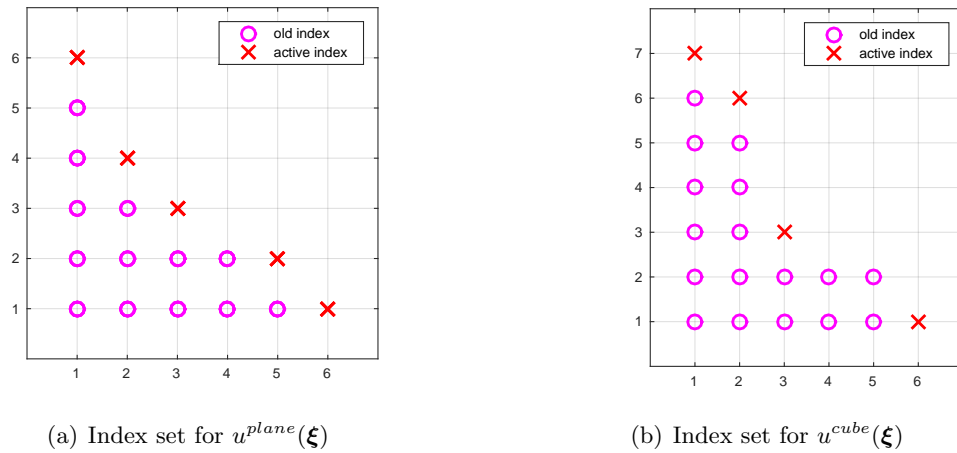
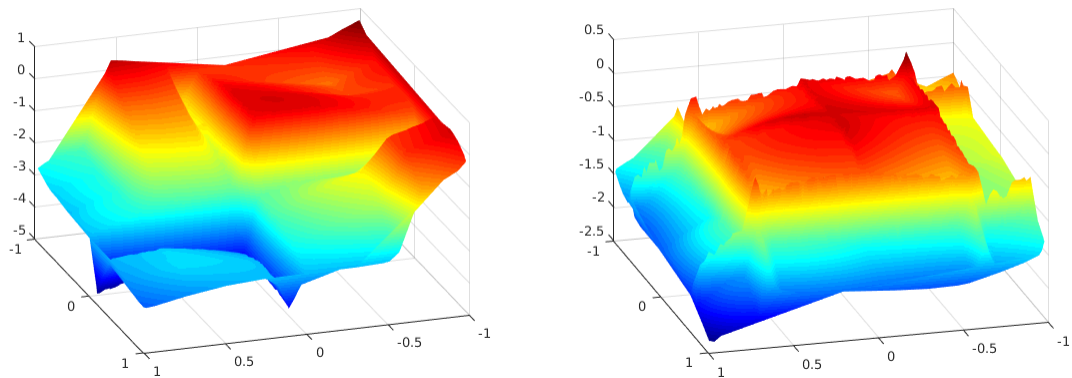


Figure 5.3.5: 3-D index set obtained by dimension adaptive sparse grid algorithm.



Similar to the conventional sparse grid, the results obtained by the generalized adaptive sparse grid is not as good as expected. However, for high-dimensional problem, the dimension-adaptive algorithm is still capable of focusing more on the dimensions that need refinement. If we apply the algorithm to 3-dimensional test functions $u^{cube}(\xi)$ and $u^{plane}(\xi)$, the index set together with the number of nodes are shown in Figure 5.3.6. The low resolution in the third dimension for test function $u^{plane}(\xi)$ is exactly as expected since the discontinuity exists in the first two dimensions.

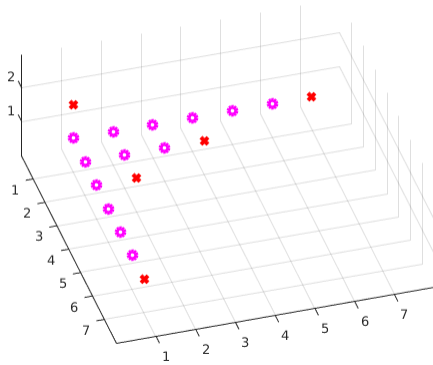
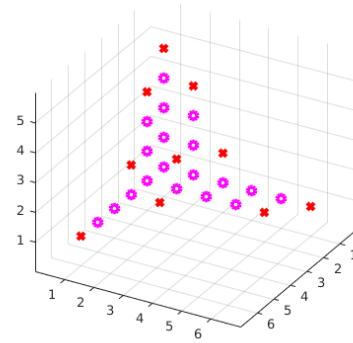
(c) Index set for $u^{plane}(\xi)$, with $S = 151$ nodes.(d) Index set for $u^{cube}(\xi)$, with $S = 165$ nodes.

Figure 5.3.6: 3-D index set obtained by dimension adaptive sparse grid algorithm.

To conclude, the robustness of the proposed SC-ENO approach on the tensor product grid are illustrated. However, the linear combinations of them cannot guarantee a robust response surface.

Chapter 6

Uncertainty quantification for shock tube problem

This chapter shows the comparison of the proposed SC-ENO method with the SC method and the Subcell Resolution (SR) method for the shock tube problem with uncertainties in initial conditions. Inspired by the numerical results on test functions, the full tensor product Clenshaw-Curtis points are used as the deterministic sampling points. First, the shock tube test case is discussed after which the deterministic solution is explained. Then, comparisons of different methods are made in section 6.4, with respect to the statistics of the QOI and the response surface in the parameter space for a certain physical location.

6.1 Shock tube test case descriptions

The Sod's Riemann problem is a classical test case to study the solutions of hyperbolic conservation laws. Simplex Stochastic Collocation (SSC) method has been applied to this problem to investigate the propagations of uncertainties in initial conditions [74, 75]. The computational model can be represented by the following differential conservative form of 1-D Euler equations:

$$\frac{\partial \mathbf{U}}{\partial t} + \frac{\partial \mathbf{F}}{\partial x} = 0, \quad (6.1.1)$$

with state vector of the conservative variables \mathbf{U} and flux vector \mathbf{F}

$$\mathbf{U} = \begin{bmatrix} \rho \\ \rho u \\ \rho E \end{bmatrix}, \quad \mathbf{F} = \begin{bmatrix} \rho u \\ \rho u^2 + p \\ \rho u E + pu \end{bmatrix}, \quad (6.1.2)$$

where ρ is the density, and E is the total energy per unit mass. For a perfect gas, we have $p = \rho RT$, $\gamma = C_p/C_v$ and $E = C_v T + \frac{1}{2}u^2$.

The finite physical domain is confined to $x \in [-0.2; 2]$ with reflective boundary conditions. The initial conditions $\mathbf{U}_0(x)$ for the static pressure p , the density ρ and the velocity on the both sides of a diaphragm at x_0 are given by the Sod's Riemann problem:

$$\begin{cases} u_{left} = 0, \\ p_{left} = 1, \\ \rho_{left} = 1, \end{cases} \quad \begin{cases} u_{right} = 0, \\ p_{right} = 0.1, \\ \rho_{right} = 0.125. \end{cases} \quad (6.1.3)$$

The uncertainties are imposed on the initial left static pressure $p_{left} \in [0.9; 1.1]$ and the location $x_0 \in [-0.025; 0.025]$ of the initial discontinuity with uniform distributions. The output quantity of interest is the density across the whole spatial domain.

6.2 Deterministic simulation

The Euler equations (6.1.1) are solved using a second order front tracking method [77, 69]. Known to be an effective tool for resolving discontinuities in the solution of the hyperbolic conservation laws, front tracking method is not susceptible to the numerical diffusion, consequently resulting in sharp jumps in the physical space. Characteristic fronts are used to discretize the rarefaction wave, the number of which is chosen to be $n_f = 64$ based on a convergence study [74]. The deterministic solution at $t = 1$, with medium value of uncertain inputs $p_{left} = 1, x_0 = 0$, is shown in Figure 6.2.1. Apart from the shock wave around $x = 1.75$, the contact surface results in a discontinuity in the density field around $x = 0.8$ as well.

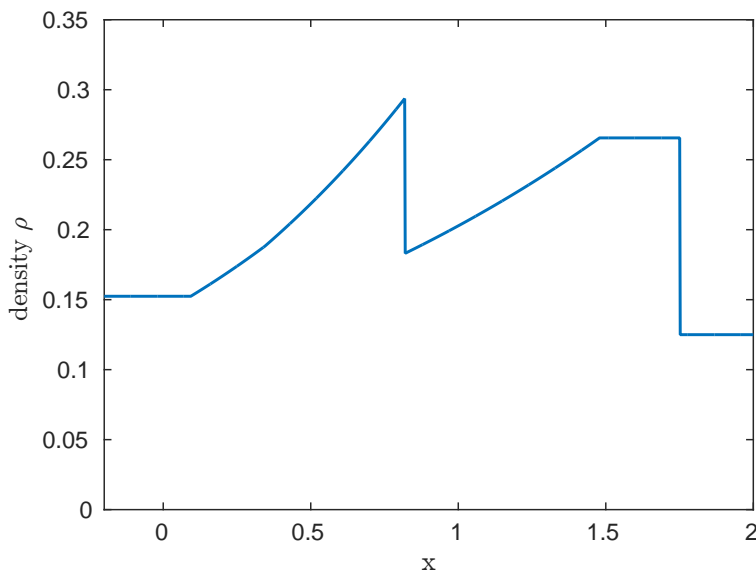


Figure 6.2.1: Deterministic density distribution at $t = 1, n_f = 64$.

6.3 Reference Monte Carlo results

10,000 Monte Carlo simulations are performed to serve as the reference result based on a convergence study. The mean and full confidence interval of the density field is depicted in Figure 6.3.1(a). Different from the deterministic solutions, the shock and contact waves are smeared due to the effects of the uncertainties on initial conditions. Subsequently, a large variation shows up in the discontinuity regions due to the highly non-linear property of the underlying hyperbolic system. It should be noted that there is no uncertainty at the right boundary since that region lies outside the influence domain of p_{left} and x_0 [74].

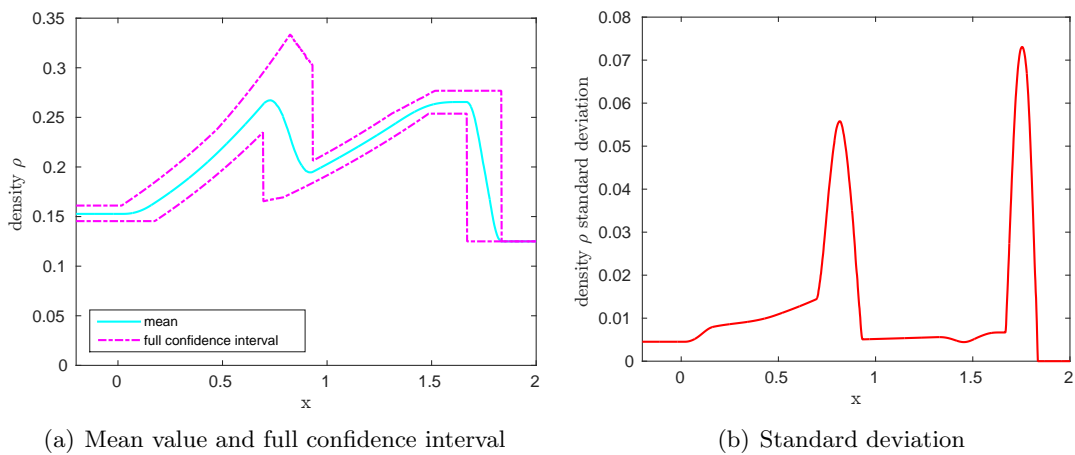


Figure 6.3.1: Reference stochastic results of the density field based on 10,000 MC simulations

6.4 Uncertainties propagation results with SC, SC-ENO and SR methods

In this section, the performances of different uncertain quantification methods are compared. To exclude the impact of sampling nodes, the same Clenshaw-Curtis nodes are used for parameter sampling in each dimension of the parameter space and a full tensor product grid is employed.

6.4.1 Uncertain density at $x = 0.82$

The large standard deviation in the discontinuity regions results from the discontinuous response surface in the parameter space. The reference result obtained by Monte Carlo simulations is shown in Figure 6.4.1. As a result of the moving location of the contact surface, the response is composed of two smooth regions, which are separated by a curved diagonal discontinuity of varying strength.

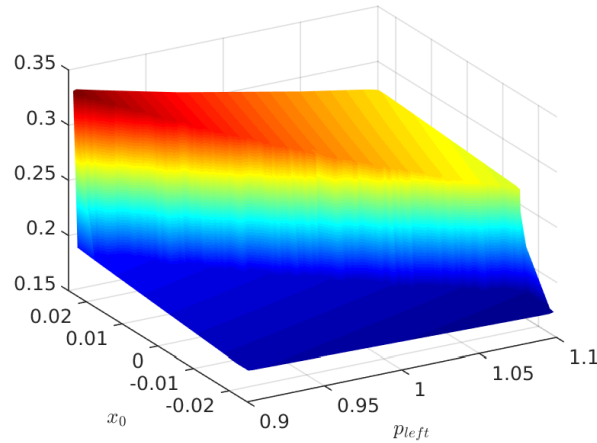


Figure 6.4.1: Response surface at $x = 0.82$ with 10,000 Monte Carlo simulations.

To show the efficacy of the SC-ENO method in dealing with Gibbs oscillations, the response surface of ρ in the parameter space is approximated using increasing level of Clenshaw-Curtis nodes. The results are displayed in Figure 6.4.2 and Figure 6.4.3. While there exists Gibbs oscillations around the discontinuity for the SC method, the SC-ENO yields a robust approximation and converges to the reference result. With increasing number of sampling nodes, the size of discontinuous elements in the parameter space grows smaller and the linear interpolation inside them converges to the sharp discontinuity. For the interpolation in the smooth sub-domains, the SC-ENO can achieve almost zero error in direct contrast to the SC method, in which case the oscillations even exist away from the discontinuity.

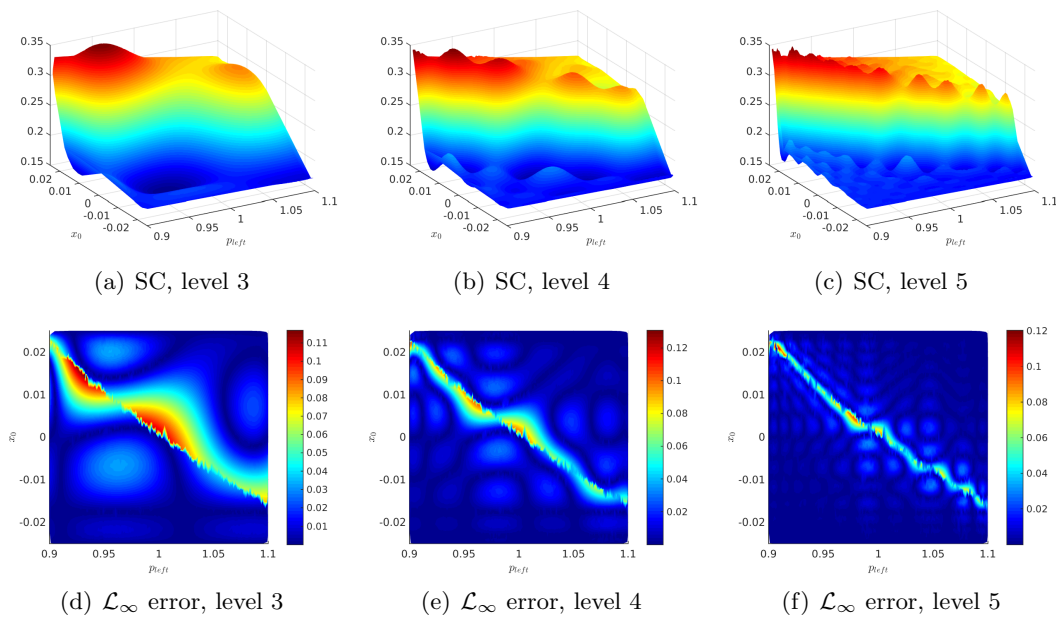
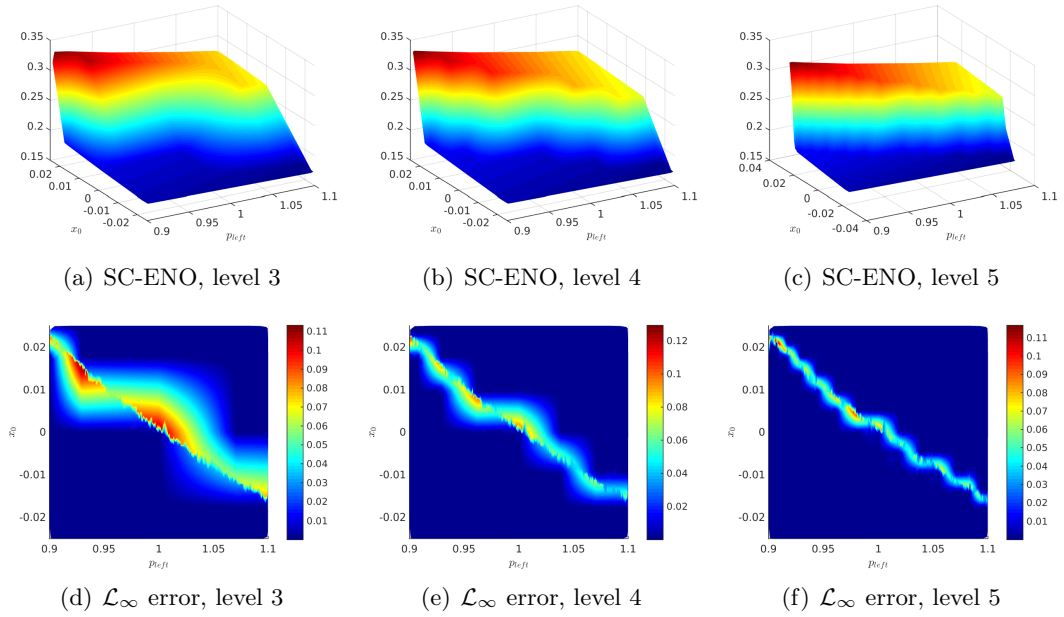


Figure 6.4.2: Response surface and \mathcal{L}_∞ error at $x = 0.82$ with SC

Figure 6.4.3: Response surface and \mathcal{L}_∞ error at $x = 0.82$ with SC-ENO

Although effective in removing Gibbs oscillations, the SC-ENO method still needs further improvement in terms of the resolution of the discontinuity location inside the discontinuous element. To this end, the subcell resolution (SR) concept is introduced to approximate the exact locations of discontinuity. Different from the implementation in [75], the *least interpolation method* is used to construct the surrogate by interpolating all the sampling nodes inside each smooth sub-domain.

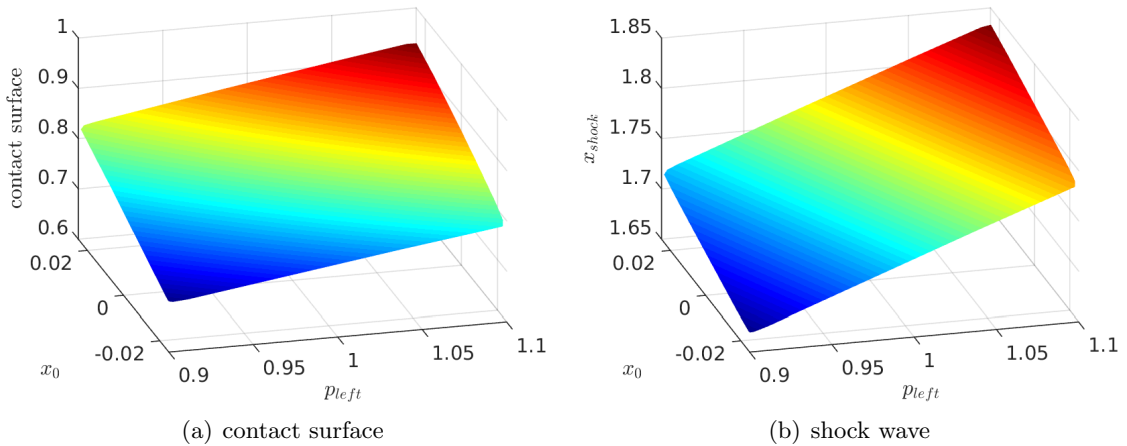


Figure 6.4.4: Approximation of the discontinuity locations in the parameter space with 25 sampling nodes

Two monotonic functions $w_{shock}(\xi)$ are obtained by interpolating the physical discontinuity locations as a function of two random inputs p_{left} and x_0 . Consequently, the locations of the discontinuity in the parameter space for a certain physical location can then be resolved

by finding the intersection of the hyperplane with the function $w_{shock}(\xi)$. Once the discontinuity location is resolved, the surrogate constructed in each smooth sub-domain can be extended to the predicted location of discontinuity. The response surfaces and \mathcal{L}_∞ error are shown in Figure 6.4.5. For this test case, the SR method can achieve a fairly good accuracy with a relatively small number of sampling nodes. The interpolation error at a few points in the parameter space may result from the approximation of the discontinuity locations.

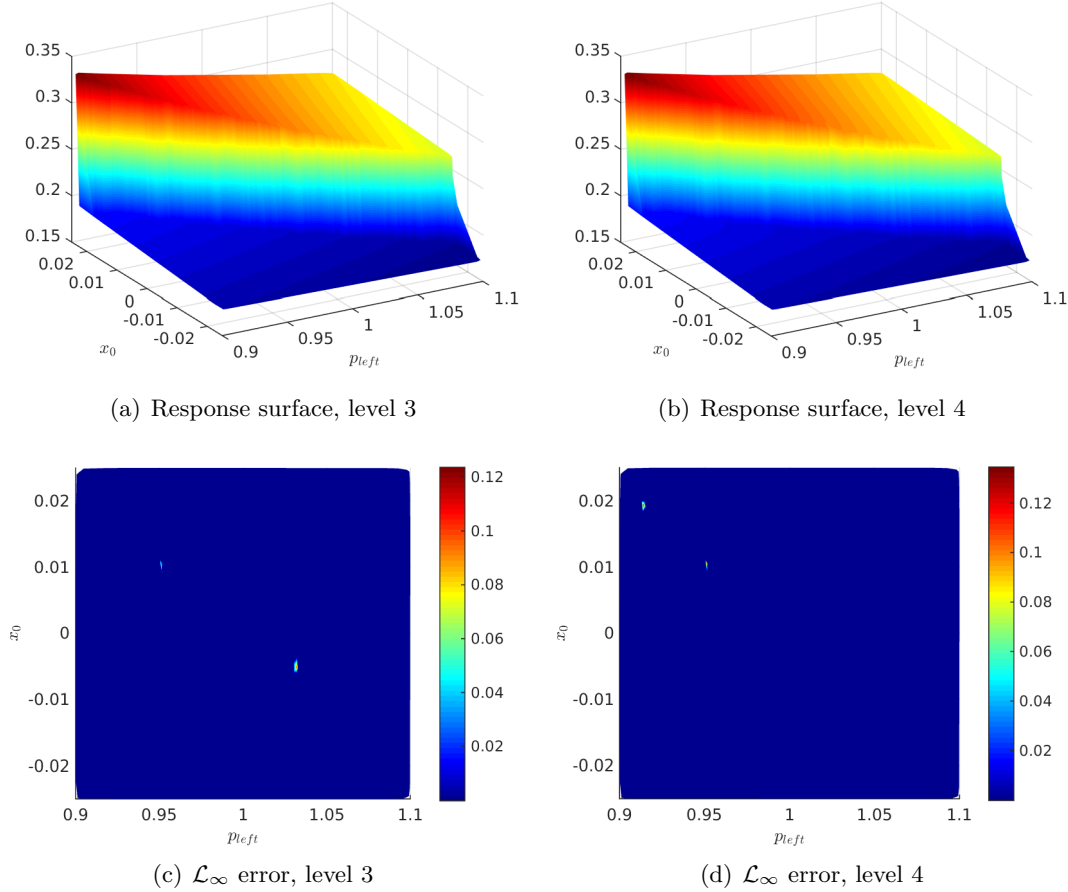


Figure 6.4.5: Response surface and \mathcal{L}_∞ error at $x = 0.82$ with SR

6.4.2 Statistics and full confidence interval of the whole field

The mean value and the full confidence interval of the density field obtained with the SC, SC-ENO and SR method using $n_s = \{25, 81\}$ sampling nodes are shown in Figure 6.4.6, 6.4.7 and 6.4.8. Compared to the SC method, both of the SC-ENO method and the SR method succeed in suppressing oscillations in the discontinuity regions, thus resulting in a physical and robust approximation of the mean value and the full confidence interval.

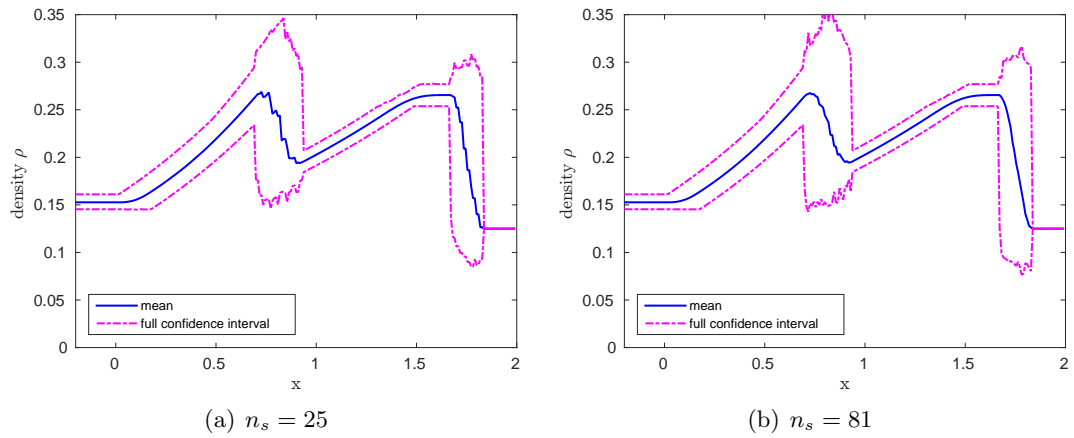


Figure 6.4.6: Mean value of the density and full confidence interval obtained with SC

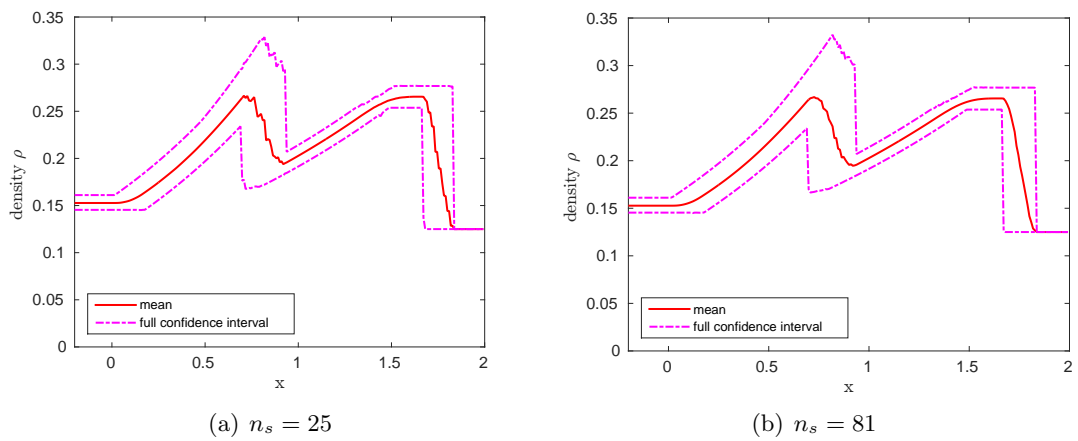


Figure 6.4.7: Mean value of the density and full confidence interval obtained with SC-ENO

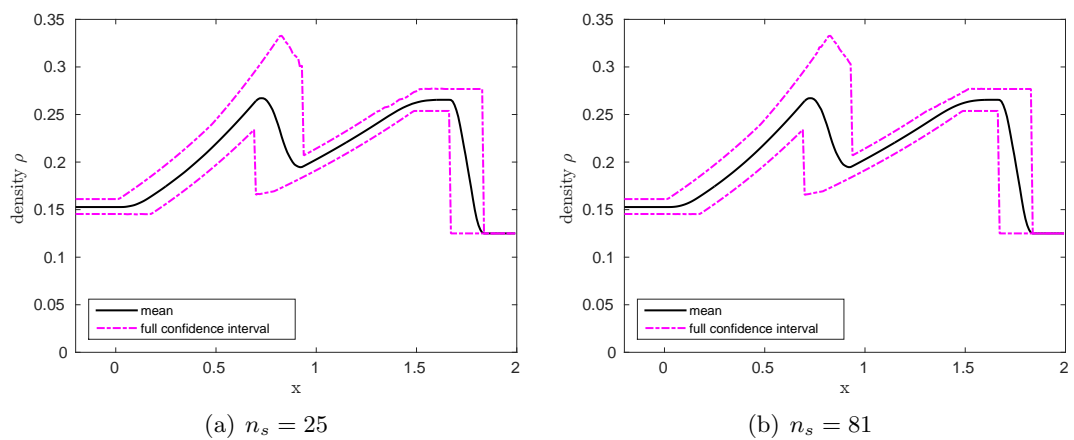


Figure 6.4.8: Mean value of the density and full confidence interval obtained with SR

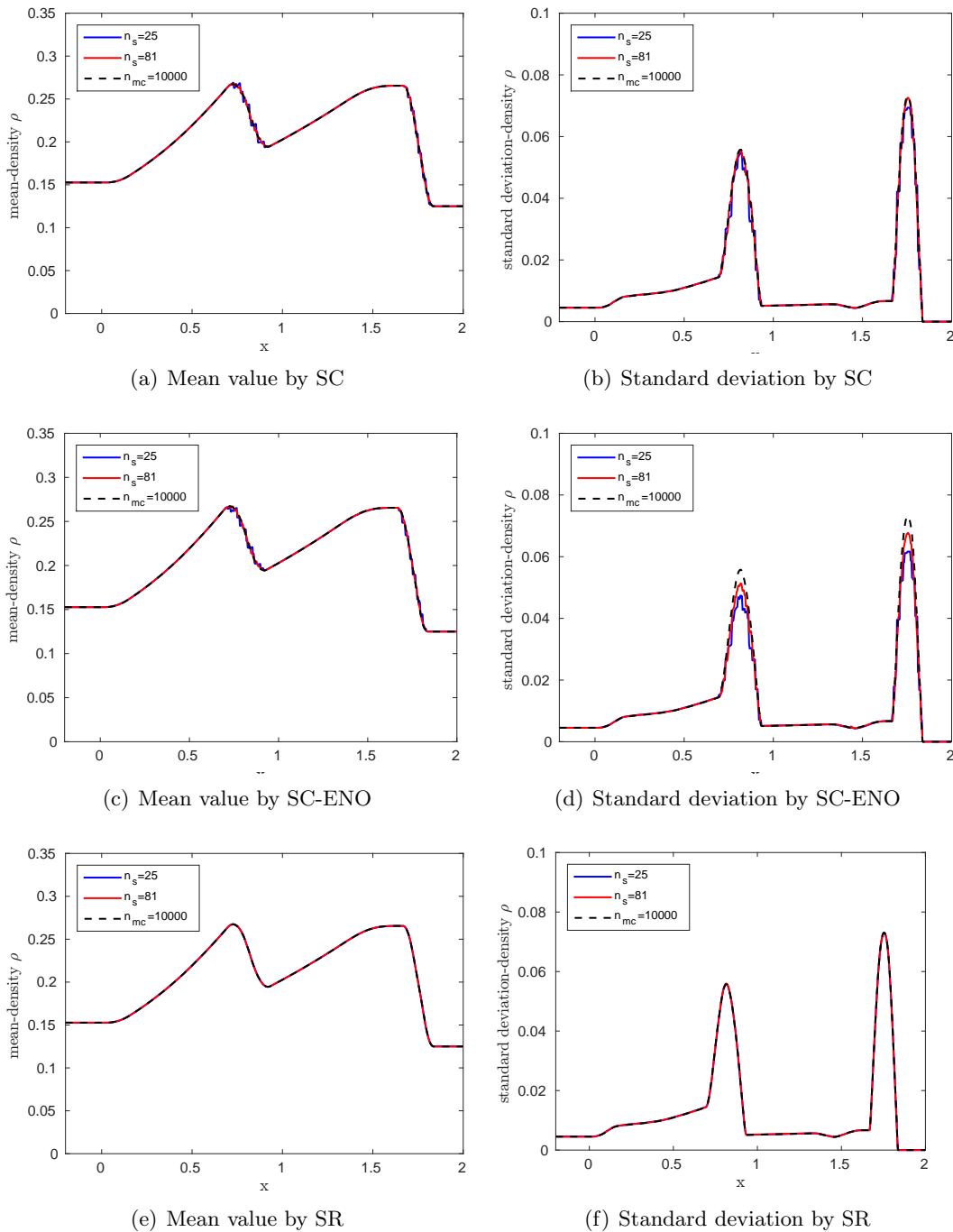


Figure 6.4.9: Statistical moments for the density field obtained with the SC, SC-ENO and SR method

However, due to the linear interpolation for the discontinuous element in the parameter space, the solution obtained by the SC-ENO method remains the same unless the discontinuity moves across a sampling point. Consequently, the phenomenon of staircase approximation of the mean shows up for the SC-ENO method. The larger number of sampling nodes, the smaller the size of the staircase jumps. This is further demonstrated in Figure 6.4.9 for the

convergence of the mean and the standard deviation with $n_s = \{25, 81\}$.

Chapter 7

Uncertainty quantification for RAE 2822 airfoil

In this chapter, the non-intrusive Stochastic Collocation method with ENO robustness is applied to a steady flow around a transonic RAE 2822 airfoil, which is one of the test cases of the UMRIDA project ¹. Two aerodynamic uncertainties, *i.e.*, freestream Mach number M_∞ and angle of attack α , are modeled by independent uniform or symmetric beta distribution ($\alpha = 4, \beta = 4$) under the probabilistic framework. Due to the low dimensionality of the stochastic space, the deterministic sampling on tensor product grids is affordable. What's more, the robustness can be maintained. The test case description is given in Section 7.1, followed by the deterministic simulation in Section 7.2. Then, the uncertainty propagation results are presented in Section 7.3 and Section 7.4.

7.1 RAE 2822 airfoil test case descriptions

The test case of the transonic flow over the RAE 2822 airfoil corresponds to the case 6 in [11], of which the freestream flow conditions is listed in table 7.1.1.

Table 7.1.1: **Original freestream flow conditions**

Mach number	Reynolds number	Angle of attack
0.725	$6.5 \cdot 10^6$	2.92°

It should be noted that due to the slight differences between the design coordinates of the

¹UMRIDA: Uncertainty Management for Robust Industrial Design in Aeronautics is a European Union's research project under grant agreement ACP3-GA-2013-605036

airfoil geometry and the actually measured airfoil in wind tunnel tests, the measured profile is used for the grid generation, which is shown in Figure 7.1.1.

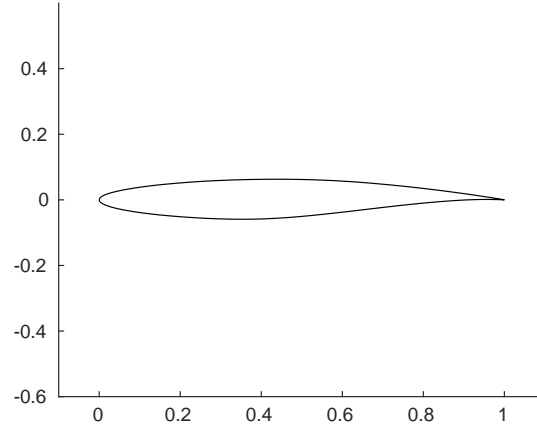


Figure 7.1.1: The measured RAE2822 airfoil geometry

Apart from the geometry differences, the experimental flow conditions needs to be corrected to eliminate the wall interference. Then, the corrected freestream flow conditions are considered here, which are listed as follows:

Table 7.1.2: Corrected freestream flow conditions

Mach number	Reynolds number	Angle of attack
0.729	$6.5 \cdot 10^6$	2.31°

Operational uncertainties are imposed on the Mach number and the angle of attack with medium value from Table 7.1.2. The uncertain interval for the Mach number is [95%–105%], while [98%–102%] for the angle of attack. It should be noted that we impose the same probability distribution for both parameters since we do not want to favor any particular random parameter, although different distributions for different parameters are not incompatible with the SC-ENO formulation. In previous stochastic studies of flow around transonic airfoils [10, 70], the same methodology is employed. Different from the test case descriptions of the UMRIDA workshop, where symmetric beta distribution is used, uniform distribution is added here for the reason that the uniform distribution contains more uncertainty than any other continuous distribution on an interval of compact support. It would be interested to see the influences of different probabilistic characterizations of uncertain inputs. The Reynolds number is kept fixed at $Re=6.5 \cdot 10^6$, consequently, the dynamics viscosity μ changes with varying freestream velocity due to the uncertain Mach number M_∞ .

The quantities of interest (QOI) are the lift coefficient C_l , drag coefficient C_d , pitching moment coefficient C_m , whole pressure field and pressure coefficient C_p along the surface of

airfoil, of which the mean, standard deviation and probability density function are solved. The moment reference point is chosen as $(x, y) = (0.25, 0)$ in the coordinate system of Figure 7.1.1.

7.2 Deterministic simulation

The deterministic steady-state flow solutions are computed based on solving the Reynolds-Averaged Navier-Stokes (RANS) equations using the commercial software of NUMECA. The structured hexahedral mesh provided by the UMRIDA workshop is used, which consists of $9 \cdot 10^4$ volumes, as seen in Figure 7.2.1.

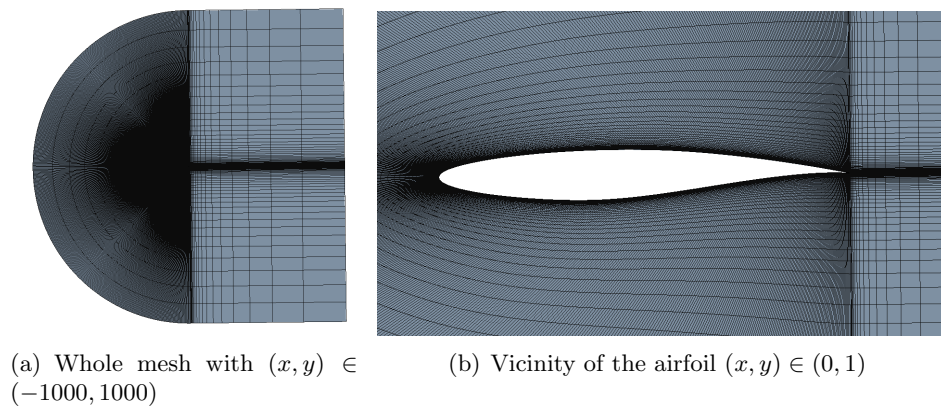


Figure 7.2.1: Spatial mesh

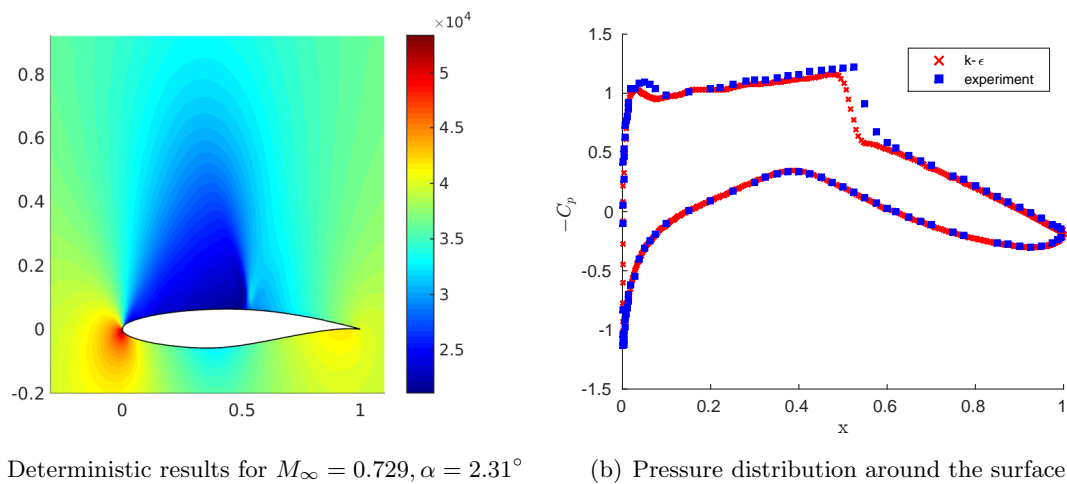


Figure 7.2.2: Deterministic validation against experimental data from [11] of RAE 2822 airfoil

After comparison with the experiment data, the $k - \epsilon$ turbulence model is used for the turbulence modelling. The second order central scheme is used for the spatial discretization.

All simulations are performed using the Courant-Friedrichs-Lewy (CFL) number equal to 1 and converged to the residual of order 10^{-6} . Each simulation takes about 50 hours on one core.

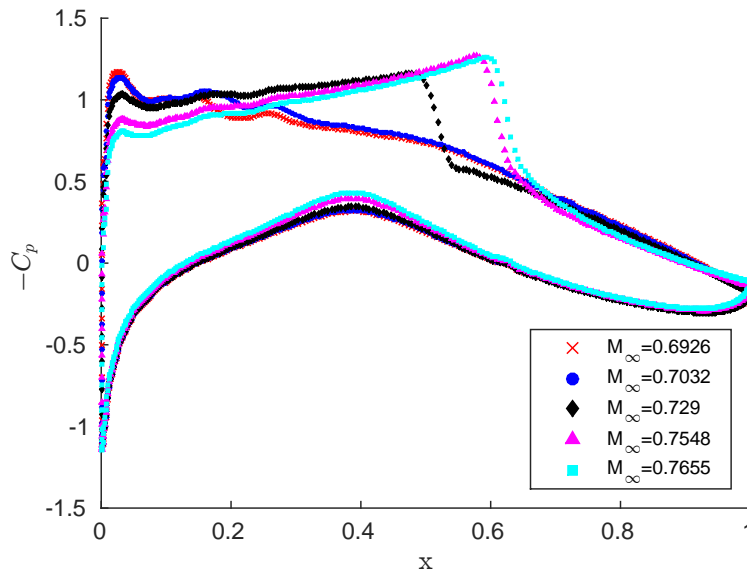


Figure 7.2.3: Deterministic pressure distribution around the surface for 5 different Mach number under the same angle of attack $\alpha = 2.31^\circ$

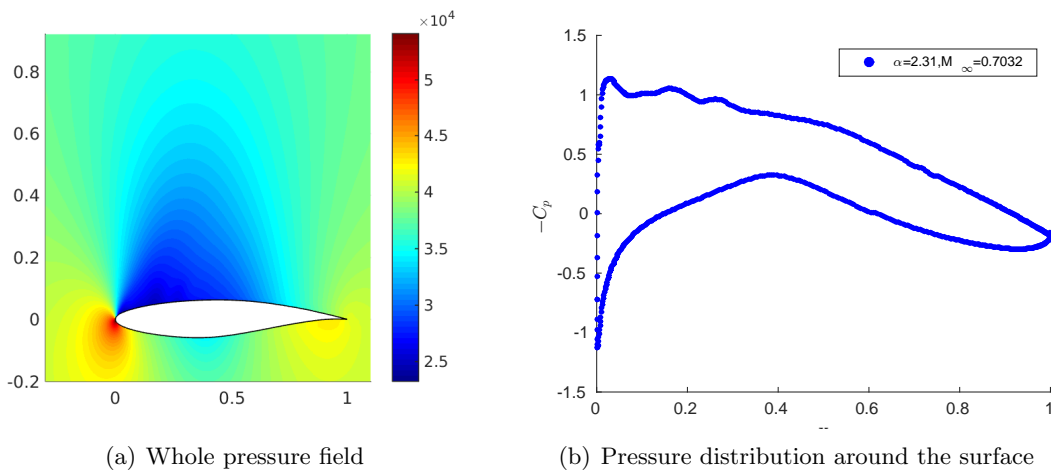


Figure 7.2.4: Deterministic results for $M_\infty = 0.7032$, $\alpha = 2.31^\circ$

For validation of numerical simulation results, the experimental data for case 6 from [11] is used. The comparison of surface pressure distribution is shown in Figure 7.2.2(b), from which we can see that there exists a weak transonic shock wave on the upper surface around $x/c = 0.55$.

To see how the deterministic solutions vary with the uncertain inputs, the pressure distribution of the same angle of attack $\alpha = 2.31^\circ$ and 5 different Mach numbers, which corre-

sponds to the Clenshaw-Curtis sampling nodes, is shown in Figure 7.2.3. For $M_\infty \geq 0.729$, the weak shock wave moves towards the trailing edge with increasing Mach number. Meanwhile, the strength of the shock wave grows. However, for this test case, the weak shock wave disappears for freestream inflow with low Mach number. As shown in Figure 7.2.4(b), the static pressure on the upper surface is recovered in a smooth way.

7.3 Uncertainty propagation results with SC and SC-ENO

In this section, analysis of stochastic flows for beta distribution ($\alpha = 4, \beta = 4$) and uniform distribution are given. Clenshaw-Curtis nodes of level 3 are used for parameter sampling in each dimension of the parameter space and a full tensor product grid is employed.

7.3.1 PDF of C_l , C_d and C_m

We first investigate the influence of the random parameters on the integral value, *i.e.*, the lift, drag and moment coefficient. Results obtained by the SC and SC-ENO are compared with each other.

Combined beta distribution

The probability density function of C_l , C_d and C_m for the propagation of the beta distributed uncertain inflow conditions are given in Figure 7.3.1. Due to the non-linearity of the underlying deterministic model, the symmetric property of the input random parameter is lost.

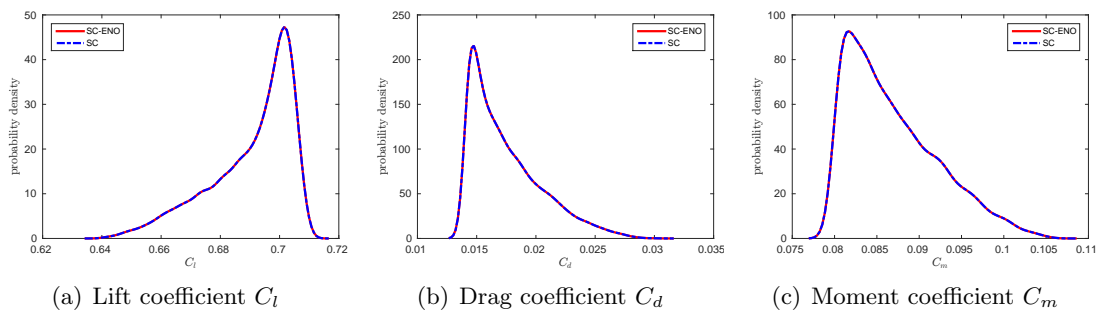


Figure 7.3.1: Probability densities for the beta distribution

The results obtained by SC and SC-ENO exhibit a reasonable agreement due to the smooth nature of these integral quantities, which is manifested in Figure 7.3.2

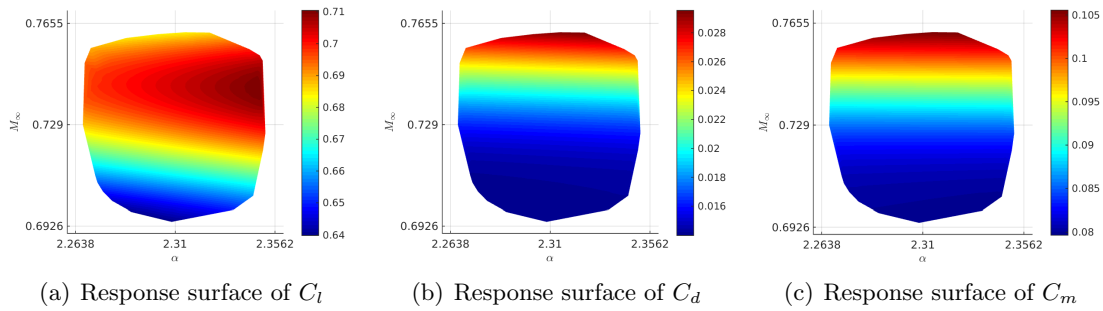


Figure 7.3.2: Response surface for the beta distribution

Combined uniform distribution

The probability density function of C_l , C_d and C_m for the propagation of the uniform distributed uncertain inflow conditions are given in Figure 7.3.3. Similar to the case of beta distribution, the evenly distributed property cannot be preserved through the deterministic solver. However, the influence of the random inputs can still be reflected by the PDF of the outputs, which are more evenly spread compared to the case of the symmetric beta distribution. Again, the results obtained by SC and SC-ENO exhibit a reasonable agreement due to the smooth nature of these integral quantities, which can be seen in Figure 7.3.4

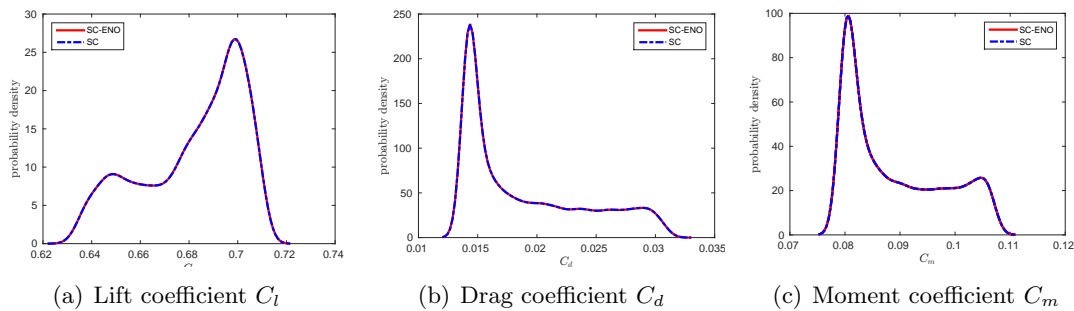


Figure 7.3.3: Probability densities for the uniform distribution

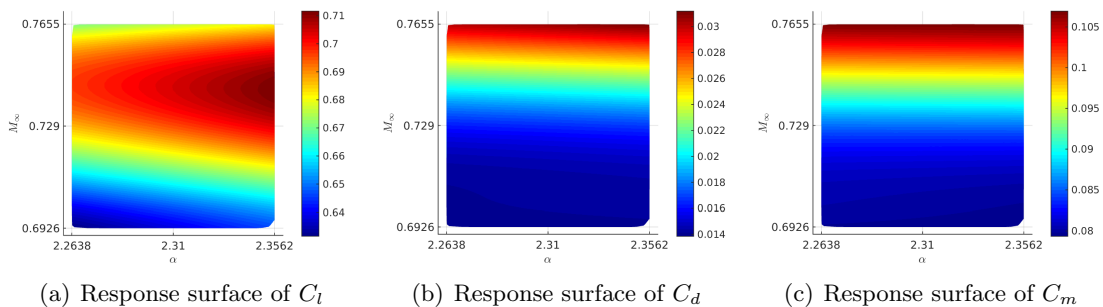


Figure 7.3.4: Response surface for the uniform distribution

7.3.2 Pressure distribution around the airfoil surface

Another quantity of great importance for robust airfoil design and active control of flow field is the pressure distribution around the airfoil. The presence of weak shock wave on the upper surface results in a large variation in the parameter space for a certain physical location, therefore, it is important and necessary to investigate how the pressure distribution varies under the influence of the random inputs. The mesh used around the airfoil has 610 volumes, to each of which the same post-processing, *i.e.*, the non-intrusive uncertainty propagation, is applied. After comparison of different surrogate construction methods, the *least interpolation method* is incorporated into the SC-ENO method since the difference between the least interpolation method and the blocked Lagrange interpolation method is negligible.

Combined beta distribution

The results of post-processing with SC and SC-ENO for the beta distribution are displayed here. The mean surface pressure coefficient $C_p \pm$ standard deviation is shown in Figure 7.3.5. The results obtained by both methods are consistent for the lower surface due to the smooth response surface in the parameter space for each physical location.

However, things are different for the upper surface due to the presence of the shock wave. For a better clarification, the standard deviation on the upper surface is shown in Figure 7.3.6. The traditional SC method overestimates the standard deviation on the upper surface as a result of the Gibbs oscillations around the discontinuities in the parameter space. As mentioned earlier, the oscillations even spread to the smooth region, as demonstrated by the overprediction of standard deviation in the region right after the shock wave, which corresponds to the part $x \in [0.65 - 0.8]$ in Figure 7.3.6.

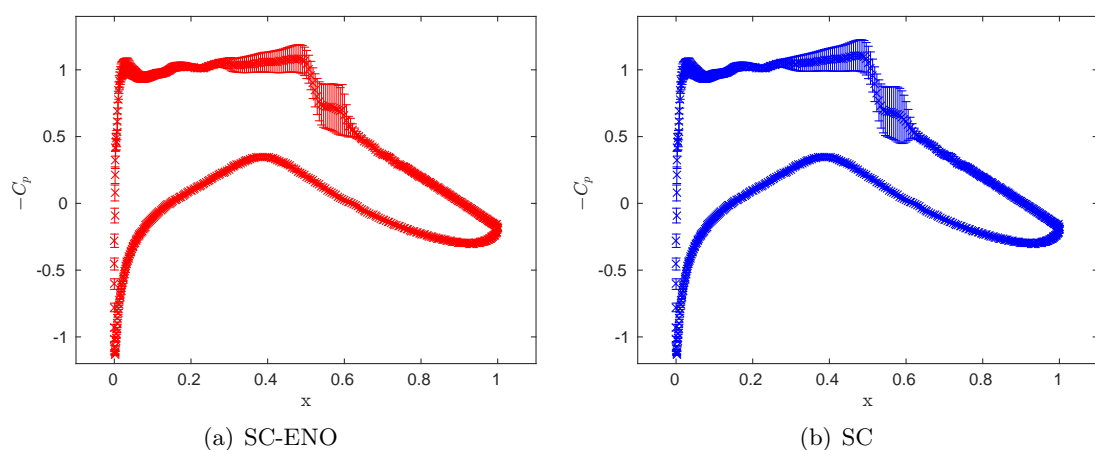


Figure 7.3.5: Mean surface pressure coefficient $C_p \pm$ standard deviation for the beta distribution

By comparison, the Gibbs oscillations in the parameter space are completely eliminated

by the SC-ENO method. Consequently, the values of standard deviation are smaller. This improvement is more necessary if the uncertain bar of full confidence interval is needed for design purpose. The changing location and strength of the shock wave resulting from the uncertain inputs give rise to a dramatic surface pressure variation. Consequently, a large uncertainty bar exists in the shock region, which is shown in Figure 7.3.7. A small undershoot is visible in the shock region for the case of SC. In contrast, the maximum and minimum bounds of pressure distribution obtained by the SC-ENO are completely smooth and follows the same tendency as the mean value. For the ease of visualization of uncertain bar, a sparse version with fewer physical points is displayed in Figure 7.3.8.

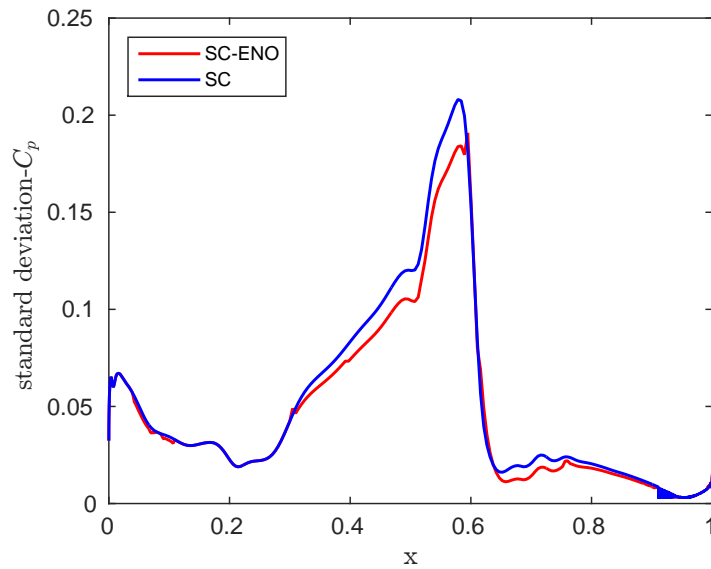


Figure 7.3.6: Standard deviation of upper surface pressure coefficient C_p for the beta distribution

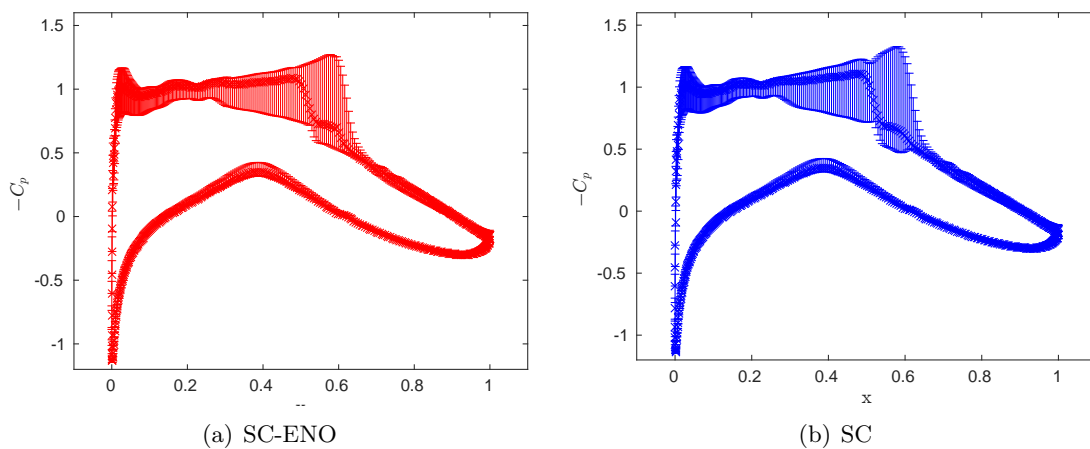


Figure 7.3.7: Mean surface pressure coefficient C_p and full confidence interval for the beta distribution

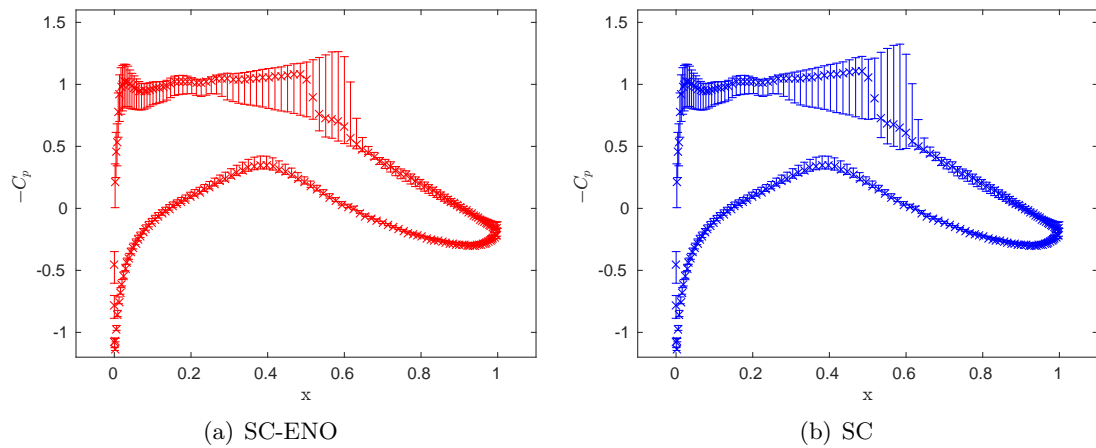


Figure 7.3.8: Mean surface pressure coefficient C_p and full confidence interval for the beta distribution with fewer physical points

Combined uniform distribution

The results for the propagation of the uniform distributed operational uncertainties are remarkably similar to those for the beta distribution. The main difference is that the standard deviation of beta distribution is smaller than the uniform distribution due to the high concentration of the probability in a small region of the parameter space, as we can see from Figure 7.3.11

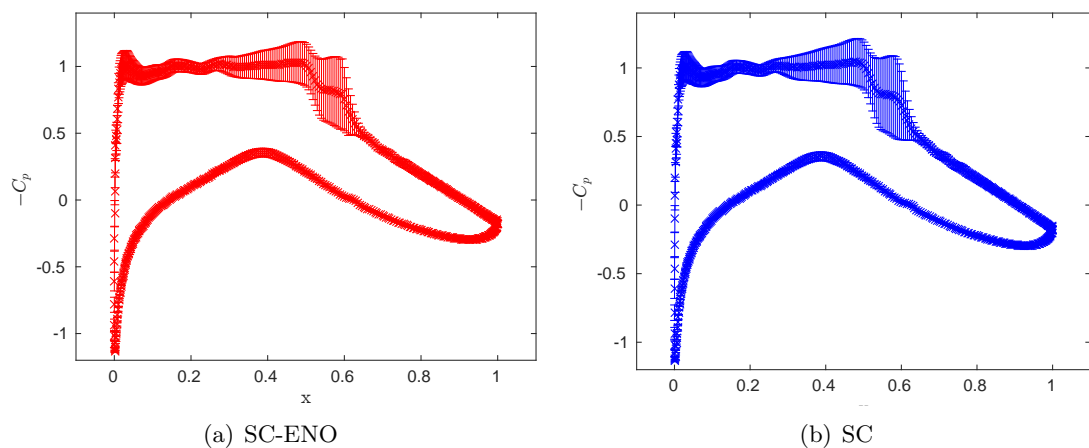


Figure 7.3.9: Mean surface pressure coefficient $C_p \pm$ standard deviation for the uniform distribution

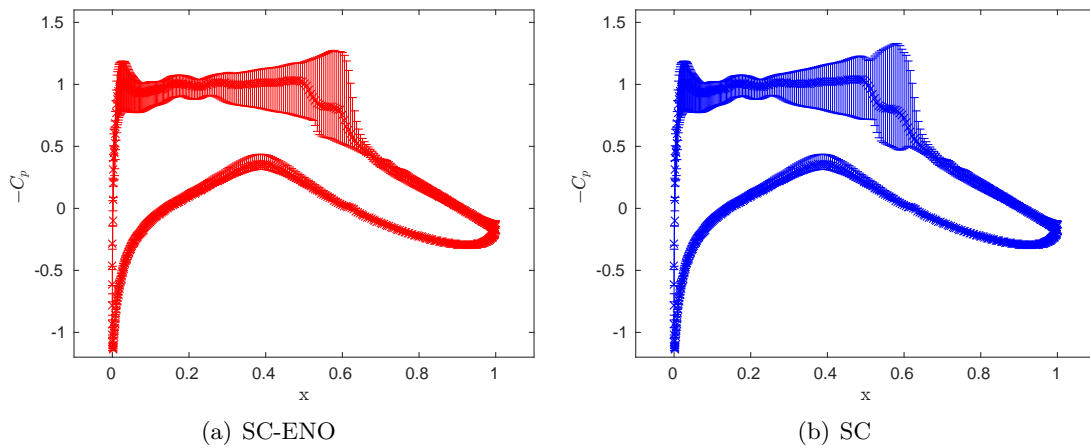


Figure 7.3.10: Mean surface pressure coefficient C_p and full confidence interval for the uniform distribution

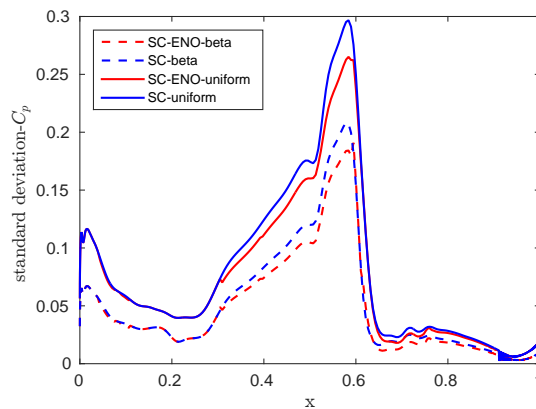


Figure 7.3.11: Standard deviation comparison of the pressure coefficient C_p on the upper surface

Response surface in the parameter space

The different behaviours of SC and SC-ENO methods in terms of the standard deviation and the full confidence interval can be explained if the response surface in the parameter space for a certain physical location is investigated. The physical locations with large standard deviation $x = 0.584$ is picked. In Figure 7.3.12(a), the LEC and MP limiter is enforced to suppress the overshoot around the sharp gradient. It should be noted that although there does not exist a discontinuity in a strict sense, the steep gradient still needs special care for the purpose of robust designs.

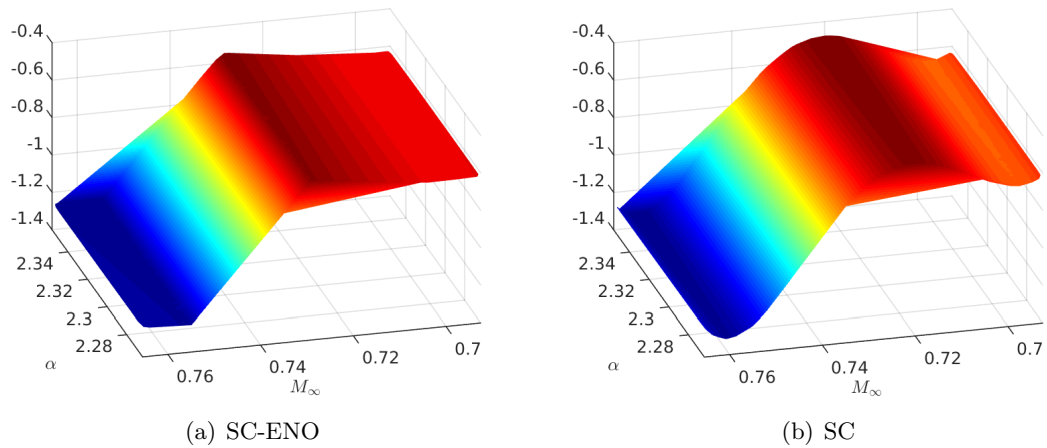
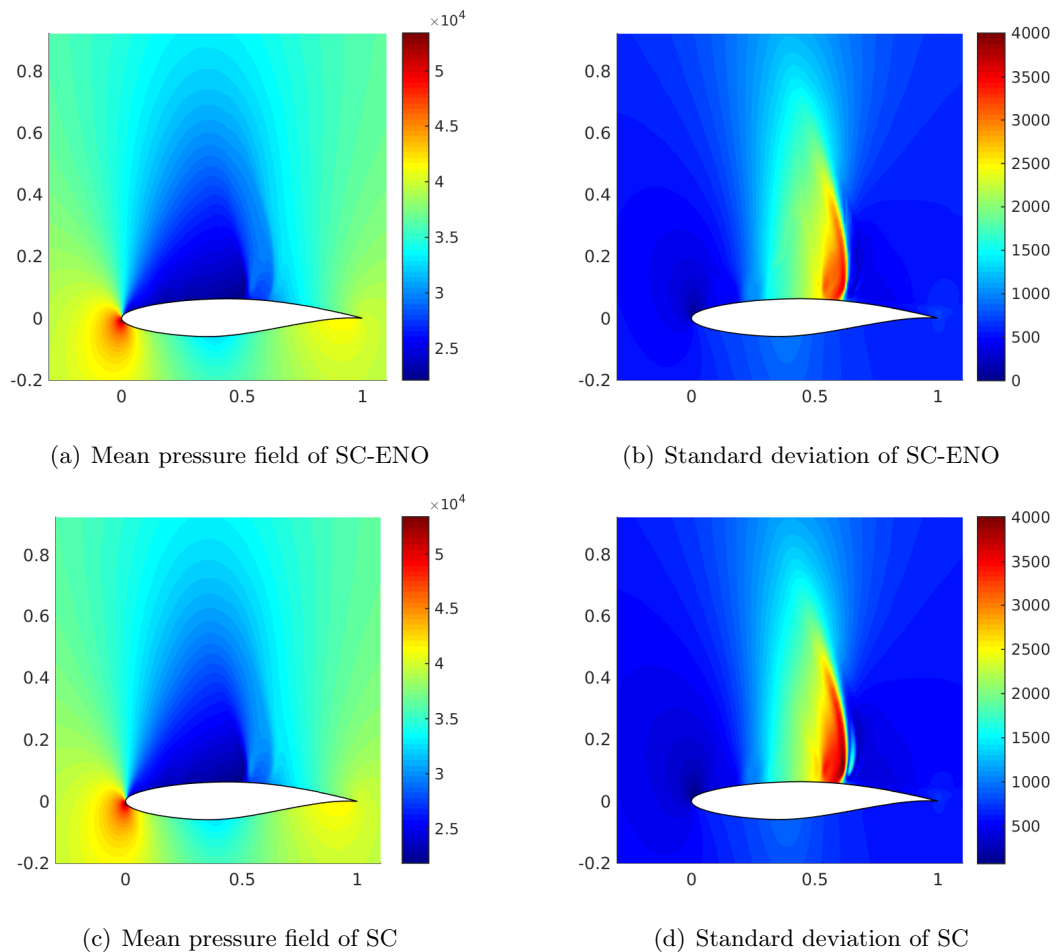
Figure 7.3.12: Response surface in the parameter space for $x = 0.584$.

Figure 7.3.13: Mean and standard deviation of the whole pressure field for the beta distribution

7.3.3 Mean and standard deviation of the whole pressure field

The stochastic analysis for the whole pressure field is presented in this section. The post-processing step is performed for each of the physical points close to the airfoil, which are reduced to 46200. Again, the standard deviation is dominant in the shock region for both of the distributions.

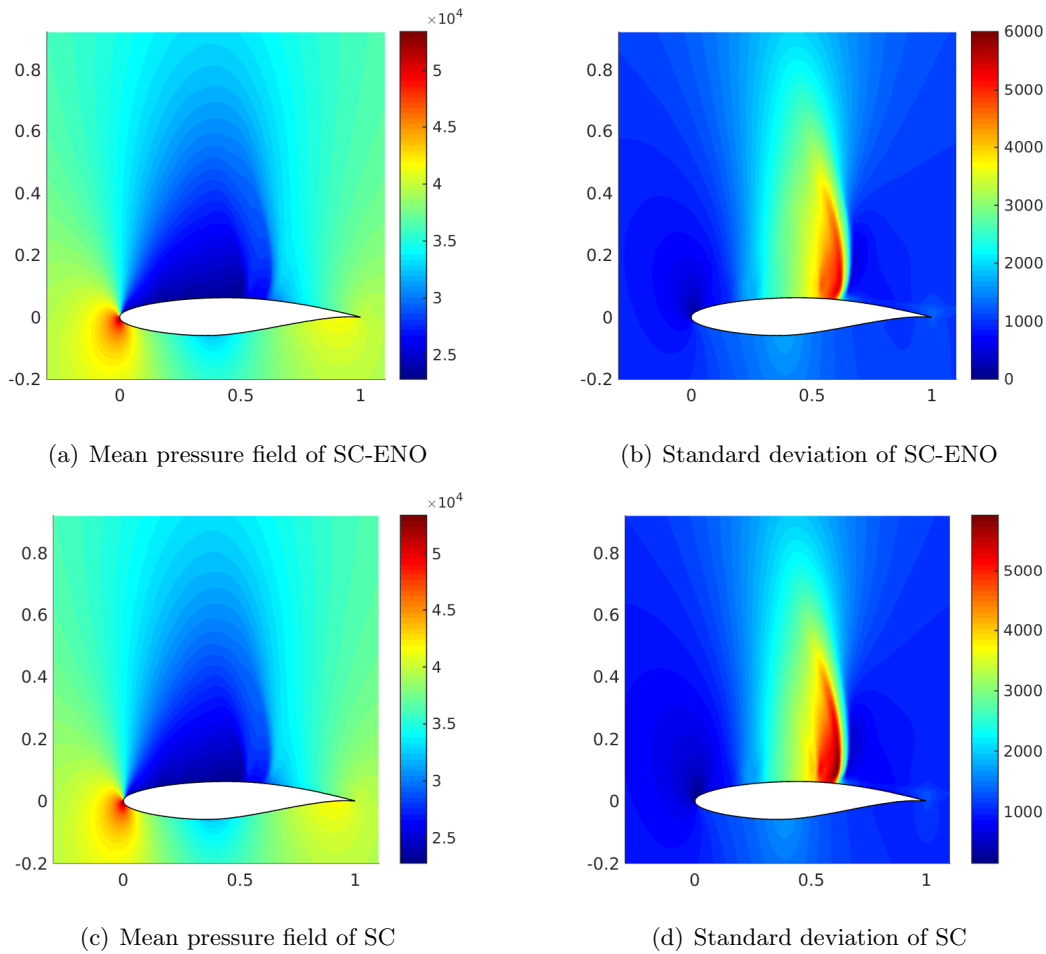


Figure 7.3.14: Mean and standard deviation pressure fields for the uniform distribution

7.4 Uncertainties propagation with the Subcell Resolution (SR) method

In this section, uncertainties propagation results obtained with Subcell Resolution method are presented. Some inherent limitations of the proposed SC-ENO method are discussed first. Then, the application of the Subcell Resolution method to the surface pressure distribution is presented. Finally, the limitations of SR to this test case are discussed.

7.4.1 Staircase approximation of the statistics

The essential idea of the SC-ENO method is to employ piecewise polynomial basis to approximate a discontinuous underlying function. As a result, multi-variate linear interpolation is always used for the discontinuous element bounded by sampling nodes. However, in problems where the discontinuities in the parameter space result from the discontinuities in the physical space, *e.g.*, the test case under consideration, the corresponding random discontinuity locations often result in a staircase approximation of the mean and standard deviation, which can be observed in Figure 7.4.1. Here, the sensitive part of the upper surface is considered. Obviously, this kind of staircase behaviour of the mean value is non-physical. What's more, the convergence rate is reduced to first-order. Meanwhile, standard deviation is underpredicted.

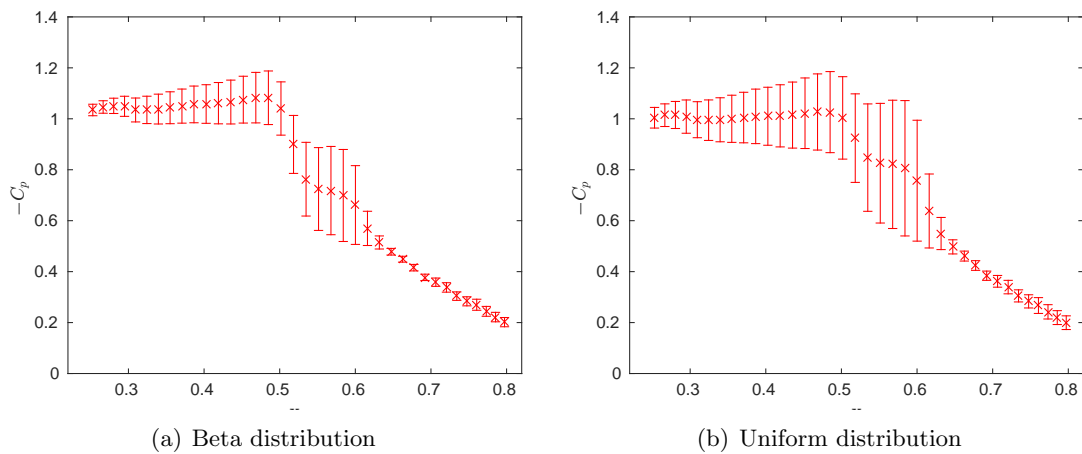


Figure 7.4.1: The mean value and standard deviation of pressure coefficient in the shock region

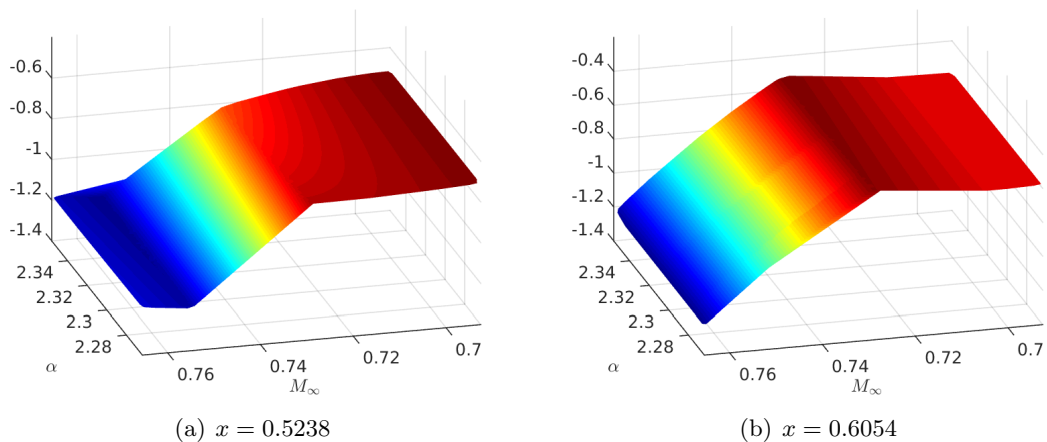


Figure 7.4.2: Response surface in the parameter space with SC-ENO

To explain this, we consider two physical locations $x = 0.5238$ and $x = 0.6054$, which are approximately the starting point and ending point of the staircase approximation in the shock region. The response surfaces in the parameter space are shown in Figure 7.4.2. In this case, the solution does not change much for these two far-apart physical locations, especially for the high gradient region between $M_\infty = 0.729$ and $M_\infty = 0.7548$, where the linear interpolation is always used. It can be imagined that the solutions in the parameter space are more similar for neighbouring physical locations. It should be noted that the staircase behaviour in the statistics is more obvious if the underlying function is strictly discontinuous. To improve the accuracy of the statistics, the subcell resolution method is introduced in the following.

7.4.2 Subcell resolution for the transonic airfoil test case

The implementation of the subcell resolution concept is problem-dependent. For this test case, only a weak discontinuity exists around the upper surface for certain combinations of random parameters due to the viscous boundary layer, which is in contrast to the existing applications to the inviscid solutions around the airfoil in [75].

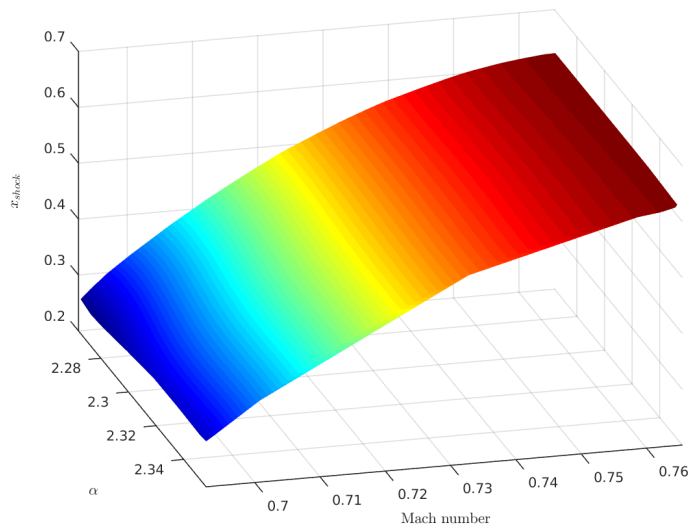
To resolve the location of the discontinuity inside the discontinuous element in the parameter space, the physical shock location x_{shock} along the airfoil is firstly extracted from each of the samples based on the gradient magnitude of the pressure coefficient. Then, to avoid the discrete resolution of the shock location, which is limited to the size of the spatial cell, a parabolic fitting through the maximum gradient point and its two neighbouring spatial points is performed. Consequently, a more accurate shock location is obtained by finding the extremum of that parabolic fit. As shown in Figure 7.2.3, there is no shock wave or even high gradient region of pressure on the upper surface for $M_\infty \leq 0.7032$. Then, the extraction step is spared for those 10 samples.

Subsequently, the extracted physical discontinuity locations x_{shock} are interpolated in the parameter space to obtain an approximation $w_{shock}(\boldsymbol{\xi})$ of the spatial discontinuity location x_{shock} as a function of the random parameters, *i.e.*, the angle of attack and the Mach number. For this test case, the approximation is extrapolated from the parameter space with $M_\infty \geq 0.729$ to the whole parameter space and a monotonic function is obtained, which is shown in Figure 7.4.3.

The locations of the discontinuity in the parameter space for a certain physical location can then be resolved by finding the intersection hypersurface Ξ_{shock} . For each physical location, a corresponding hypersurface Ξ_{shock} is resolved, which is assumed to be the discontinuity in the parameter space. Consequently, the surrogate constructed in each smooth sub-domain can be extended to the predicted locations of the discontinuity.

7.4.3 Response surface in the parameter space with SR

To compare the proposed SC-ENO method with the SR method, the response surface in the parameter space obtained with SR method is shown in Figure 7.4.4 for the previously

Figure 7.4.3: Approximation of x_{shock} in the parameter space

considered physical locations $x = 0.5238$ and $x = 0.6054$, the plots of which are in Figure 7.4.2. With the subcell resolution, the linear interpolation inside the discontinuous element are replaced by the extended interpolation of neighbouring smooth sub-domains from both sides to the predicted discontinuity location ξ_{shock} along the hypersurface Ξ_{shock} .

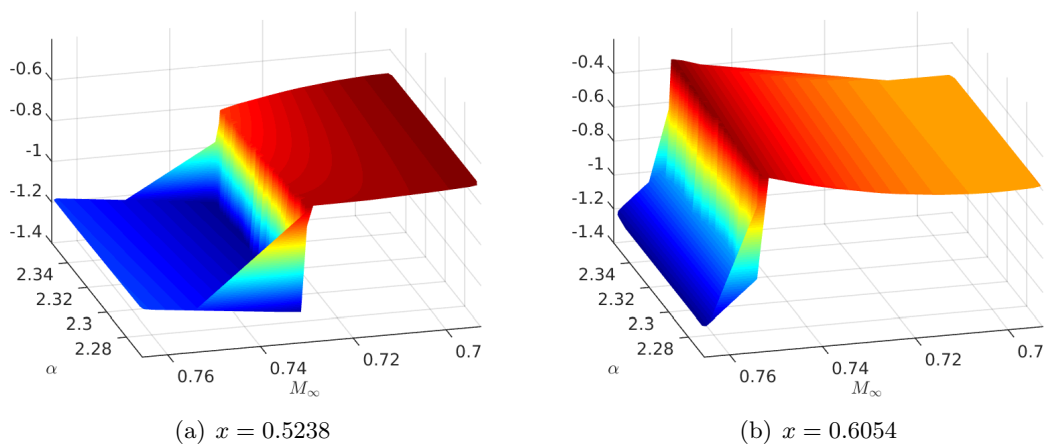


Figure 7.4.4: Response surface in the parameter space with SR

7.4.4 Statistics and full confidence interval obtained with SR

Here, comparisons of the statistics between the SC, SC-ENO and SR methods are made for the sensitive shock region. When it comes to the full confidence interval, the SR and the SC method exhibit similar behaviour, *i.e.*, a larger interval with non-physical overshoots. However, the reasons for that are different. As can be observed in Figure 7.4.4(b), the

overshoots can be explained by the smooth extrapolation inside the discontinuous elements where the limiter is not satisfied any more, which is different from the Gibbs oscillations. Due to the truly discontinuous representation of the sharp gradient enclosed in the discontinuous element, the standard deviation obtained with the SR method is larger than that of the SC-ENO method regardless of the distribution of the random parameter, as shown in Figure 7.4.6 and Figure 7.4.7. This difference of the standard deviation is enlarged if the distribution of the random parameters is concentrated in the parameter space, which is demonstrated in Figure 7.4.8.

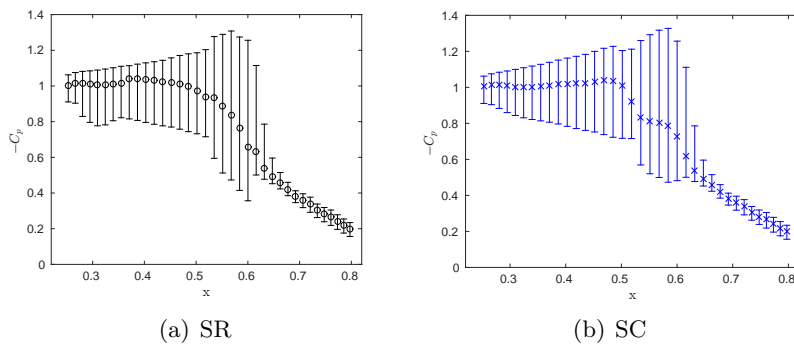


Figure 7.4.5: Mean of the pressure coefficient C_p and full confidence interval for the uniform distribution in the shock region

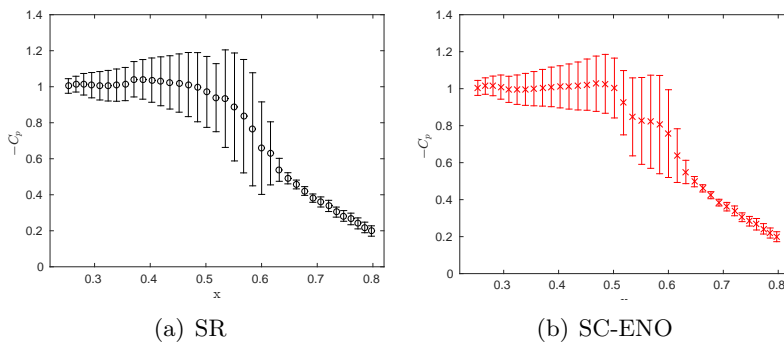


Figure 7.4.6: Mean of the pressure coefficient $C_p \pm$ standard deviation for the uniform distribution in the shock region

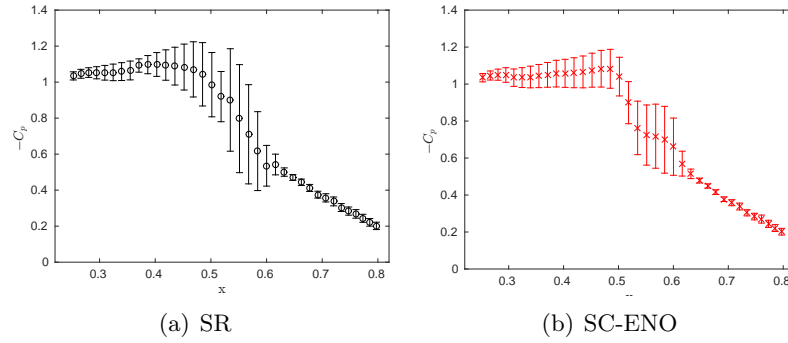


Figure 7.4.7: Mean of the pressure coefficient $C_p \pm$ standard deviation for the beta distribution in the shock region

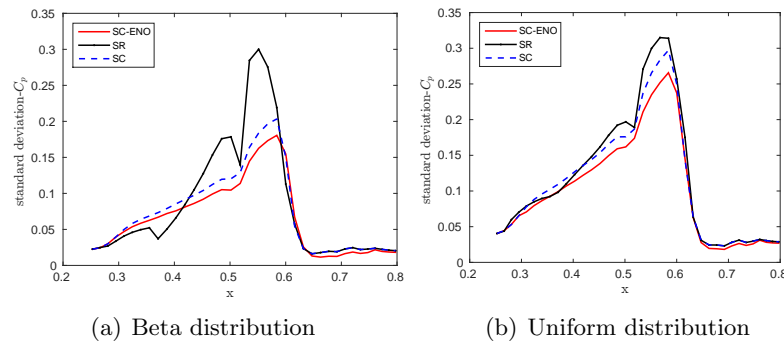


Figure 7.4.8: Comparison of the standard deviation of the pressure coefficient C_p in the shock region

7.4.5 Limitation of the SR method

The SR method is introduced to solve the staircase approximation of the statistics. For this test case, the staircase behaviour of the standard deviation is not obvious due to the smeared shock wave. In terms of the mean value of the pressure coefficient, the SR succeeds to obtain a generally monotonic continuous curve. However, there exist a small overshoot near the end of the shock region, which can be seen in Figure 7.4.7(a). To explain this, the response surfaces of two consecutive physical locations at that region are plotted in Figure 7.4.9.

We can see from the figure that the response surfaces in the parameter space are dramatically different. In both locations, the parameter domain are splitted into two parts. However, the sampling nodes inside each smooth sub-domains is not the same. For the sub-domain associated with the large Mach number, the predicted location of the discontinuity lies between the second and middle sampling nodes in the dimension of the Mach number at $x = 0.6054$, while it lies between the boundary and the second sampling nodes at $x = 0.6108$. Subsequently, two sampling nodes are employed in the Mach number dimension at $x = 0.6054$ while only one sampling node exists $x = 0.6108$. Consequently, a linear interpolation is applied for the Mach number dimension at $x = 0.6054$ while constant approximation is made

$x = 0.6108$. As for the other part of the parameter space, the surrogates constructed show a huge difference as well.

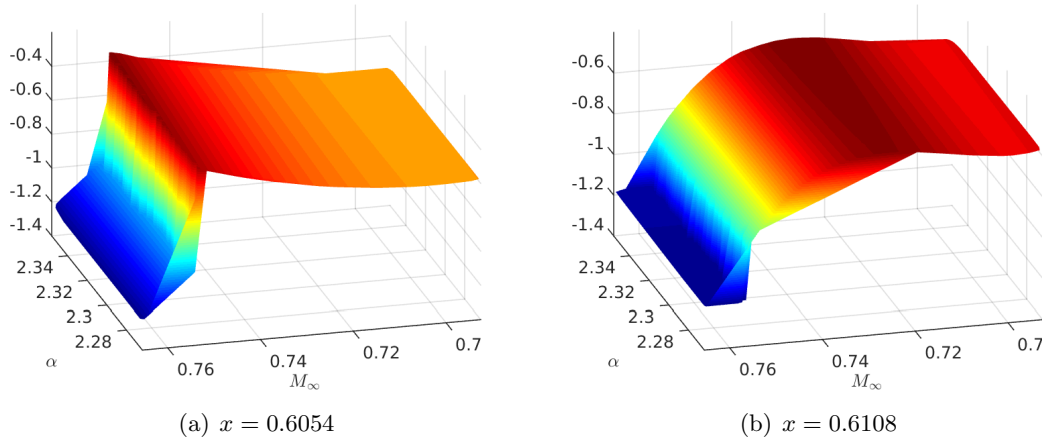


Figure 7.4.9: Response surface in the parameter space with SR near the end of shock region

For this test case, where a full N-S solver is used, the weak shock wave on the upper surface of the airfoil cannot be defined as a discontinuity in the strict sense. Therefore, SR is not suitable compared to the robust SC-ENO method. On the other hand, this test case proves that SC-ENO method is a reliable and robust method for practical problems.

Chapter 8

Conclusions and Recommendations

The main contribution of this thesis is to develop an efficient and robust uncertainty propagation method for underlying functions with discontinuities or steep gradients, especially targeting expensive CFD simulations. To eliminate the stochastic Gibbs oscillations, a complete computational methodology, termed SC-ENO, is proposed and coupled with the dimension adaptive sparse grid approach to alleviate the *curse of dimensionality*. A black box toolkit based on Matlab for the probabilistic uncertainty propagation is developed.

8.1 Conclusions

As we all know, Stochastic Collocation with global basis exhibits fast convergence provided that the underlying function is smooth. However, in most cases, the smoothness of the interested quantities is not known *a priori*. To prevent the Gibbs oscillations inherent with the spectral basis, robustness concepts from the CFD community, *i.e.*, Local Extremum Conserving (LEC), Monotonicity Preserving (MP) and Essentially Non-Oscillatory (ENO), are reformulated for the multi-dimensional stochastic space and incorporated into the Stochastic Collocation method. Different from the existing Simplex Stochastic Collocation (SSC) method, where the simplex tessellation is employed to discretize the stochastic space, the proposed SC-ENO method works on the hypercube discretization where the structured sampling grids are formed by the tensor product of 1-D quadrature nodes. With the prescribed deterministic sampling nodes, the SC-ENO method first locates the discontinuities by enforcing the robust limiter to the surrogate response surface and then constructs the surrogate using the piecewise polynomial basis inside each smooth sub-domain. Due to its non-adaptive nature, the locations of discontinuity can only be resolved up to a resolution of the size of the hypercube elements. As for the surrogate construction, the performance multivariate interpolation methods, *i.e.*, Sauer-Xu Lagrange interpolation and the least interpolation, are compared in terms of the robustness and the accuracy. The least interpolation method is better than Sauer-Xu algorithm but it lacks robustness for certain distribution of the sampling points. To remedy this, a element-wise interpolation method matching the proposed discontinuity detection method is developed.

Like other non-intrusive uncertainty propagation methods, the SC-ENO method can be linked to any deterministic solver to propagate the probabilistic uncertainties. The surrogate model in the stochastic space comes out automatically without the need for parameter manipulations. Generally speaking, it can be viewed as a weighted interpolation method as well as a robust and efficient surrogate construction tool. The most important character of the developed framework lies in its self-adaptation in choosing between the global basis and the local basis based on the smoothness of the constructed surrogate. This is extremely useful when there are more than one quantity of interest (QOI) with different smooth properties since the same set deterministic sampling values can be used. In contrast to the existing adaptive methods designed for the robust approximation of discontinuous function, the SC-ENO is more efficient in terms of the number of deterministic solutions. Besides, the deterministic solvers can be run parallelly.

The performance comparison between the SC-ENO method and the traditional Stochastic Collocation has been demonstrated with respect to some test functions with jumps in function values or derivatives. Robustness against spurious oscillations have been demonstrated. To illustrate its potential for a wider industrial applications, it is first applied to the shock tube problem with uncertainties in initial conditions, whose QOI has a discontinuous response surface in the parameter space. Then, it is applied to the steady flow around the transonic airfoil. For this test case, different QOIs have different smoothness as the functions of the random parameters. The integral value such as the lift coefficient has no jump in the parameter space, where the global basis is desired for the sake of fast convergence. For the same QOI with different smoothness properties at different physical locations, *e.g.*, the static pressure around the airfoil surface, a robust result is obtained with the same set of deterministic sampling values. In both of these test cases, the accuracy, efficiency and robustness of the SC-ENO method are illustrated. It is shown that there are no unphysical overshoots in the full confidence intervals of the interested quantities with sufficient deterministic sampling points. Meanwhile, the performance of another approach dealing with the stochastic discontinuities, *Subcell Resolution* (SR), is investigated. It is concluded that the SC-ENO method is more suitable for the problems with steep gradients whereas the SR approach performs better for the truly discontinuous problems.

8.2 Recommendations and future works

In addition to the need of a robust method to cope with the discontinuous function, there is another challenging research topic in the field of the uncertainty propagation, *i.e.*, *curse of dimensionality*. The proposed SC-ENO method relies on a structured tensor product grid, therefore, it is prone to suffering from the formidable computational costs for problems with high stochastic dimensions. To deal with that, the conventional sparse grid and dimension-adaptive sparse grid are coupled with the SC-ENO method. However, the accuracy of the results is not as good as expected. Based on the experience with the discontinuous test functions, it may be concluded that the conventional sparse grid is not a good choice for discontinuous problems. The combination of the SC-ENO with the existing High-Dimensional Model Representation (HDMR) technique is a future research topic. Another approach to reduce the number of nodes is to perform the sensitivity analysis first, thus identifying the

important dimensions where more deterministic sampling values are supposed to be obtained.

It should be noted that the performance of the SC-ENO method depends largely on the distribution of the sampling nodes. In this thesis work, the Chebyshev extrema nodes are considered with rigorous support from the approximation theory. Besides that, the sampling nodes can be constructed by optimization methods to minimize the error of the interpolant. In that sense, the approach becomes adaptive. Consequently, the multi-dimensional discontinuity detection algorithm, which relies on the tensor product grid, needs to be reformulated.

As shown in the numerical examples of the discontinuous functions, the main interpolation error comes from the linear interpolation applied to the discontinuous elements. To get a more accurate result, it would be beneficial to apply the adaptive grid refinements to the discontinuous elements.

Bibliography

- [1] R. Archibald, A. Gelb, and J. Yoon. Polynomial fitting for edge detection in irregularly sampled signals and images. *SIAM journal on numerical analysis*, 43(1):259–279, 2005.
- [2] M. Arnst and J. P. Ponthot. An overview of nonintrusive characterization, propagation, and sensitivity analysis of uncertainties in computational mechanics. *International Journal for Uncertainty Quantification*, 4(5):387–421, 2014. ISSN 2152-5080.
- [3] R. Askey and J. A. Wilson. *Some basic hypergeometric orthogonal polynomials that generalize Jacobi polynomials*, volume 319. American Mathematical Soc., 1985.
- [4] I. Babuska, R. Tempone, and G. E. Zouraris. Galerkin finite element approximations of stochastic elliptic partial differential equations. *SIAM Journal on Numerical Analysis*, 42(2):800–825, 2004.
- [5] I. Babuška, R. Tempone, and G. E. Zouraris. Solving elliptic boundary value problems with uncertain coefficients by the finite element method: the stochastic formulation. *Computer methods in applied mechanics and engineering*, 194(12):1251–1294, 2005.
- [6] V. Barthelmann, E. Novak, and K. Ritter. High dimensional polynomial interpolation on sparse grids. *Advances in Computational Mathematics*, 12(4):273–288, 2000.
- [7] H.-J. Bungartz and M. Griebel. Sparse grids. *Acta numerica*, 13:147–269, 2004.
- [8] R. H. Cameron and W. T. Martin. The orthogonal development of non-linear functionals in series of Fourier-Hermite functionals. *Annals of Mathematics*, pages 385–392, 1947.
- [9] T. Chantrasmi. *Padé-Legendre method for uncertainty quantification with fluid dynamics applications*. PhD thesis, Stanford University, 2011.
- [10] J.-C. Chassaing and D. Lucor. Stochastic investigation of flows about airfoils at transonic speeds. *AIAA journal*, 48(5):938–950, 2010.
- [11] P. Cook, M. Firmin, and M. McDonald. *Aerofoil RAE 2822 - Pressure Distributions, and Boundary Layer and Wake Measurements*. Experimental Data Base for Computer Program Assessment, AGARD Report AR 138, 1977.
- [12] P. C. Curtis Jr. n-parameter families and best approximation. *Pacific Journal of Mathematics*, pages 1013–1027, 1959.
- [13] C. De Boor. On the error in multivariate polynomial interpolation. *Applied Numerical Mathematics*, 10(3):297–305, 1992.

- [14] C. De Boor. *Gauss elimination by segments and multivariate polynomial interpolation*. Springer, 1994.
- [15] C. De Boor. Polynomial interpolation in several variables. In *Studies in computer science*, pages 87–109. Springer, 1994.
- [16] C. De Boor and A. Ron. On multivariate polynomial interpolation. *Constructive Approximation*, 6(3):287–302, 1990.
- [17] C. De Boor and A. Ron. Computational aspects of polynomial interpolation in several variables. *Mathematics of Computation*, 58(198):705–727, 1992.
- [18] C. De Boor and A. Ron. The least solution for the polynomial interpolation problem. *Mathematische Zeitschrift*, 210(1):347–378, 1992.
- [19] M. K. Deb, I. M. Babuška, and J. T. Oden. Solution of stochastic partial differential equations using galerkin finite element techniques. *Computer Methods in Applied Mechanics and Engineering*, 190(48):6359–6372, 2001.
- [20] W. Edeling. *Quantification of Modelling Uncertainties in Turbulent Flow Simulations*. PhD thesis, TU Delft, Delft University of Technology, 2015.
- [21] G. F. Fasshauer. *Meshfree approximation methods with MATLAB*. World Scientific Publishing Co., Inc., 2007.
- [22] J. Foo, X. Wan, and G. E. Karniadakis. The multi-element probabilistic collocation method (ME-PCM): error analysis and applications. *Journal of Computational Physics*, 227(22):9572–9595, 2008.
- [23] M. Gasca and T. Sauer. Polynomial interpolation in several variables. *Advances in Computational Mathematics*, 12(4):377–410, 2000.
- [24] A. Genz. A package for testing multiple integration subroutines. *Numerical Integration*, pages 337–340, 1987.
- [25] M. Gerritsma, J.-B. Van der Steen, P. Vos, and G. Karniadakis. Time-dependent generalized polynomial chaos. *Journal of Computational Physics*, 229(22):8333–8363, 2010.
- [26] T. Gerstner and M. Griebel. Dimension-adaptive tensor-product quadrature. *Computing*, 71(1):65–87, 2003.
- [27] R. G. Ghanem and P. D. Spanos. *Stochastic finite elements: a spectral approach*, volume 387974563. Springer.
- [28] A. Gorodetsky and Y. Marzouk. Efficient localization of discontinuities in complex computational simulations. *SIAM Journal on Scientific Computing*, 36(6):A2584–A2610, 2014.
- [29] D. Gottlieb and C.-W. Shu. On the gibbs phenomenon and its resolution. *SIAM review*, 39(4):644–668, 1997.
- [30] S. Gottlieb, J.-H. Jung, and S. Kim. A review of david gottlieb’s work on the resolution of the gibbs phenomenon. *Communications in Computational Physics*, 9(3):497–519, 2011.

- [31] M. Griebel. *Sparse grids and related approximation schemes for higher dimensional problems*. SFB 611, 2005.
- [32] A. Harten. ENO schemes with subcell resolution. *Journal of Computational Physics*, 83(1):148 – 184, 1989.
- [33] A. Harten, B. Engquist, S. Osher, and S. R. Chakravarthy. Uniformly high order accurate essentially non-oscillatory schemes, iii. *Journal of computational physics*, 71(2): 231–303, 1987.
- [34] J. C. Helton and F. J. Davis. Latin hypercube sampling and the propagation of uncertainty in analyses of complex systems. *Reliability Engineering & System Safety*, 81(1): 23–69, 2003.
- [35] S. Hosder, R. W. Walters, and M. Balch. Efficient sampling for non-intrusive polynomial chaos applications with multiple uncertain input variables. In *Proceedings of the 48th AIAA/ASME/ASCE/AHS/ASC Structures, Structural Dynamics and Materials Conference, AIAA paper*, volume 1939, 2007.
- [36] G. Iaccarino. Uncertainty quantification in computational fluid dynamics. STO-AVT-VKI Lecture Series-AVT 235, 2014.
- [37] J. D. Jakeman, R. Archibald, and D. Xiu. Characterization of discontinuities in high-dimensional stochastic problems on adaptive sparse grids. *Journal of Computational Physics*, 230(10):3977–3997, 2011.
- [38] J. D. Jakeman, A. Narayan, and D. Xiu. Minimal multi-element stochastic collocation for uncertainty quantification of discontinuous functions. *Journal of Computational Physics*, 242:790–808, 2013.
- [39] P. Kergin. A natural interpolation of c functions. *Journal of Approximation Theory*, 29(4):278–293, 1980.
- [40] A. Klimke. Sparse Grid Interpolation Toolbox – user’s guide. Technical Report IANS report 2007/017, University of Stuttgart, 2007.
- [41] A. Klimke and B. Wohlmuth. Algorithm 847: Spinterp: piecewise multilinear hierarchical sparse grid interpolation in matlab. *ACM Transactions on Mathematical Software (TOMS)*, 31(4):561–579, 2005.
- [42] A. Klimke and B. Wohlmuth. Constructing dimension-adaptive sparse grid interpolants using parallel function evaluations. *Parallel processing letters*, 16(04):407–418, 2006.
- [43] O. P. Le Maître and O. M. Knio. *Spectral methods for uncertainty quantification: with applications to computational fluid dynamics*. Springer, 2010.
- [44] O. P. Le Maître, O. M. Knio, H. N. Najm, and R. G. Ghanem. Uncertainty propagation using Wiener–Haar expansions. *Journal of Computational Physics*, 197(1):28–57, 2004.
- [45] O. P. Le Maître, H. N. Najm, R. G. Ghanem, and O. M. Knio. Multi-resolution analysis of Wiener-type uncertainty propagation schemes. *Journal of Computational Physics*, 197(2):502–531, 2004.

- [46] A. Loeven, J. A. S. Witteveen, and H. Bijl. Probabilistic collocation: an efficient non-intrusive approach for arbitrarily distributed parametric uncertainties. In *Proceedings of the 45th AIAA Aerospace Sciences Meeting and Exhibit, AIAA paper*, volume 317, 2007.
- [47] D. Lucor, J. Witteveen, P. Constantine, D. Schiavazzi, and G. Iaccarino. Comparison of adaptive uncertainty quantification approaches for shock wave-dominated flows. In *Proceedings of the Summer Program*, page 219, 2012.
- [48] X. Ma and N. Zabarar. An adaptive hierarchical sparse grid collocation algorithm for the solution of stochastic differential equations. *Journal of Computational Physics*, 228(8):3084–3113, 2009.
- [49] X. Ma and N. Zabarar. An adaptive high-dimensional stochastic model representation technique for the solution of stochastic partial differential equations. *Journal of Computational Physics*, 229(10):3884–3915, 2010.
- [50] J. C. Mairhuber. On haar’s theorem concerning chebychev approximation problems having unique solutions. *Proceedings of the American Mathematical Society*, 7(4):609–615, 1956.
- [51] L. Mathelin and M. Y. Hussaini. A stochastic collocation algorithm for uncertainty analysis. Technical report, NASA Langley Research Center, 2003.
- [52] M. D. McKay, R. J. Beckman, and W. J. Conover. Comparison of three methods for selecting values of input variables in the analysis of output from a computer code. *Technometrics*, 21(2):239–245, 1979.
- [53] A. Narayan and D. Xiu. Stochastic collocation methods on unstructured grids in high dimensions via interpolation. *SIAM Journal on Scientific Computing*, 34(3):A1729–A1752, 2012.
- [54] F. Nobile, R. Tempone, and C. G. Webster. An anisotropic sparse grid stochastic collocation method for partial differential equations with random input data. *SIAM Journal on Numerical Analysis*, 46(5):2411–2442, 2008.
- [55] F. Nobile, R. Tempone, and C. G. Webster. A sparse grid stochastic collocation method for partial differential equations with random input data. *SIAM Journal on Numerical Analysis*, 46(5):2309–2345, 2008.
- [56] G. Poëtte and D. Lucor. Non intrusive iterative stochastic spectral representation with application to compressible gas dynamics. *Journal of Computational Physics*, 231(9):3587–3609, 2012.
- [57] M. T. Reagana, H. N. Najm, R. G. Ghanem, and O. M. Knio. Uncertainty quantification in reacting-flow simulations through non-intrusive spectral projection. *Combustion and Flame*, 132(3):545–555, 2003.
- [58] T. Sauer. Lagrange interpolation on subgrids of tensor product grids. *Mathematics of Computation*, 73(245):181–190, 2004.
- [59] T. Sauer and Y. Xu. On multivariate lagrange interpolation. *Mathematics of Computation*, 64(211):1147–1170, 1995.

- [60] C.-W. Shu. *Essentially non-oscillatory and weighted essentially non-oscillatory schemes for hyperbolic conservation laws*. Springer, 1998.
- [61] S. A. Smolyak. Quadrature and interpolation formulas for tensor products of certain classes of functions. In *Dokl. Akad. Nauk SSSR*, volume 4, page 123, 1963.
- [62] A. Suresh and H. Huynh. Accurate monotonicity-preserving schemes with runge–kutta time stepping. *Journal of Computational Physics*, 136(1):83–99, 1997.
- [63] L. N. Trefethen. Is Gauss quadrature better than Clenshaw-Curtis? *SIAM review*, 50(1):67–87, 2008.
- [64] L. N. Trefethen. *Approximation theory and approximation practice*. Siam, 2013.
- [65] X. Wan and G. E. Karniadakis. An adaptive multi-element generalized polynomial chaos method for stochastic differential equations. *Journal of Computational Physics*, 209(2):617–642, 2005.
- [66] X. Wan and G. E. Karniadakis. Multi-element generalized polynomial chaos for arbitrary probability measures. *SIAM Journal on Scientific Computing*, 28(3):901–928, 2006.
- [67] G. W. Wasilkowski and H. Wozniakowski. Explicit cost bounds of algorithms for multivariate tensor product problems. *Journal of Complexity*, 11(1):1–56, 1995.
- [68] N. Wiener. The Homogeneous Chaos. *American Journal of Mathematics*, 60(4):pp. 897–936, 1938. ISSN 00029327.
- [69] J. A. Witteveen. Second order front tracking for the euler equations. *Journal of Computational Physics*, 229(7):2719–2739, 2010.
- [70] J. A. Witteveen, A. Doostan, T. Chantrasmi, R. Pecnik, and G. Iaccarino. Comparison of stochastic collocation methods for uncertainty quantification of the transonic rae 2822 airfoil. In *Proceedings of workshop on quantification of CFD uncertainties*, 2009.
- [71] J. A. S. Witteveen and H. Bijl. Modeling arbitrary uncertainties using gram-schmidt polynomial chaos. In *Proceedings of the 44th AIAA Aerospace Sciences Meeting and Exhibit, number AIAA-2006-0896, Reno, NV*, volume 117, 2006.
- [72] J. A. S. Witteveen and G. Iaccarino. Refinement criteria for simplex stochastic collocation with local extremum diminishing robustness. *SIAM Journal on Scientific Computing*, 34(3):A1522–A1543, 2012.
- [73] J. A. S. Witteveen and G. Iaccarino. Simplex stochastic collocation with random sampling and extrapolation for nonhypercube probability spaces. *SIAM Journal on Scientific Computing*, 34(2):A814–A838, 2012.
- [74] J. A. S. Witteveen and G. Iaccarino. Simplex stochastic collocation with ENO-type stencil selection for robust uncertainty quantification. *Journal of Computational Physics*, 239:1–21, 2013.
- [75] J. A. S. Witteveen and G. Iaccarino. Subcell resolution in simplex stochastic collocation for spatial discontinuities. *Journal of Computational Physics*, 251:17–52, 2013.

- [76] J. A. S. Witteveen and G. Iaccarino. Uncertainty propagation with monotonicity preserving robustness. 2014.
- [77] J. A. S. Witteveen, B. Koren, and P. G. Bakker. An improved front tracking method for the euler equations. *Journal of Computational Physics*, 224(2):712–728, 2007.
- [78] J. A. S. Witteveen, A. Loeven, and H. Bijl. An adaptive stochastic finite elements approach based on newton–cotes quadrature in simplex elements. *Computers & Fluids*, 38(6):1270–1288, 2009.
- [79] D. Xiu. Efficient collocational approach for parametric uncertainty analysis. *Communications in computational physics*, 2(2):293–309, 2007.
- [80] D. Xiu. *Numerical methods for stochastic computations: a spectral method approach*. Princeton University Press, 2010.
- [81] D. Xiu and G. Em Karniadakis. Modeling uncertainty in steady state diffusion problems via generalized polynomial chaos. *Computer Methods in Applied Mechanics and Engineering*, 191(43):4927–4948, 2002.
- [82] D. Xiu and J. S. Hesthaven. High-order collocation methods for differential equations with random inputs. *SIAM Journal on Scientific Computing*, 27(3):1118–1139, 2005.
- [83] D. Xiu and G. E. Karniadakis. The Wiener-Askey polynomial chaos for stochastic differential equations. *SIAM Journal on Scientific Computing*, 24(2):619–644, 2002.
- [84] D. Xiu and G. E. Karniadakis. Modeling uncertainty in flow simulations via generalized polynomial chaos. *Journal of computational physics*, 187(1):137–167, 2003.
- [85] D. Xiu and G. E. Karniadakis. A new stochastic approach to transient heat conduction modeling with uncertainty. *International Journal of Heat and Mass Transfer*, 46(24):4681–4693, 2003.

Appendix A

The original Wiener polynomial chaos

Let $\{\xi_j(\omega)\}_{j=1}^{\infty}$ be a set of independent standard Gaussian random variables, ω is the sample event. $L_2(\Omega, \mathcal{P})$ is the space of second order random variables ξ defined on $(\Omega, \mathcal{A}, \mathcal{P})$. Let $\hat{\Gamma}_p$ denote the space of all polynomials in $\{\xi_j(\omega)\}_{j=1}^{\infty}$ of degree not exceeding p ; Γ_p represent the set of polynomials in $\hat{\Gamma}_p$ orthogonal to $\hat{\Gamma}_{p-1}$; $\bar{\Gamma}_p$ be the space spanned by Γ_p . We have [43]

$$\hat{\Gamma}_p = \hat{\Gamma}_{p-1} \oplus \bar{\Gamma}_p, \quad L_2(\Omega, \mathcal{P}) = \bigoplus_{i=0}^{\infty} \bar{\Gamma}_i. \quad (\text{A.1})$$

Then, the subspace $\bar{\Gamma}_p$ of $L_2(\Omega, \mathcal{P})$ is called the p -th *Homogeneous Chaos*, and Γ_p is called the *Polynomial Chaos* of order p [68]. As indicated in [8], any second-order random process U , as a function of random event ω , can be represented in the form:

$$\begin{aligned} U(\omega) = & a_0 \Gamma_0 + \sum_{i_1=1}^{\infty} a_{i_1} \Gamma_1(\xi_{i_1}(\omega)) \\ & + \sum_{i_1=1}^{\infty} \sum_{i_2=1}^{i_1} a_{i_1 i_2} \Gamma_2(\xi_{i_1}(\omega), \xi_{i_2}(\omega)) \\ & + \sum_{i_1=1}^{\infty} \sum_{i_2=1}^{i_1} \sum_{i_3=1}^{i_2} a_{i_1 i_2 i_3} \Gamma_3(\xi_{i_1}(\omega), \xi_{i_2}(\omega), \xi_{i_3}(\omega)) \\ & + \dots, \end{aligned} \quad (\text{A.2})$$

where $\Gamma_p(\xi_{i_1}(\omega), \dots, \xi_{i_p}(\omega))$ denotes the Hermite Polynomial Chaos of order p in terms of the variables $(\xi_{i_1}(\omega), \dots, \xi_{i_p}(\omega))$. This expansion is convergent in the mean-square sense as a result of Cameron-Martin theorem [8]. Such L^2 *strong convergence* implies convergence in probability, and further convergence in distribution. We can also observe from the above expansion that the Polynomial Chaos of order p consist of all orthogonal polynomials of order p with all kinds of combinations of random variables $\{\xi_j(\omega)\}_{j=1}^{\infty}$. An intrinsic property of Polynomials Chaos is that they are orthogonal to each other when they are either of different order or with a different argument list. Consequently, the Polynomial Chaos of order greater than one have vanishing mean.

For the computational purpose, the construction above that involves infinite dimension

should be reduced to a finite dimensional Polynomial Chaos. In this case, the infinite upper limit on the summations in (A.2) is replaced by a number equal to the number of independent random variables ξ_i . For instance, an expansion with two dimensions becomes:

$$\begin{aligned}
U(\omega) &= a_0\Gamma_0 + \sum_{i_1=1}^2 a_{i_1}\Gamma_1(\xi_{i_1}(\omega)) \\
&+ \sum_{i_1=1}^2 \sum_{i_2=1}^{i_1} a_{i_1 i_2}\Gamma_2(\xi_{i_1}(\omega), \xi_{i_2}(\omega)) \\
&+ \sum_{i_1=1}^2 \sum_{i_2=1}^{i_1} \sum_{i_3=1}^{i_2} a_{i_1 i_2 i_3}\Gamma_3(\xi_{i_1}(\omega), \xi_{i_2}(\omega), \xi_{i_3}(\omega)) \\
&+ \cdots .
\end{aligned} \tag{A.3}$$

If we use ξ_1 and ξ_2 to denote these two random variables, (A.3) becomes:

$$\begin{aligned}
U(\omega) &= a_0\Gamma_0 + a_1\Gamma_1(\xi_1(\omega)) + a_2\Gamma_1(\xi_2(\omega)) \\
&+ a_{11}\Gamma_2(\xi_1(\omega), \xi_1(\omega)) + a_{12}\Gamma_2(\xi_1(\omega), \xi_2(\omega)) + a_{22}\Gamma_2(\xi_2(\omega), \xi_2(\omega)) \\
&+ a_{111}\Gamma_3(\xi_1(\omega), \xi_1(\omega), \xi_1(\omega)) + a_{211}\Gamma_3(\xi_2(\omega), \xi_1(\omega), \xi_1(\omega)) + a_{221}\Gamma_3(\xi_2(\omega), \xi_2(\omega), \xi_1(\omega)) \\
&+ a_{222}\Gamma_3(\xi_2(\omega), \xi_2(\omega), \xi_2(\omega)) + \cdots .
\end{aligned} \tag{A.4}$$

Appendix B

Algorithm of the multivariate Lagrange interpolation

In this chapter, the pseudo code of the multivariate Lagrange interpolation algorithm is reproduced from [59].

Let $\alpha_1^n, \dots, \alpha_{r_n^d}^n$ be the multi-indices ¹ of a certain order n , with $|\alpha| = n$ and $r_n^d = \binom{d+n-1}{n}$. Also, these multi-indices are arranged in a certain order, *e.g.*, lexicographical order. For convenience and without misunderstanding, we denote ordering $\alpha_1^1, \alpha_1^2, \dots, \alpha_d^2, \dots, \alpha_1^n, \dots, \alpha_{r_n^d}^n$ by $\alpha_1, \dots, \alpha_S$.

¹These multi-indices are actually the exponents of monomial basis

Algorithm 3 Lagrange interpolation algorithm [59]

Input: Scattered data $\Theta_d = \{x_1, \dots, x_S\}$ in d -dimensional space

Initialization:

$M := N;$

for $k = 1 : S$ **do**

$Q_k := x^{\alpha_k}$ \triangleright Multi-indices are prescribed in a certain order based on total degree

end for

Inductive process:

for $k = 1 : S$ **do**

$i := \min(\{k \leq j \leq M : Q_j(x_k) \neq 0\} \cup \{M + 1\})$

while $i = M + 1$ **do**

for $j = 1 : 1 : r_{n+1}^d$ **do**

$Q_{S+j}(x) = x^{\alpha_j^{n+1}} - \sum_{l=1}^k x_l^{\alpha_j^{n+1}} P_l(x);$

end for

$M := \dim \Pi_{n+1}^d;$

$n + 1;$

$i := \min(\{k \leq j \leq M : Q_j(x_k) \neq 0\} \cup \{M + 1\});$

end while

$P_k(x) := \frac{Q_i(x)}{Q_i(x_k)};$

for $j = 1 : 1 : k - 1$ **do**

$P_j(x) = P_j(x) - P_j(x_k)P_k(x);$

end for

for $j = i - 1 : k + 1$ **do**

$Q_j(x) = Q_{j-1}(x) - Q_{j-1}(x_k)P_k(x);$

end for

for $j = i + 1 : 1 : S$ **do**

$Q_j(x) = Q_j(x) - Q_j(x_k)P_k(x);$

end for

end for

Output: $P_1, \dots, P_S \in \Pi_n^d$ are the Lagrange polynomial basis satisfying $P_i(x_j) = \delta_{ij}, i, j = 1, \dots, S$

Appendix C

Construction of the least interpolant by Gauss elimination

First, a proof of the proposition 4.3.2 is presented. The proposition is restated as follows:

Proposition C.0.1. [17] *The polynomial interpolant in the form*

$$\mathcal{I}_\Theta f := \sum_{j=1}^S g_{j\downarrow} \frac{\langle g_j, f \rangle}{\langle g_j, g_{j\downarrow} \rangle} \quad (\text{C.1})$$

is the unique interpolant satisfying $\mathcal{I}_\Theta f = f$ on Θ , with g_1, g_2, \dots, g_S a basis for \exp_Θ (particularly, $S = \#\Theta$) and

$$\langle g_i, g_{j\downarrow} \rangle = 0 \iff i \neq j. \quad (\text{C.2})$$

In the following, the proof of the above proposition is given based on [17]:

Proof. First, let us recall the pairing:

$$\langle g, f \rangle := \sum_{\alpha} D^\alpha g(0) D^\alpha f(0) / \alpha!, \quad g, f \in \Pi. \quad (\text{C.3})$$

and the polynomial evaluation $f(\theta)$ in terms of the pairing with respect to the exponential e_θ , i.e.,

$$\langle e_\theta, f \rangle = \sum_{\alpha} D^\alpha e_\theta(0) D^\alpha f(0) / \alpha! = f(\theta), \quad (\text{C.4})$$

The equation (C.4) can be extended to pairing of arbitrary $g \in \exp_\Theta$ and $f \in C(\mathbb{R}^d)$ by

$$\left\langle \sum_{\alpha \in \Theta} w(\alpha) e_\alpha, f \right\rangle = \sum_{\alpha \in \Theta} w(\alpha) f(\alpha), \quad f \in C \quad (\text{C.5})$$

Consequently,

$$\sum_i w(i) g_i = e_\theta \Rightarrow \sum_i w(i) \langle g_i, f \rangle = f(\theta), \quad f \in C \quad (\text{C.6})$$

From (C.1) and (C.2), it follows that

$$\langle g_i, \mathcal{I}_\Theta f \rangle = \langle g_i, f \rangle, \quad \text{all } i. \quad (\text{C.7})$$

Since g_1, g_2, \dots, g_S is a basis for exp_Θ and (C.4) (C.6), it implies that

$$\mathcal{I}_\Theta f(\theta) = \langle e_\theta, \mathcal{I}_\Theta f \rangle = \left\langle \sum_i w(i)g_i, \mathcal{I}_\Theta f \right\rangle = \sum_i w(i)\langle g_i, f \rangle = f(\theta), \quad \theta \in \Theta. \quad (\text{C.8})$$

□

In the following, a detailed discussion of Gauss elimination with partial row pivoting is given. It should be remarked that most of the following descriptions are taken from [17]. More details are added based on the knowledge and understanding of the author. A little typo from the original paper is corrected.

We consider the matrix

$$\mathbf{V} := (\theta^\alpha)_{\theta \in \Theta, \alpha \in \mathbb{N}^d}, \quad (\text{C.9})$$

which is obtained from the Vandermonde matrix $V = (\theta^\alpha)$ by treating all entries of a given degree as one entry. From here on, boldface letters indicate vector quantities. The rows of \mathbf{V} are indexed by $\theta \in \Theta$ as before, but its columns are indexed by degree by degree instead of term by term. Hence,

$$(\theta^k) = (\theta^\alpha)_{|\alpha|=k}, \quad k = 0, 1, 2, \dots$$

Here, the term *Gauss elimination* takes a new meaning since we cannot ‘eliminate entries’ as what we did for entries of numbers any more. Rather, the entries of \mathbf{V} are vectors, so we can only make all the entries in the pivot column below the pivot row **orthogonal** to the pivot entry. When eliminating in column k of \mathbf{V} , the inner product

$$\langle a, b \rangle_k := \sum_{|\alpha|=k} a(\alpha)b(\alpha)/\alpha! \quad (\text{C.10})$$

is defined, which is consistent with the *pairing* defined in (4.3.11).

Let \mathbf{W} be the ‘working matrix’, which initially equals \mathbf{V} . So it has vectors indexed by $\{\alpha \in \mathbb{N}^d : |\alpha| = k\}$ as the entries in its k th column. To simplify the notation, the following abbreviation

$$\langle \mathbf{W}(\theta, k), \mathbf{W}(\theta, k) \rangle := \langle \mathbf{W}(\theta, k), \mathbf{W}(\theta, k) \rangle_k$$

is used.

The overall process of Gauss elimination with partial row pivoting is achieved by manipulating the \mathbf{W} using the scalar product (C.10). At the j th step, the largest nontrivial entry of \mathbf{W} in column k_j is searched, where k_j is the smallest order satisfying $k_j \geq k_{j-1}$. Then, interchange its row with row j of \mathbf{W} to put it into the pivot position $\mathbf{W}(\theta_j, k_j)$ if necessary. Then, the appropriate multiple of the pivot row $\mathbf{W}(\theta_j, :)$ is subtracted from the subsequent rows in order to make $\mathbf{W}(\theta_j, k_j)$ orthogonal to $\mathbf{W}(\theta_i, k_j)$ for all $i > j$.

As a result of the above ‘elimination’, a factorization

$$L\mathbf{W} = \mathbf{V}$$

is obtained, where L is a unit lower triangular matrix of size $\mathbb{R}^{S \times S}$, and $\mathbf{W} \in \mathbb{R}^{S \times k_S}$ is in row echelon form. It should be noted that for some ordering $\{\theta_1, \theta_2, \dots, \theta_S\}$ of Θ and all j , there is a nondecreasing sequence k_1, k_2, \dots, k_S ¹ such that the vector entry $\mathbf{W}(\theta_j, k_j)$ is the first nonzero entry in the row $\mathbf{W}(\theta_j, :)$. In other words, the matrix $(\mathbf{W}(\theta_i, k_j))_{i,j=1}^S$ is block upper triangular [17]. The orthogonality of $\mathbf{W}(\theta_j, k_j)$ to $\mathbf{W}(\theta_i, k_j)$ when $k_i = k_j$ and $i \neq j$ is guaranteed by the elimination steps, thus the square matrix defined as

$$U := (\langle \mathbf{W}(\theta_i, k_j), \mathbf{W}(\theta_j, k_j) \rangle)_{i,j=1}^S \in \mathbb{R}^{S \times S}$$

is upper triangular and invertible. Due to the orthogonality of $\mathbf{W}(\theta_j, k_j)$ to $\mathbf{W}(\theta_i, k_j)$ when $k_i = k_j$ and $i \neq j$, there may exist some zeros in upper part of U .

After this top-down elimination step is finished, the next task is to enforce orthogonality of the pivot element in row j to the elements *above* it in the pivot column, *i.e.*, to make $\mathbf{W}(\theta_j, k_j)$ orthogonal to $\mathbf{W}(\theta_i, k_j)$ for all $i < j$. This can be accomplished by a further factorization of the matrix \mathbf{W} with $U\mathbf{G} := \mathbf{W}$. As shown later, the matrix $\mathbf{G} \in \mathbb{R}^{S \times k_S}$ is the matrix we want. To factor out the upper triangular matrix U , ‘back substitution’ is used, *i.e.*,

```

for  $j = S, S - 1, \dots, 1$ , do
   $W(\theta_j, :) \leftarrow W(\theta_j, :)/U(j, j)$ 
  for  $i = 1, 2, \dots, j - 1$ , do
     $W(\theta_i, :) \leftarrow W(\theta_i, :) - U(i, j)W(\theta_j, :)$ 
  end for
end for

```

The j th step exerts the orthogonality of the pivot element in row j to the elements *above* it in the pivot column, without changing the orthogonalities already achieved in subsequent columns², and without changing anything in the preceding columns. Consequently, the matrix

$$(\langle \mathbf{G}(\theta_i, k_j), \mathbf{G}(\theta_j, k_j) \rangle)_{i,j=1}^S$$

is diagonal and invertible. As for the diagonal value, we have

$$\begin{aligned} \langle G(\theta_i, :), G_{k_j}(\theta_j, :) \rangle &= \sum_k \langle G(\theta_i, :), G_{k_j}(\theta_j, :) \rangle_k \\ &= \delta_{i,j}/U(j, j), \quad i, j = 1, \dots, S, \end{aligned} \quad (\text{C.11})$$

with G_k given by

$$G_k(i, \alpha) := \begin{cases} G(i, \alpha), & |\alpha| = k \\ 0 & \text{otherwise.} \end{cases} \quad (\text{C.12})$$

¹The sequence k_1, k_2, \dots, k_S need not be strictly increasing.

²Think an example, if $a \perp b, a \perp c$, then $a \perp (\alpha b + \beta c)$, where a, b, c are vectors and α, β are real numbers.

Define a scalar valued function:

$$g_i := \sum_{\alpha} \binom{\cdot}{\alpha} / \alpha! G(\theta_i, \alpha). \quad (\text{C.13})$$

Since $LUG = V = (D^\alpha e_{\theta_i}(0))_{i,\alpha}$, if we multiply a column vector $[\frac{(\cdot)^\alpha}{\alpha!}]$ from right on both sides, where $|\alpha|_{\max} = k_S$, we get

$$\sum_j (LU)(i, j) \left[\sum_{\alpha} \frac{(\cdot)^\alpha}{\alpha!} G(\theta_j, \alpha) \right] = (D^\alpha e_{\theta_i}(0))_{i,\alpha} \cdot \sum_{\alpha} \frac{(\cdot)^\alpha}{\alpha!} = \sum_{\alpha} \frac{(\cdot)^\alpha \cdot \theta_i^\alpha}{\alpha!}, \quad (\text{C.14})$$

and subsequently ³

$$\sum_j (LU)(i, j) g_j = e_{\theta_i}, \quad \text{all } i. \quad (\text{C.15})$$

Further,

$$g_{i\downarrow} := \sum_{|\alpha|=k_i} \binom{\cdot}{\alpha} / \alpha! G(\theta_i, \alpha), \quad (\text{C.16})$$

with equation (C.11), we get

$$\langle g_i, g_{j\downarrow} \rangle = \delta_{i,j} / U(j, j), \quad i, j = 1, \dots, S. \quad (\text{C.17})$$

Due to the above equation, g_1, g_2, \dots, g_S is linearly independent, (C.15) implies that g_1, g_2, \dots, g_S is a basis for \exp_{θ} . What's more, $g_{1\downarrow}, \dots, g_{S\downarrow}$ is linearly independent, thus a basis for Π_{Θ} .

With the above defined functions, the polynomial interpolant in the form

$$\mathcal{I}_{\Theta} f := \sum_{j=1}^S g_{j\downarrow} a(j), \quad (\text{C.18})$$

where $a := \text{diag}(U)(LU)^{-1}(f(\theta_1), \dots, f(\theta_S))$, is the unique interpolant from Π_{Θ} to f on Θ .

Proof. From (C.17), it follows that

$$\langle g_j, \mathcal{I}_{\Theta} f \rangle = a(j) / U(j, j). \quad (\text{C.19})$$

Therefore, from (C.15) and the expression of a ,

$$\begin{aligned} \mathcal{I}_{\Theta} f(\theta_i) &= \langle e_{\theta_i}, \mathcal{I}_{\Theta} f \rangle = \sum_j (LU)(i, j) \langle g_j, \mathcal{I}_{\Theta} f \rangle \\ &= \sum_j (LU)(i, j) \sum_r (LU)^{-1}(j, r) f(\theta_r) = f(\theta_i). \end{aligned} \quad (\text{C.20})$$

□

³There is a little typo in the original paper [17], it is corrected based on the author's derivation.

Appendix D

Properties of the least interpolation method

Descriptions of the properties of the least interpolation method are reproduced from [15]. (Interested readers can refer [16, 17, 18, 13, 15] for proof and further information):

- **Well defined.** Π_Θ is well-defined polynomial space regardless of the choice of Θ .
- **Continuity**, that is, small changes in Θ results in small change Π_Θ .
- **Coalescence \Rightarrow osculation**, *i.e.*, as points coalesce, Lagrange interpolation approaches Hermite interpolation.
- **Translation invariance**, *i.e.*, $\forall(p \in \Pi_\Theta, a \in \mathbb{R}^d) \quad p(a + \cdot) \in \Pi_\Theta$. This implies that Π_Θ is independent of the choice of the origin, that is, it is closed under differentiation.
- **Scale invariance**, *i.e.*, $\forall(p \in \Pi_\Theta, a \in \mathbb{R}) \quad p(a \cdot) \in \Pi_\Theta$.
- **Coordinate system independence**, *i.e.*, an affine change of variables $x \mapsto Ax + c$ (for some invertible matrix A) affects Π_Θ in a reasonable way. Precisely, $\forall(\text{invertible } A \in \mathbb{R}^{d \times d}, c \in \mathbb{R}^d) \quad \Pi_{A\Theta+c} = \Pi_\Theta \circ A^T$.
- **Minimal degree**, *i.e.*, the elements of Π_Θ have as small a degree as is possible. To be precise: For any polynomial space P for which $\langle \Theta, P \rangle$ is correct, and for all j , $\dim P \cap \Pi_j \leq \dim \Pi_\Theta \cap \Pi_j$.
- **Monotonicity**, *i.e.*, $\Theta \subset \Theta' \Rightarrow \Pi_\Theta \subset \Pi_{\Theta'}$.
- **Cartesian product \Rightarrow tensor product**, *i.e.*, $\Pi_{\Theta \times \Theta'} = \Pi_\Theta \otimes \Pi_{\Theta'}$. This means for tensor product grids, we recover the standard tensor product space.
- **Constructible**, *i.e.*, a basis for Π_Θ can be constructed in a finitely many arithmetic steps.

